Universidade de São Paulo
Instituto de Física

# Modelos de energia escura com interação em Cosmologia e testes observacionais com estruturas em grande escala

Rafael José França Marcondes

Orientador: Prof. Dr. Elcio Abdalla

Tese de doutorado apresentada ao Instituto de Física para a obtenção do título de Doutor em Ciências

Banca examinadora:

Prof. Dr. Elcio Abdalla (IF-USP)
Profa. Dra. Ivone Freita Mota de Albuquerque (IF-USP)
Prof. Dr. Laerte Sodré Júnior (IAG-USP)
Prof. Dr. Alberto Vazquez Saa (IMECC-Unicamp)
Prof. Dr. Jailson Souza de Alcaniz (ON)

São Paulo
2016

University of São Paulo
Institute of Physics

# Interacting dark energy models in Cosmology and large-scale structure observational tests

Rafael José França Marcondes

Supervisor: Prof. Dr. Elcio Abdalla

Thesis presented to the Institute of Physics of the University of São Paulo in partial fulfillment of the requirements for the degree of Doctor of Science

Examination board:

Prof. Dr. Elcio Abdalla (IF-USP)
Prof. Dr. Ivone Freita Mota de Albuquerque (IF-USP)
Prof. Dr. Laerte Sodré Júnior (IAG-USP)
Prof. Dr. Alberto Vazquez Saa (IMECC-Unicamp)
Prof. Dr. Jailson Souza de Alcaniz (ON)

São Paulo
2016

## Acknowledgements

I would like to start by thanking my supervisor Elcio Abdalla who warmly welcomed me from a different research area and handed me this challenging project. I thank him for his patience, guidance and for helping make this thesis possible.

I would like to thank my collaborators Morgan Le Delliou, Gastão Lima Neto and Bin Wang for the extensive discussions and advices. Professors Marcos Lima, Luis Raul Abramo and George Matsas were also important for my growth as a physicist and researcher.

I am also very grateful to all my family – Monica, Humberto, Gabriel, Wanessa and Igor – for the unconditional support throughout this long journey and to all my colleagues and friends who contributed with their knowledge and friendship. A very special thank you to Ricardo Landim, André Costa, Lucas Olivari, Riis Bachega, Elisa Ferreira, Maicon Siqueira, Rafael de Castro Lopes, Eduardo Marcondes, José Ebram Filho, Daniela Pena, Fernando Henrique de Sá, Janaína Angeli, Jéssica Fernandes and Andreza Leite.

Finally, I would like to show my most profound gratitude to my girlfriend Nathany for her love, dedication and for being so supportive and sweet.

v

## Abstract

Modern Cosmology offers us a great understanding of the universe with striking precision, made possible by the modern technologies of the newest generations of telescopes. The standard cosmological model, however, is not absent of theoretical problems and open questions. One possibility that has been put forward is the existence of a coupling between dark sectors. The idea of an interaction between the dark components could help physicists understand why we live in an epoch of the universe where dark matter and dark energy are comparable in terms of energy density, which can be regarded as a strange coincidence given that their time evolutions are completely different.

Dark matter and dark energy are generally treated as perfect fluids. Interaction is introduced when we allow for a non-zero term in the right-hand side of their individual energy-momentum tensor conservation equations. We proceed with a phenomenological approach to test models of interaction with observations of redshift-space distortions. In a flat universe composed only of these two fluids, we consider separately two forms of interaction, through terms proportional to the densities of both dark energy and dark matter. An analytic expression for the growth rate approximated as $f = \Omega_{\mathrm{DM}}^{\gamma}$, where $\Omega_{\mathrm{DM}}$ is the percentage contribution from the dark matter to the energy content of the universe and $\gamma$ is the growth index, is derived in terms of the interaction strength and of other parameters of the model in the first case, while for the second model we show that a non-zero interaction cannot be accommodated by the index growth approximation. The successful expressions obtained are then used to compare the predictions with growth of structure observational data in a Markov Chain Monte Carlo code and we find that the current growth data alone cannot impose constraints on the interaction strength due to their large uncertainties.

We also employ observations of galaxy clusters to assess their virial state via the modified Layzer–Irvine equation in order to detect signs of an interaction. We obtain measurements of observed virial ratios, interaction strength, rest virial ratio and departure from equilibrium for a set of clusters. A compounded analysis indicates an interaction strength of $0.29^{+2.25}_{-0.40}$, compatible with no interaction, but a compounded rest virial ratio of $0.82^{+0.13}_{-0.14}$, which means a $2\sigma$ confidence level detection. Despite this tension, the method produces encouraging results while still leaves room for improvement, possibly by removing the assumption of small departure from equilibrium.

**Keywords:**   Cosmology, Dark energy, Dark matter, Large-scale structure

### Resumo

A cosmologia moderna oferece um ótimo entendimento do universo com uma precisão impressionante, possibilitada pelas tecnologias modernas das gerações mais novas de telescópios. O modelo cosmológico padrão, porém, não é livre de problemas do ponto de vista teórico, deixando perguntas ainda sem respostas. Uma possibilidade que tem sido proposta é a existência de um acoplamento entre setores escuros. A ideia de uma interação entre os componentes escuros poderia ajudar os físicos a entender por que vivemos em uma época do universo na qual a matéria escura e a energia escura são comparáveis em termos de densidades de energia, o que pode ser considerado uma estranha coincidência dado que suas evoluções com o tempo são completamente diferentes.

Matéria escura e energia escura são geralmente tratadas como fluidos perfeitos. A interação é introduzida ao permitirmos um tensor não nulo no lado direito das equações de conservação dos tensores de energia-momento. Prosseguimos com uma abordagem fenomenológica para testar modelos de interação com observações de distorções no espaço de *redshift*. Em um universo plano composto apenas por esses dois fluidos, consideramos, separadamente, duas formas de interação, através de termos proporcionais às densidades de energia escura e de matéria escura. Uma expressão analítica para a taxa de crescimento aproximada por $f = \Omega_{\mathrm{DM}}^{\gamma}$, onde $\Omega_{\mathrm{DM}}$ é a contribuição percentual da matéria escura para o conteúdo do universo e $\gamma$ é o índice de crescimento, é deduzida em termos da interação e de outros parâmetros do modelo no primeiro caso, enquanto para o segundo caso mostramos que uma interação não nula não pode ser acomodada pela aproximação do índice de crescimento. As expressões obtidas são então utilizadas para comparar as previsões com dados observacionais de crescimento de estruturas em um programa para Monte Carlo via cadeias de Markov. Concluímos que tais dados atuais por si só não são capazes de restringir a interação devido às suas grandes incertezas.

Utilizamos também observações de aglomerados de galáxias para analisar seus estados viriais através da equação de Layzer–Irvine modificada a fim de detectar sinais de interação. Obtemos medições de taxas viriais observadas, constante de interação, taxa virial de equilíbrio e desvio do equilíbrio para um conjunto de aglomerados. Uma análise combinada indica uma constante de interação $0.29^{+2.25}_{-0.40}$, compatível com zero, mas uma taxa virial de equilíbrio combinada de $0.82^{+0.13}_{-0.14}$, o que significa uma detecção em um intervalo de confiança de $2\sigma$. Apesar desta tensão, o método produz resultados encorajadores enquanto ainda permite melhorias, possivelmente pela remoção da suposição de pequenos desvios do equilíbrio.

**Palavras-chave:**   Cosmologia, Energia escura, Matéria escura, Estrutura do universo

# Acronyms

**ΛCDM** Λ-Cold Dark Matter.
*w***CQDE** fixed-*w* coupled quintessence-like dark energy.
**2dFGRS** Two-degree-Field Galaxy Redshift Survey.
**6dFGS** Six-degree-Field Galaxy Survey.
**ACT** Atacama Cosmology Telescope.
**BAO** baryon acoustic oscillations.
**BBN** Big Bang nucleosynthesis.
**BOSS** Baryon Oscillation Spectroscopic Survey.
**CAMB** Code for Anisotropies in the Microwave Background.
**CDE** coupled dark energy.
**CDF** cumulative distribution function.
**CL** confidence level.
**CMB** cosmic microwave background.
**COBE** COsmic Background Explorer Satellite.
**CPDE** coupled phantom-like dark energy.
**CQDE** coupled quintessence-like dark energy.
**DE** dark energy.
**DfE** departure from equilibrium.
**DM** dark matter.
**eCMB** extended cosmic microwave background.
**EdS** Einstein–de Sitter.
**EFE** Einstein's Field Equations.
**EoS** equation of state.
**FIRAS** Far Infrared Absolute Spectrophotometer.
**FLRW** Friedmann–Lemaître–Robertson–Walker.
**FoG** Fingers-of-God.
**GR** General Relativity.
**LSS** large-scale structure.
**MCMC** Markov Chain Monte Carlo.
**MPSRF** multivariate potential scale reduction factor.
**NFW** Navarro–Frenk–White.

**OVR** observed virial ratio.
**PDF** probability density function.
**PSRF** potential scale reduction factor.
**RMS** root mean square.
**RSD** redshift-space distortion.
**SDSS** Sloan Digital Sky Survey.
**SNe Ia** Type Ia supernovae.
**SPT** South Pole Telescope.
**SRF** scale reduction factor.
**TVR** theoretical virial ratio.
**WMAP** Wilkinson Microwave Anisotropy Probe.

# Contents

# Chapter 1

# Introduction

Cosmology is a branch of astronomy that studies the universe in large scale. The theory of General Relativity (GR) underlies the standard cosmological model, assuming that the physics is the same everywhere and at all times, based on both laboratory results and inferences from what can be observed. However, the validity of this extrapolation is limited. At very high energy scales, GR fails to describe the early universe, which may be dominated by quantum gravity effects.

As far as observations are concerned, the universe looks the same no matter at what direction we look. Also, there is no reason to believe that we live in a privileged part of the universe. Combining these two ideas, we can translate this situation into a scenario well characterized by homogeneity and isotropy at scales larger than a hundred megaparsecs. The assumptions of homogeneity and isotropy are the fundamental principles of cosmology. With this in mind, cosmology attempts to track down the history and evolution of the universe as a whole, from the beginning until the present epoch. Component species, growth of structures and the future of the universe are also between the subjects of interest to cosmologists.

Current observational facts, like the luminosity distances of Type Ia supernovae (SNe Ia) [1, 2], offer us strong evidences of an accelerating expansion going on. This expansion traces back to a hot and dense phase, where all the content of the universe were concentrated in a very small region, then started to expand. This picture is known as the "Big Bang". If the Einstein's Field Equations (EFE) from GR are correct for very large scales, such an accelerated expansion occurring today could only be sustained by a component with negative pressure dominating the universe, as the Friedmann equations point out [3]. We call this component dark energy (DE). A simple cosmological constant can also play that role and is completely equivalent, from a cosmological point of view, to the existence of a DE fluid for which the sum of its pressure and energy density is exactly zero.

At the scales of structures, e.g. galaxies and galaxy clusters, observed galaxy rotation curves differ from the prediction of classical mechanics if the velocity profiles are due to the gravitational field of the matter that we can see (e.g. baryons). When computing the mass considering the luminosity profiles and the mass-to-light ratio, the amount of luminous matter is not sufficient to match the observed profile [4, 5]. One possibility for this discrepancy is the existence of a dark, non-baryonic component which does not interact with the other components except gravitationally. This dark matter (DM) is supposed to permeate the galaxy, extending to the galaxy's halo.

The most currently accepted cosmological model is called $\Lambda$-Cold Dark Matter ($\Lambda$CDM). The standard cosmological model comprises the Big Bang and the subsequent expansion, the universe being composed today, in most part, of dark energy (or the cosmological constant $\Lambda$), cold (non-relativistic) dark matter, baryonic matter and a small amount of radiation. This model describes the universe quite well, in good agreement with the most recent and precise observations (chapter 2), but still leaves some open questions, which we further detail in section 2.2. Perturbation theory is introduced in chapter 3. This is done in a general way that goes beyond the standard model, allowing an interaction between dark energy and dark matter, which may enable us to address some of the questions not answered by the $\Lambda$CDM model. Still in this chapter, the two-point functions are defined. Chapter 4 follows with a brief study of the redshift-space distortions (RSDs). Then, in chapter 5, we work further on the interacting models and develop the equations describing the growth of structures, which we later employ in order to try to constrain the interaction and other model parameters by comparing their predictions with large-scale structure (LSS) data obtained from RSD measurements. The work presented in this chapter has been submitted to the Journal of Cosmology and Astroparticle Physics [6]. Next, in chapter 6 we present a study of an interacting dark energy model based on the equilibrium states of galaxy clusters, trying to evaluate the effect of the interaction by their deviation from the virial theorem. This interesting approach has been published in the Monthly Notices of the Royal Astronomical Society [7]. We conclude in chapter 7 summarizing the results of the two approaches and briefly discuss some of the ideas that we may follow in the next works, aiming to improve those results, particularly for the LSS data in view of upcoming observations that will be provided by the newest and most advanced telescopes currently under construction.

# Chapter 2

# The $\Lambda$CDM model

The universe is expanding. The obvious conclusion is that the distance between two distant galaxies was smaller in the past, possibly all the way back to a hot and dense state. This picture is reinforced by the perception of Hubble [8] that the more distant the celestial objects are, the faster they recede from us. This became famous as the Hubble's law,

$$\dot{r} = H_0 r, \tag{2.1}$$

where $\dot{r}$ is the recessional velocity, $r$ is the proper distance of the object from us and $H_0$ is the Hubble constant, the current value of the time varying expansion rate. This recessional velocity is measured by the redshift $z \equiv (\lambda_{\mathrm{obs}} - \lambda_{\mathrm{emit}})/\lambda_{\mathrm{emit}}$ of the object, i.e., the relative shift of the spectral emission or absorption lines of that source's light. The observed wavelength $\lambda_{\mathrm{obs}}$ differs from the emitted wavelength $\lambda_{\mathrm{emit}}$ due to the motion relative to the observer. For small redshifts, the velocity is measured by $\dot{r} = cz$, where $c$ is the speed of light. Since galaxies are, in general, receding, wavelengths are stretched, going towards the red side of the spectrum, hence the name *red*shift.

A convenient way to study the universe is to separate the expansion from other dynamics. We write the proper distance $r$ of an object in terms of a universal time-only varying scale factor $a(t)$ times a coordinate distance $x$. Since the wavelengths scale as this expansion parameter, $\lambda_{\mathrm{obs}}/\lambda_{\mathrm{emit}} = a_{\mathrm{obs}}/a_{\mathrm{emit}}$, the scale factor relates to the redshift by $1 + z = a(t_{\mathrm{obs}})/a(t_{\mathrm{emit}})$. The proper velocity is then $u \equiv \dot{r} = \dot{a}x + a\dot{x}$, the dot representing differentiation with respect to the cosmic time $t$.

The second term is the peculiar velocity. When a galaxy does not have peculiar velocity and, therefore, has fixed comoving coordinate x, we can write the proper velocity as $\dot{r} = \dot{a}x = (\dot{a}/a)ax = Hr$, which is similar to eq. (2.1) but valid for all cosmic times. Here we introduced the Hubble rate $H(t) \equiv \dot{a}(t)/a(t)$. We use the index 0 to refer to the value of a quantity in the current days ($t_0$). The scale factor

is normalized to 1 today $[a(t_0) \equiv a_0 \equiv 1]$ and $H_0$ in eq. (2.1) means $H(t_0)$.[1] In the absence of peculiar velocity, a galaxy is said to follow the Hubble flow.

We adopt the $(-, +, +, +)$ convention for the metric signature. With the considerations of homogeneity and isotropy, the line element in such a smooth, expanding universe is

$$\mathrm{d}s^2 = -\mathrm{d}t^2 + a^2(t)\,\mathrm{d}\ell^2, \tag{2.2}$$

in units with $c = 1$; $\mathrm{d}\ell$ is the three-dimensional space element. It gives the proper spatial separation between two events occurring at a time $t$. For a flat universe, the spatial element can be written simply as the Euclidean line element $\mathrm{d}\ell^2 = \mathrm{d}x^2 + \mathrm{d}y^2 + \mathrm{d}z^2$, but we also like to express it in hyperspherical coordinates, where it can be generalized to a form that includes a possible spatial curvature. With the usual transformation $x = r \sin\theta \cos\varphi$, $y = r \sin\theta \sin\varphi$ and $z = r \cos\theta$, and then a new change of coordinate $r = \{R \sinh\chi, R\chi, R \sin\chi\}$, according to the curvature $K$ being negative, zero or positive corresponding to open, flat or closed universes, respectively, the line element in the new coordinates is

$$\mathrm{d}s^2 = -\mathrm{d}t^2 + a^2(t)R^2 \left[\mathrm{d}\chi^2 + S_K^2(\chi)\,\mathrm{d}\Omega_\chi^2\right], \tag{2.3}$$

where the function $S_K$ assumes

$$S_K(\chi) = \begin{cases} \sinh\chi, & \text{for } K < 0; \\ \chi, & \text{for } K = 0; \\ \sin\chi, & \text{for } K > 0; \end{cases} \tag{2.4}$$

and $\Omega_\chi$ is the solid angle defined by $\mathrm{d}\Omega_\chi^2 = \mathrm{d}\theta^2 + \sin^2\theta\,\mathrm{d}\varphi^2$. In these coordinates, $\chi$ is an angle coordinate, $R$ is a constant with units of length and can be interpreted as the comoving radius of curvature of the space.

The function $S_K$ can still be written in a unified fashion as

$$S_K(\chi) = \frac{1}{\sqrt{-K}} \sinh\left(\sqrt{-K}\chi\right), \tag{2.5}$$

the flat universe being recovered by taking the limit $K \to 0^-$. The Friedmann–Lemaître–Robertson–Walker (FLRW) metric [3, 12–14] is then obtained by equating $\mathrm{d}s^2 = g_{\mu\nu}\,\mathrm{d}x^\mu\,\mathrm{d}x^\nu$ and eq. (2.3), so in the general coordinates we have the

---

[1]Planck Collaboration [9] constrains the Hubble parameter to $H_0 = 67.74 \pm 0.46\,\mathrm{km\,s^{-1}\,Mpc^{-1}}$ through indirect (model-dependent) measurements, which is in tension with direct (model-independent) measurements by up to $3.4\sigma$; a value of $H_0 = 73.24 \pm 1.74\,\mathrm{km\,s^{-1}\,Mpc^{-1}}$ is measured by Riess et al. [10]. This tension has attracted attention of physicists lately. For more details, see Bernal, Verde & Riess [11] and other references therein.

non-zero metric components

$$g_{tt} = -1, \qquad g_{\chi\chi} = a^2(t)R^2,$$
$$g_{\theta\theta} = a^2(t)R^2 S_K^2(\chi), \qquad g_{\varphi\varphi} = a^2(t)R^2 S_K^2(\chi)\sin^2\theta \tag{2.6}$$

The evolution of $a$ with $t$ in this FLRW universe is determined by the content of the universe. We describe the fluids by the total energy density $\bar{\rho}(t)$ and total pressure $\bar{p}(t)$, so the total energy-momentum tensor is[2]

$$\bar{\mathcal{T}}_{\mu\nu} = \bar{p}\bar{g}_{\mu\nu} + (\bar{p} + \bar{\rho})\,\bar{u}_\mu \bar{u}_\nu, \tag{2.7}$$

where $\bar{u}^\mu = (1, \mathbf{0})$ is the four-velocity of the fluid, comoving with the Hubble flow. The bars indicate that these are background (unperturbed) quantities. Since the distinction will be important when we treat inhomogeneities later, we prefer to introduce this notation already to avoid confusion.

With eq. (2.7) and the metric $\bar{g}_{\mu\nu}$ given by eq. (2.6), we write the time-time component of the EFE as

$$H^2(t) = \frac{8\pi G}{3}\bar{\rho}(t) - \frac{K}{a^2(t)R^2}, \tag{2.8}$$

where $G$ is the Newton's gravitational constant. This is the well-known Friedmann equation [3]. The second term in the right-hand side is the contribution from the curvature. The constant $R$ can be arbitrarily set to 1 and $K$ normalized to $-1$, 0 or 1 simultaneously. This freedom of choice is possible with a redefinition of the radial coordinate $r$ and of the scale factor $a$.

We can think of the curvature as a fluid component with energy density $\bar{\rho}_K(t) \equiv -3K(8\pi G)^{-1}a^{-2}(t)$ and then write the Friedmann equation as

$$H^2(t) = \frac{8\pi G}{3}\left[\bar{\rho}_{\mathrm{DM}}(t) + \bar{\rho}_{\mathrm{b}}(t) + \bar{\rho}_{\mathrm{DE}}(t) + \bar{\rho}_{\mathrm{rad}}(t) + \bar{\rho}_K(t)\right], \tag{2.9}$$

also expressing each component of the total $\bar{\rho}(t)$ explicitly: dark matter, baryonic matter, dark energy and radiation (photons and neutrinos). The $K = 0$ flat universe has an energy density equal to $3H^2(t)/8\pi G \equiv \bar{\rho}_{\mathrm{cr}}(t)$, which is called the critical energy density.[3] Normalizing both sides of eq. (2.9) by $\bar{\rho}_{\mathrm{cr}}(t)$ and defining the dimensionless density parameters $\Omega_A(t) \equiv \bar{\rho}_A(t)/\bar{\rho}_{\mathrm{cr}}(t)$, where $A$ stands for each of the components mentioned above, eq. (2.9) becomes

$$1 = \Omega_{\mathrm{M}}(t) + \Omega_{\mathrm{rad}}(t) + \Omega_{\mathrm{DE}}(t) + \Omega_K(t). \tag{2.10}$$

---

[2]Greek letters are used for indices running through 0, 1, 2 and 3.

[3]The value of the critical energy density today is $\bar{\rho}_{\mathrm{cr},0} = 1.878\,47(23) \times 10^{-29}\,h^2\,\mathrm{g\,cm^{-3}}$ [15], where $h$ is the Hubble constant $H_0$ in units of $100\,\mathrm{km\,s^{-1}\,Mpc^{-1}}$.

The density parameters of matter, radiation and dark energy amount to 1 in a universe without curvature. In general $\Omega_K = 1 - \Omega$, where $\Omega \equiv \Omega_M + \Omega_{rad} + \Omega_{DE}$ is the total density parameter. $\Omega_{DE}$ is also called the vacuum density. Note, by our definitions, that $\Omega_K$ and $K$ have opposite signs, $\Omega_K = -K/a^2H^2 = -K/\dot{a}^2$.

The spatial part of the EFE gives, using eq. (2.8), another important equation referred to as the second Friedmann equation:

$$\frac{\ddot{a}}{a} = -\frac{4\pi G}{3}(\bar{\rho} + 3\bar{p}), \tag{2.11}$$

where $K$ has been canceled out. From eq. (2.11) it follows that a current accelerated expansion restricts the effective equation of state (EoS) parameter—the ratio between the pressure and the energy density $w(t) \equiv \bar{p}(t)/\bar{\rho}(t)$—of the universe as a whole to be less than $-1/3$ so that $\ddot{a} > 0$.

We know from the energy-momentum tensor conservation law in an expanding universe and from their EoS that matter (both dark and baryonic) and radiation evolve with $a^{-3}$ and $a^{-4}$, respectively. Still under the assumption that the conservation applies for each species, the DE density is proportional to $a^{-3(1+w_{DE})}$, where $w_{DE} = \bar{p}_{DE}/\bar{\rho}_{DE}$ is the dark energy EoS parameter. The density simplifies to a constant in the case $w_{DE} = -1$ (cosmological constant),[4] in which we may want to write the density as $\bar{\rho}_\Lambda \equiv \bar{\rho}_{DE}(t) = \bar{\rho}_{DE,0}$. The curvature energy density goes with $a^{-2}$. The energy densities as functions of $a$ rather than $t$ are thus given by

$$\bar{\rho}_M(a) = \bar{\rho}_{M,0}\, a^{-3}, \qquad \bar{\rho}_{DE}(a) = \bar{\rho}_{DE,0}\, a^{-3(1+w_{DE})}, \tag{2.12a}$$

$$\bar{\rho}_{rad}(a) = \bar{\rho}_{rad,0}\, a^{-4}, \qquad \bar{\rho}_K(a) = \bar{\rho}_{K,0}\, a^{-2}. \tag{2.12b}$$

We may want to write eq. (2.9) normalized by $\bar{\rho}_{cr,0}$ instead of $\bar{\rho}_{cr}(t)$, and also express the evolution in terms of the redshift rather than the scale factor. In this case we have

$$\frac{H^2(z)}{H_0^2} = \Omega_{M,0}(1+z)^3 + \Omega_{rad,0}(1+z)^4 + \Omega_{K,0}(1+z)^2 + \Omega_{DE,0}(1+z)^{3(1+w_{DE})}.$$
$$\tag{2.13}$$

Recent observational data from the Wilkinson Microwave Anisotropy Probe (WMAP) [19, 20] indicated, for a six-parameter ΛCDM fit, a DM density parameter $\Omega_{DM,0} = 0.233 \pm 0.023$, a baryonic density parameter $\Omega_{b,0} = 0.0463 \pm 0.0024$,

---

[4]Several models for dark energy which are different in nature have been proposed. They are characterized by the EoS parameter, which can be different from $-1$ and still constant ($w$CDM models) or can vary with time (dynamic dark energy), e.g. quintessence described by a self-interacting scalar field [16–18]. *Planck*'s cosmic microwave background (CMB) data alone do not constrain $w$ too much because of degeneracy with other parameters, but combining them with Wilkinson Microwave Anisotropy Probe (WMAP) polarization data [19], Type Ia supernovae, baryon acoustic oscillations and other data, Planck Collaboration [9] found $w_{DE} = -1.019^{+0.075}_{-0.080}$ at 95 % confidence limit.

the total matter density parameter being $\Omega_{M,0} = 0.279 \pm 0.025$, and a DE component with $\Omega_\Lambda = 0.721 \pm 0.025$. Curvature and radiation density parameters are assumed to be zero in this simple six-parameter model.[5] Placing limits on deviations from this simple model with a seven-parameter model allows non-zero curvature $\Omega_{K,0} = -0.037^{+0.044}_{-0.042}$. The precisions on these parameters are further improved by combining WMAP data with other extended cosmic microwave background (eCMB) measurements from the Atacama Cosmology Telescope (ACT) and the South Pole Telescope (SPT), baryon acoustic oscillations data, and direct measurements of the Hubble constant [19]. Newer results from the *Planck* satellite [9] give the slightly different values $\Omega_{M,0} = 0.3089 \pm 0.0062$, and $\Omega_\Lambda = 0.6911 \pm 0.0062$. All uncertainties correspond to 68 % confidence limits.

## 2.1 Cosmic probes and observational evidences for the ΛCDM model

In this section we discuss some of the most important cosmological probes—Type Ia supernovae (SNe Ia), light element abundances, the cosmic microwave background (CMB), baryon acoustic oscillations (BAO), redshift-space distortions (RSDs) and galaxy clusters—and comment on the Hubble diagram and the uniformity of the CMB, two of the main and most convincing observational facts that settle the Big Bang model on a firm basis.

### 2.1.1 Type Ia supernovae

White dwarf stars that accrete mass from a companion star can eventually reach the Chandrasekhar limit, in which their masses become so big that the electron degeneracy pressure cannot continue counterbalancing the gravitational collapse [22]. The variable star which results from the thermonuclear explosion of a white dwarf is a supernova. The classification of the supernovae is based on their spectral properties. In contrast to those of the Type II, Type I supernovae do not show any Balmer lines of hydrogren in their spectrum. The type Ia differs from its siblings Ib and Ic by the presence of a strong ionized silicon absorption line at wavelength 6150 Å [23].

The acceleration of the expansion of the universe was first discovered by Riess et al. [1] by measuring luminosity distances of SNe Ia, used as standard candles. Perlmutter et al. [2] later confirmed the discovery with analysis of nearby and

---

[5]Radiation density is not actually zero but rather small, at the order of $\Omega_{rad,0} \sim 8 \times 10^{-5}$ [21]. Although negligible today, radiation was important and dominated the universe at early epochs, when $a$ was small, as is evident from eqs. (2.12).

high-redshift supernovae. Once the absolute magnitude of the SNe Ia is determined, one can obtain the observational distance modulus

$$\mu_{\text{obs}} = m - M, \qquad (2.14)$$

where $m$ and $M$ are the apparent and absolute magnitudes, respectively. The theoretical distance modulus of a supernova (labelled by $i$), on the other hand, can be calculated as

$$\mu_{\text{th}}(z_i) \equiv 5 \log_{10} d_L(z_i) + 25. \qquad (2.15)$$

Models can then be constrained through the dependence of the luminosity distance $d_L$ on the cosmological parameters by comparing $\mu_{\text{obs}}$ and $\mu_{\text{th}}$.

**The Hubble diagram**

The Hubble diagram is still the most direct evidence of expansion. Plotting the redshift velocity versus the luminosity distance $d_L$ for distant galaxies reveals the linear increase at low redshifts. At higher redshifts, the luminosity distance is more sensitive to the contents of the universe through the Hubble rate:

$$d_L(z) = \frac{1+z}{H_0 \sqrt{|\Omega_K|}} S_K \left[ H_0 \sqrt{|\Omega_K|} \int_0^z \frac{d\tilde{z}}{H(\tilde{z})} \right]. \qquad (2.16)$$

It is clear, from eqs. (2.13) and (2.16), how the Hubble factor is nearly constant for small $z$, but affects strongly the luminosity distance at high redshifts, besides departing from the constant proportionality between velocity and distance.

The major challenge in the construction of the Hubble diagram is to determine the distances of objects whose intrinsic brightness is unknown. With the use of standard candles one can determine the difference in the distances of these objects from us by their apparent brightness. It is possible to analyze the Hubble diagram at large redshifts with SNe Ia, which are too distant but are bright enough they can still be detected. The redshifts of these objects allow us to distinguish between flat matter dominated, open, and flat universe with a cosmological constant Λ [1, 2], as shown in Figure 2.1. Current high-redshift data favor a universe dominated by some form of dark energy or cosmological constant, with a best-fit of about 70 % of the total energy density for this component.

## 2.1.2   The light element abundances

A distinct confirmation of the Big Bang is the prediction of light element abundances by the Big Bang nucleosynthesis (BBN). Light elements started to form
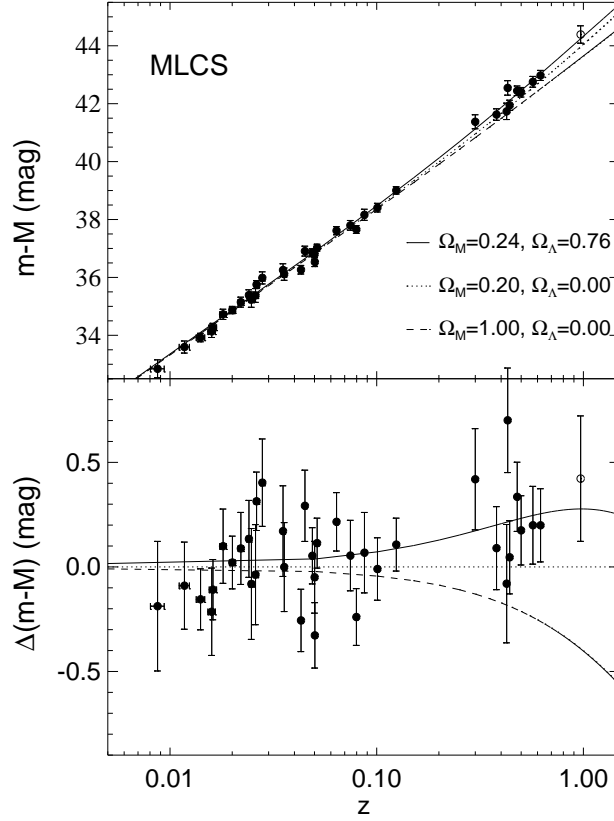
Figure 2.1: Type Ia supernovae diagram from Riess et al. [1]. The upper panel shows apparent magnitudes (as an indicator of distance) versus redshift, for low- and high-redshift SNe Ia samples. The bottom panel shows the residual magnitudes, thus elucidating the preference for a Λ-dominated universe supported by the high-redshift SNe Ia.

when the universe cooled down sufficiently so that protons and neutrons could combine into nuclei, and then nuclei and electrons could combine into atoms. Before that, in a hot universe with temperature $T$ of order $1\,\mathrm{MeV}/k_B$ (where $k_B$ is the Boltzmann constant), the intense radiation prevented atoms from being produced when those particles collided. The atoms would be destroyed by high energy photons right after being formed. When the temperature went down way below the typical nuclei binding energies, the lightest elements started to form. With knowledge of the conditions of the early universe and of the nuclear cross-sections of the relevant processes, one can calculate the expected amount of those elements in the primordial universe. These predictions are in good agreement with current

estimates of light element abundances [21], hence serving as a good argument in favor of the Big Bang theory.[6]

### 2.1.3   The cosmic microwave background

The high degree of uniformity of the CMB is the most compelling evidence of the universe starting with a Big Bang. At the epoch when the universe was hot enough for electrons to be bounded into atoms, the collisions of photons with free electrons had maintained a thermal equilibrium between radiation and matter, making the distribution of the number density of photons follow a black-body spectrum. At some time later, as the universe was expanding, the matter cooled down and became less dense. The radiation then decoupled from the matter to start a free expansion (we call this moment "last scattering"), but the form of its spectrum was kept unchanged. The cosmic temperature when this last interaction of photons with matter took place was about 3000 K, at a redshift 1100. Photons have travelled freely since then. In 1965, Penzias & Wilson [25] discovered such cosmic radiation which later would be reported to have a temperature of about 3 K. The cosmological implications of this CMB were treated by Dicke, Peebles, Roll & Wilkinson [26] in a companion article. More details about the history of the CMB discovery can be found in Weinberg's *Cosmology* [27]. More recently, observations with the Far Infrared Absolute Spectrophotometer (FIRAS) radiometer of the COsmic Background Explorer Satellite (COBE) revealed an almost exact black-body spectrum in the wavelength range of 0.5 cm to 0.05 cm [28]. Figure 2.2 shows these observations compared with the black-body spectrum. The value of the redshifted CMB temperature today has been determined with high precision by Fixsen [30] using WMAP data to recalibrate the FIRAS data. The new, reviewed value is 2.725 48(57) K.

Anisotropies in the CMB (small temperature fluctuations) were discovered by the COBE satellite in 1989. The WMAP measured precisely the temperature power spectrum and probed several cosmological parameters with high accuracy. A best-fitting value of $\Omega_\Lambda \approx 0.72$ for the DE density parameter corresponding to a cosmological constant was found with the 9-year data.

### 2.1.4   Baryon acoustic oscillations

Acoustic waves propagating in the early universe from the end of inflation until decoupling left a characteristic imprint on the anisotropies of the CMB and on the late-time matter power spectrum [31]. These baryon acoustic oscillations provide

---

[6]See also Coc, Uzan & Vangioni [24] for more recent predictions of the light element abundances with the results by the *Planck* satellite mission.
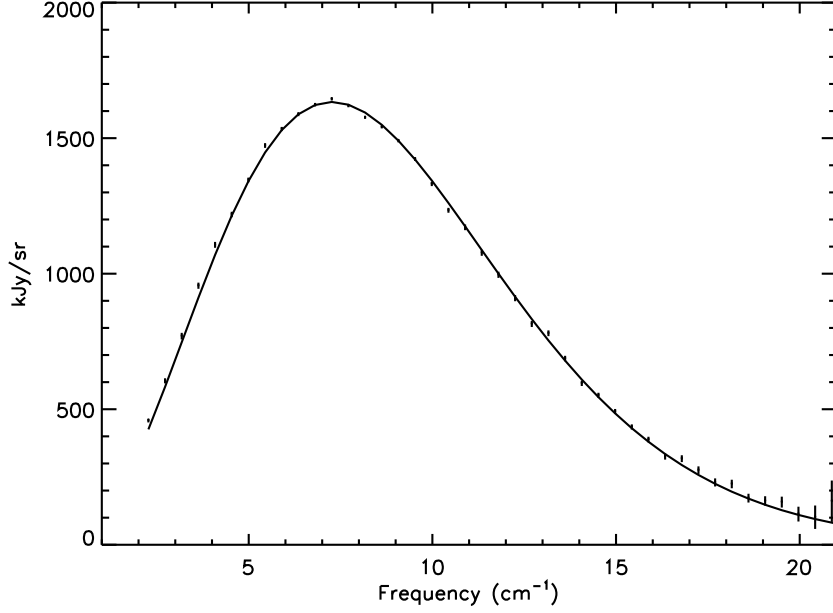
Figure 2.2: Comparison of the intensity of radiation observed with COBE's FIRAS radiometer with a black-body spectrum with temperature 2.728 K, from Fixsen et al. [29]. The intensity is in units of kiloJansky per steradian (1 Jy = $10^{-26}$ W m$^{-2}$ Hz$^{-1}$). The error bars indicate $1\sigma$ experimental uncertainty in intensity.

a standard ruler for the length scale of clustering of baryonic matter, which is about 150 Mpc today [32]. The apparent size of the BAO measured from astronomical observations hints at the expansion history of the universe through measurements of the Hubble rate $H(z)$ and yields measurements of the angular diameter distance $d_A$, which is given by

$$d_A \equiv \frac{\ell}{\theta} = \frac{1}{1+z} \int_0^z \frac{d\tilde{z}}{H(\tilde{z})}, \qquad \text{(flat universe)} \qquad (2.17)$$

the physical size $\ell$ of an object (the BAO characteristic length, for instance) divided by the angle $\theta$ it subtends, and is related to the luminosity distance by $d_A = a^2 d_L$.

## 2.1.5 Redshift-space distortions and the growth factor

As we will see in chapters 4 and 5, RSDs can be used to distinguish between dark energy and modified gravity models or even to help improve the constrains on model parameters. Measuring the growth rate of structures—the rate of change of the growth factor $D$, which is the solution of the dynamic equations governing

11

gravitational instability of matter perturbations:

$$f(z) = \frac{\mathrm{d}\ln D}{\mathrm{d}\ln a}.$$

(2.18)

Measurements of $f(z)$ from observations are dependent on the bias model, i.e., on how galaxies are supposed to trace the matter field. RSDs, however, can provide a measurement of an observable that is independent on the bias model [33].

### 2.1.6 Galaxy clusters

Galaxy clusters are some of the largest structures in the universe, containing from hundreds to thousands of galaxies in a radius from approximately 1 Mpc to 5 Mpc [32]. Clusters are observed through a variety of techniques, e.g. X-ray imaging and spectroscopy and gravitational lensing. N-body simulations can predict the number density $n(z, M)$ of dark matter halos of mass $M$ as a function of the redshift $z$ and of the halo mass $M$. These predictions can be compared to cluster surveys to provide constraints on the expansion history of the universe.

In chapter 6 we adopt a different approach to test an interacting model assessing the virial equilibrium states of clusters through the Layzer–Irvine equation.

## 2.2 Classical problems in Cosmology

The evidences we have seen so far constitute a solid ground for the ΛCDM model with the Big Bang. ΛCDM by itself, however, fails to answer some questions raised based on observational facts. Some of them have been explained by inflation remarkably well. Because of this success, ΛCDM and inflation constitute, together, the current standard model of cosmology.

In this section we present some of these classical problems—the first two of which have already been solved by inflation—and introduce, in section 2.2.4, what motivates most this work, a puzzle whose solution can be the existence of a non-minimal coupling between DE and DM: the coincidence problem.

### 2.2.1 The horizon problem

It is common to rewrite the line element of eq. (2.3) in terms of a new time coordinate, the conformal time $\tau$, defined by $\mathrm{d}\tau = \mathrm{d}t/a(t)$, such that the scale factor can be factored out as a common term to both time and spatial parts:

$$\mathrm{d}s^2 = a^2(\tau)(-\mathrm{d}\tau^2 + \mathrm{d}\ell^2).$$

(2.19)

Note that with this definition, the geodesic of photons $ds^2 = 0$ gives $d\tau = d\ell$. The conformal time $\tau$, which has dimension of length, is the maximum comoving distance light could have traveled since the beginning of the universe.

We discussed in section 2.1.3 how smooth the CMB is. In fact, it is so smooth that it defies the principle of causality. Photons from the CMB share the same temperature to one part in $10^5$. If this uniformity requires that photons were interacting so that larger disturbances in the temperature field could be washed out until an equilibrium was reached, how could it be that even photons that are separated by any distance larger than $\tau$ have the same temperature? They have never been in causal contact, no information could have ever propagated through that distance, no interaction could have happened to put them in equilibrium.

An explanation for this is provided by the theory of inflation, which affirms that the universe passed through a period of incredibly fast expansion right after the Big Bang. The idea gained popularity after Guth [34], who realized that inflation could also address some other cosmological puzzles.[7] The solution suggests that those particles are not in contact today but could have been in contact for some time before. That is, they are now separated by a comoving distance larger than the comoving Hubble radius $1/aH$, but smaller than the conformal time. The requirement is that $aH$ must have increased during inflation, thus implying $\ddot{a} > 0$, namely an accelerated phase of expansion [21, 39].

## 2.2.2 The flatness problem

Back then when the scale factor was of order $3 \times 10^{-4}$, at redshift about 3000, the universe underwent a transition phase. From a previously radiation dominated era, it became dominated by both radiation and matter, and then matter surpassed radiation in energy density. The scale factor, which had been increasing with $t^{1/2}$, then started to evolve with $t^{2/3}$ during the matter-dominated era until near the present.[8] This can be seen by integrating eq. (2.13) (in terms of $a$) considering only the dominant component in the right-hand side.

Let us now turn our attention to the evolution of the curvature term $\Omega_K(t) = -K/\dot{a}^2$ of eq. (2.10). Since $\dot{a} \propto t^{-1/3}$, $\Omega_K$ increased at the same rate as $a$, i.e., with $t^{2/3}$. Thus if $|\Omega_K| < 1$ today,[9] as observations indicate, in the time the scale factor increased by a factor of order $10^4$, then $\Omega_K$ must have increased by the

---

[7]Guth's first version of inflation had a serious problem, explained in Hawking, Moss & Stewart [35] and Guth & Weinberg [36], and was replaced by a new model by Linde [37] and Albrecht & Steinhardt [38], known as slow-roll inflation.

[8]At redshift $z \sim 0.4$ ($a \sim 0.7$) the universe became dominated by dark energy or cosmological constant and the scale factor dependence with time became exponential.

[9]Since this DE-dominated phase began only recently, considering only the long matter-dominated era is sufficient to evince the flatness problem. One can conclude that taking into ac-

same factor, which means $|\Omega_K| < 10^{-4}$ at that time of matter-radiation equality. The temperature of the primordial plasma of quarks and photons, which were in a thermal equilibrium, followed the same evolution of the temperature of a gas of photons, that is, scaling with $a^{-1}$ as a consequence of the redshift, since the temperature is proportional to the photon energy or frequency. At that time, this temperature was of order $10^4$ K. Before this, in the radiation-dominated era, $a$ was increasing as $t^{1/2}$ and then $\Omega_K$ was proportional to $t$. Since $T \propto a^{-1} \propto t^{-1/2}$ during that period, we can equivalently state that $\Omega_K$ was increasing as $T^{-2}$. The observed helium abundance coincides with this temperature being of order $10^{10}$ K at the beginning of this period [27]. If the temperature has decreased by a factor $10^6$, the curvature must have increased by $10^{12}$ in the same period. In order for $|\Omega_K|$ to be smaller than $10^{-4}$ at $T \sim 10^4$ K, it could not have been greater than $10^{-16}$ at $T \sim 10^{10}$ K. At earlier times, $|\Omega_K|$ must have been even smaller.

This fine tuning of the curvature density parameter potentially poses a problem. It would be good if we could explain why the universe was so flat at the beginning, although one can argue that there is no impediment even for $\Omega_K$ being exactly zero. However, it is more natural to expect that some mechanism could have been responsible for flattening the universe independently of its initial curvature, hence avoiding the need of specific assumptions. This problem is also solved by inflation. A sufficient preceding period of inflation is enough to guarantee that the curvature is negligible at the beginning of the radiation-dominated era. The condition required is the same that solves the horizon problem. If the universe has expanded during inflation more or less exponentially by a factor $e^{\mathcal{N}}$, where $\mathcal{N}$ is the number of $e$-foldings, the condition is

$$e^{\mathcal{N}} > \frac{a_\mathrm{I} H_\mathrm{I}}{a_0 H_0}, \tag{2.20}$$

where the subscript I refers to the cosmic time when inflation ends and the radiation dominance begins.

## 2.2.3 The cosmological constant problem

The cosmological constant $\Lambda$ was first proposed by Einstein [40] as a free parameter to accommodate a static universe solution for his field equations as

$$\bar{\mathcal{R}}_{\mu\nu} - \frac{1}{2}\bar{g}_{\mu\nu}\bar{\mathcal{R}} - \Lambda\bar{g}_{\mu\nu} = -8\pi G\bar{\mathcal{T}}_{\mu\nu}, \tag{2.21}$$

where $\bar{\mathcal{R}}_{\mu\nu} = \bar{\mathcal{R}}^{\rho}{}_{\mu\rho\nu}$ is the Ricci tensor, given by the contraction of Riemann tensor in the first and third indices, $\bar{\mathcal{R}} = \bar{\mathcal{R}}^{\nu}{}_{\nu}$ is the Ricci scalar (the contracted Ricci

---

count this latest regime of the scale factor worsens the problem, requiring an even finer tuning of the initial curvature.

tensor) and $\bar{\mathcal{T}}_{\mu\nu}$ is the energy-momentum tensor, which describes the content of the universe.

With a non-zero cosmological constant, the Friedmann equation (2.8) is written as

$$H^2(t) = -\frac{K}{a^2(t)} + \frac{8\pi G}{3}\bar{\rho}(t) + \frac{\Lambda}{3}, \qquad (2.22)$$

where now the total density $\bar{\rho}(t)$ accounts for the matter (and radiation) content only, not including a dark energy field (i.e., the term $\Lambda$ is equivalent to $8\pi G\bar{\rho}_{\text{DE}}$).

Cosmological observations constrain the effective vacuum energy density to be no greater than $10^{-47}\,\text{GeV}^4$. On the other hand, by summing the zero-point energies of all modes (up to a cutoff) of some field describing the empty space gives $\bar{\rho}_{\text{vac}} = 2 \times 10^{71}\,\text{GeV}^4$, a discrepancy of 118 orders of magnitude [41].[10] It is true that what really should be smaller than $10^{-47}\,\text{GeV}^4$ is the effective vacuum energy density, which is composed of the vacuum energy density $\bar{\rho}_{\text{vac}}$, from the energy-momentum tensor in vacuum $\bar{\mathcal{T}}_{\mu\nu}^{(\text{vac})} = -\bar{\rho}_{\text{vac}}\bar{g}_{\mu\nu}$, and the cosmological constant contribution $\Lambda/8\pi G$, but then we should have the two terms canceling to 118 decimal places:

$$\left|\bar{\rho}_{\text{vac}} + \frac{\Lambda}{8\pi G}\right| < 10^{-47}\,\text{GeV}^4. \qquad (2.23)$$

One could argue that the effective energy density $|\bar{\rho}_{\text{vac}} + \Lambda/8\pi G|$ is exactly zero (or equivalently the effective cosmological constant $\Lambda_{\text{eff}} = \Lambda + 8\pi G\bar{\rho}_{\text{vac}}$ is exactly zero), with an explanation yet to be given presumably by a theory of quantum gravity, but current cosmological observations point to a non-zero, although extremely small and fine-tuned, value for $\Lambda_{\text{eff}}$ [44].

## 2.2.4 The cosmic coincidence problem

We already know that dark matter and dark energy evolved completely differently with the expansion of the universe. While the energy density of dark matter has decreased as $a^{-3}$, the dark energy's remained constant. Surprisingly, both components contribute to the energy content of the universe by similar (of the same order) amounts today [45, 46]. One could expect totally different orders of magnitude, specially when noting that in the standard model the DM-DE density ratio $\rho_{\text{DM}}/\rho_{\text{DE}}$ should just cross the value 1 at some time, without being forced towards it. Thus the fact that those two components have similar densities just now can be seen as a coincidence.

---

[10]This discrepancy can vary depending on the chosen cutoff scale. For instance, taking the cutoff at the Planck scale gives $\bar{\rho}_{\text{vac}} \simeq 10^{74}\,\text{GeV}^4$ [42, 43], thus yielding a divergence of 121 orders of magnitude.

Some physicists have proposed the existence of a mechanism that drives the ratio $\rho_{DM}/\rho_{DE}$ close to 1 [47–49]. In general, allowing an interaction in the dark sector, i.e., between DM and DE, through a non-zero term in the right-hand side of the energy-momentum tensor conservation equation for these components can help alleviate the coincidence problem. In this case, despite the flux between the dark components, the total energy density is still conserved. The effect of such an interaction is that when the right conditions are satisfied we have $\rho_{DM}/\rho_{DE} \sim 1$ for a longer period of time. Therefore, it becomes more reasonable to find a ratio of this order from observations [50].

Chapters 5 and 6 present our works on interacting dark sector models of cosmology which aim to provide a solution to this problem or at least alleviate it.

# Chapter 3

# Fluid inhomogeneities and space-time perturbations

Cosmology as we have seen so far is well described by the FLRW metric, as long as the scales are large enough so that homogeneity still applies. In smaller scales, the assumption is obviously invalid, since matter tends to clump in structures like clusters of galaxies, galaxies and planetary systems. We believe that large-scale structures result from density fluctuations of a pressureless cold dark matter fluid amplified by the gravitational attraction. In this chapter we introduce perturbations to the metric and the fluids in a general interacting-dark sectors cosmology, which obviously also applies to the non-interacting standard model when the coupling is zero. Later, we define the two-point functions that describe the density fields statistically.

## 3.1 The perturbed metric and field equations

According to GR, the matter or energy contents of the universe define the space-time geometry, which in turn determines the geodesic lines that particles and bodies will follow. This is encoded in the EFE

$$\mathcal{R}_{\mu\nu} - \frac{1}{2} g_{\mu\nu} \mathcal{R} = -8\pi G \mathcal{T}_{\mu\nu}, \tag{3.1}$$

where $\mathcal{T}_{\mu\nu}$ is the total energy-momentum tensor,

$$\mathcal{R}_{\mu\nu} = \partial_\nu \Gamma^\lambda_{\ \mu\lambda} - \partial_\lambda \Gamma^\lambda_{\ \mu\nu} + \Gamma^\rho_{\ \mu\lambda} \Gamma^\lambda_{\ \nu\rho} - \Gamma^\rho_{\ \mu\nu} \Gamma^\lambda_{\ \lambda\rho} \tag{3.2}$$

is the Ricci tensor and $\mathcal{R}$ is the Ricci scalar, given by the space-time metric $g_{\mu\nu}$ and the Christoffel symbols

$$\Gamma^\mu_{\ \nu\lambda} = \frac{1}{2} g^{\mu\rho} \left( \partial_\nu g_{\lambda\rho} + \partial_\lambda g_{\rho\nu} - \partial_\rho g_{\nu\lambda} \right). \tag{3.3}$$

17

If we want to study perturbations to the functions that describe the fluids, we have to consider also the perturbations to the metric.

Perturbations are in general denoted by a $\delta$ preceding the quantity's symbol, while a bar denotes the unperturbed part. One exception is the metric, whose perturbation is usually denoted by $h_{\mu\nu}$, so the total metric tensor is

$$g_{\mu\nu} = \bar{g}_{\mu\nu} + h_{\mu\nu}. \tag{3.4}$$

The perturbation to the inverse of a general matrix $M$ is $\delta M^{-1} = -M^{-1}(\delta M) M^{-1}$, so $h^{\mu\nu} = -\bar{g}^{\mu\rho}\bar{g}^{\nu\sigma}h_{\rho\sigma}$. The perturbed Christoffel symbols are

$$\delta\Gamma^{\mu}{}_{\nu\lambda} = \frac{1}{2}\bar{g}^{\mu\rho}\left(-2h_{\rho\sigma}\bar{\Gamma}^{\sigma}{}_{\nu\lambda} + \partial_{\lambda}h_{\rho\nu} + \partial_{\nu}h_{\lambda\rho} - \partial_{\rho}h_{\nu\lambda}\right), \tag{3.5}$$

which lead to the perturbed Ricci tensor

$$\delta\mathcal{R}_{\mu\nu} = \partial_{\nu}\delta\Gamma^{\lambda}{}_{\mu\lambda} - \partial_{\lambda}\delta\Gamma^{\lambda}{}_{\mu\nu} + \delta\Gamma^{\rho}{}_{\mu\lambda}\bar{\Gamma}^{\lambda}{}_{\nu\rho} + \delta\Gamma^{\lambda}{}_{\nu\rho}\bar{\Gamma}^{\rho}{}_{\mu\lambda} - \delta\Gamma^{\rho}{}_{\mu\nu}\bar{\Gamma}^{\lambda}{}_{\lambda\rho} - \delta\Gamma^{\lambda}{}_{\lambda\rho}\bar{\Gamma}^{\rho}{}_{\mu\nu} \tag{3.6}$$

and the perturbed EFE

$$\delta\mathcal{R}_{\mu\nu} - \frac{1}{2}\left(h_{\mu\nu}\bar{g}^{\lambda\rho} + \bar{g}_{\mu\nu}h^{\lambda\rho}\right)\bar{\mathcal{R}}_{\lambda\rho} - \frac{1}{2}\bar{g}_{\mu\nu}\bar{g}^{\lambda\rho}\delta\mathcal{R}_{\lambda\rho} = -8\pi G\delta\mathcal{T}_{\mu\nu}, \tag{3.7}$$

up to first order in perturbations.

### 3.1.1 The perturbed FLRW metric

We write the perturbed FLRW in the Newtonian gauge [27] and restrict ourselves to scalar perturbations only. It will be convenient to use the conformal time, which we already introduced in section 2.2.1. The line element is

$$ds^2 = a^2(\tau)\left[-(1+2\psi)\,d\tau^2 + (1-2\phi)\,\delta_{ij}\,dx^i dx^j\right], \tag{3.8}$$

with $\phi = \phi(x^{\mu})$ and $\psi = \psi(x^{\mu})$ being small perturbations, satisfying $|\phi|, |\psi| \ll 1$. Assuming there is no anisotropic stress, we have $\psi = \phi$. The non-zero components of the unperturbed and perturbed metric parts are

$$\begin{aligned}
\bar{g}_{00} &= -a^2, & h_{00} &= -2a^2\phi, \\
\bar{g}_{ij} &= a^2\delta_{ij}, & h_{ij} &= -2a^2\phi\delta_{ij}.
\end{aligned} \tag{3.9}$$

## 3.2  Fluid perturbations and evolution equations

The unperturbed energy-momentum tensor assumes the perfect fluid form due to its rotational and translational invariance,

$$\bar{\mathcal{T}}_{\mu\nu} = \bar{p}\bar{g}_{\mu\nu} + (\bar{p} + \bar{\rho})\,\bar{u}_\mu\bar{u}_\nu, \tag{3.10}$$

where $\bar{p}$ is pressure, $\bar{\rho}$ is the energy density and $\bar{u}^\mu = (a^{-1}, 0, 0, 0)$ is the four-velocity of the comoving fluid. It follows from the EFE that the total energy-momentum tensor must be conserved, $\nabla_\mu\bar{\mathcal{T}}^\mu{}_\nu = 0$. Noting that the non-zero components of the energy-momentum tensor are $\bar{\mathcal{T}}^0{}_0 = -\bar{\rho}$ and $\bar{\mathcal{T}}^i{}_j = \bar{p}\delta^i_j$, the $\nu = 0$ conservation equation reads

$$\bar{\rho}' + 3\mathcal{H}(1 + w)\bar{\rho} = 0, \tag{3.11}$$

where we have substituted $\bar{p} = w\bar{\rho}$ and $\mathcal{H} \equiv a'/a$ is the Hubble rate in terms of the conformal time, the prime denoting derivatives with respect to $\tau$.

Treating the components as perfect fluids, we can also write eq. (3.10) for each matter component $A$ separately, but the conservation of the energy-momentum tensor need not to apply individually. In fact, an interaction between dark matter and dark energy is included by allowing a non-zero tensor $\bar{Q}^A{}_\nu$ in the right-hand side of the conservation equations, $\nabla_\mu\bar{\mathcal{T}}_A{}^\mu{}_\nu = \bar{Q}^A{}_\nu$, as long as the total energy-momentum conservation still applies, i.e., $\sum_A \bar{Q}^A{}_\nu = 0$. In this case, eq. (3.11) for the fluid $A$ reads

$$\bar{\rho}'_A + 3\mathcal{H}(1 + w_A)\bar{\rho}_A = a^2\bar{Q}^{A\,0} = -\bar{Q}^A_0 \tag{3.12}$$

The perturbed energy-momentum tensor of the fluid $A$ has the components

$$
\begin{aligned}
\delta\mathcal{T}_A{}^0{}_0 &= -\delta\rho_A, & \delta\mathcal{T}_A{}^i{}_j &= \delta p_A\,\delta^i_j, \\
\delta\mathcal{T}_A{}^i{}_0 &= -a^{-1}(\bar{\rho}_A + \bar{p}_A)\,\delta u_A{}^i, & \delta\mathcal{T}_A{}^0{}_i &= a^{-1}(\bar{\rho}_A + \bar{p}_A)\,\delta u_{A\,i}, \\
\delta\mathcal{T}_{A\,00} &= a^2(\delta\rho_A + 2\bar{\rho}_A\phi), & \delta\mathcal{T}_{A\,ij} &= a^2(\delta p_A - 2\bar{p}_A\phi)\,\delta_{ij},
\end{aligned}
\tag{3.13}
$$

and the perturbed energy-momentum conservation equations lead to the evolution equations for the density contrast and velocity perturbations

$$-\delta'_A - \left[3\mathcal{H}\left(c_{sA}^2 - w_A\right) - \frac{\bar{Q}^A_0}{\bar{\rho}_A}\right]\delta_A - (1 + w_A)(\theta_A - 3\phi') = \frac{\delta Q^A_0}{\bar{\rho}_A}, \tag{3.14a}$$

$$\theta'_A + \left[\mathcal{H}(1 - 3w_A) - \frac{\bar{Q}^A_0}{\bar{\rho}_A} + \frac{w'_A}{1 + w_A}\right]\theta_A - k^2\phi - \frac{c_{sA}^2}{1 + w_A}k^2\delta_A = \frac{ik^i\delta Q^A_i}{\bar{\rho}_A(1 + w_A)}, \tag{3.14b}$$

from $\nu = 0$ and $\nu = i$, respectively, using $\delta u_{A\,0} = -a\phi$, from the condition $g_{\mu\nu}u_A{}^\mu u_A{}^\nu = -1$. The density contrast (or overdensity) is defined as the relative density perturbation $\delta_A \equiv \delta\rho_A/\bar{\rho}_A$, $\theta_A \equiv a^{-1}ik^j\delta u_{A\,j}$ is the divergence of the velocity perturbation in Fourier space, where $k^i$ are the components of the wavevector and $k^2 = \mathbf{k}\cdot\mathbf{k}$; $\delta Q_\mu^A$ are the perturbations to the exchange of energy-momentum in the perturbed conservation equations and $c_{sA}^2 \equiv \delta p_A/\delta\rho_A$ is the sound speed of the fluid $A$. Another useful equation is obtained from the perturbed time-time field equation,

$$k^2\phi + 3\mathcal{H}^2\phi = -3\mathcal{H}\phi' - 4\pi G a^2 \bar{\rho}\delta. \qquad (3.15)$$

This is the relativistic Poisson equation in Fourier space. It relates the potential $\phi$ in the metric to the total density perturbation $\delta\rho = \bar{\rho}\delta = \sum_A \bar{\rho}_A\delta_A$.

### 3.2.1 Growth function and growth rate

Structures form in the universe in the Newtonian regime of GR, on spatial scales much smaller than the horizon, i.e., $k \gg \mathcal{H}$, and with negligible time variation of the gravitational potential. This allows us to discard the second term in the left-hand side of eq. (3.15) and also the term proportional to $\phi'$. Additionally, the sound speed of dark energy can be supposed large enough so that DE perturbations are smoothed out on sub-horizon scales [51]. The Poisson equation thus reduces to

$$k^2\phi = -4\pi G a^2 \bar{\rho}\delta. \qquad (3.16)$$

Considering the universe composed of matter and dark energy only, without interaction, we can also use eq. (2.9) and write

$$k^2\phi = -\frac{3}{2}\mathcal{H}^2\Omega_M\delta_M. \qquad (3.17)$$

We now take the time derivative of eq. (3.14a) to replace $\theta'_M$ in eq. (3.14b) and, with eq. (3.17), get the evolution equation for the matter perturbations

$$\delta''_M + \mathcal{H}\delta'_M - \frac{3}{2}\mathcal{H}^2\Omega_M\delta_M = 0. \qquad (3.18)$$

In order to solve eq. (3.18), one needs to know the evolution of $a$ or $\mathcal{H}$ with time. It is interesting to note, nonetheless, that this equation for $\delta_M$ does not involve derivatives with respect to spatial coordinates nor dependence on $\mathbf{x}$. This allows us to decompose the solution separating the spatial and time dependences. Therefore, the general solution of eq. (3.18) will have the form

$$\delta_M(\tau, \mathbf{x}) = \varepsilon_M^+(\mathbf{x})D_M^+(\tau) + \varepsilon_M^-(\mathbf{x})D_M^-(\tau), \qquad (3.19)$$

a linear combination of the two particular solutions, the growing mode $D_M^+$ and the decaying mode $D_M^-$. At late times, the decaying mode becomes irrelevant as the increasing solution dominates. The functions $\varepsilon_M^+$ and $\varepsilon_M^-$ correspond to the density contrast field at some time that can be arbitrarily chosen according to the normalization of $D_M^+$ and $D_M^-$. For example, we can take $\varepsilon_M^+(\mathbf{x})$ to be the current density perturbation divided by the growth function today $\delta_{M,0}(\mathbf{x})/D_{M,0}^+$, so that (neglecting the decaying mode)

$$\delta_M(z, \mathbf{x}) = \frac{\delta_{M,0}(\mathbf{x})}{D_{M,0}^+} D_M^+(z) \equiv \delta_{M,0}(\mathbf{x})\mathcal{D}_M(z; 0), \tag{3.20}$$

with the last equality defining the backward propagation function $\mathcal{D}_M(z; 0) \equiv \frac{D_M^+(z)}{D_{M,0}^+}$ for the evolution of the matter perturbation from redshift zero to $z$, with the implicit assumption that the evolution remains linear until the present epoch.

It is also convenient to define the linear matter growth rate

$$f(z) \equiv \frac{d \ln \delta_M}{d \ln a} \quad \text{or} \quad f(z) \equiv \frac{d \ln D_M^+(z)}{d \ln a} \tag{3.21}$$

and analyze eq. (3.18) in terms of $f(z)$ to simplify the study of redshift-space distortions and growth of structures, as we are going to do in chapters 4 and 5. In terms of the growth rate, the linearized continuity equation $\delta_M' + \theta_M = 0$ [eq. (3.14a)] is then

$$\mathcal{H}af\delta_M + \theta_M = 0. \tag{3.22}$$

**Solutions of the growth function**

The solution of eq. (3.18) can be found following an argument based on the Birkhoff's theorem, which says that different parts of the universe can be imagined to evolve as independent homogeneous universes [52]. We change back to the cosmic time in order to use this method. The local expansion parameter for an observer at $\mathbf{x}$ differs from the mean background parameter $\bar{a}$ by a small quantity $\epsilon$ as

$$a(t, \mathbf{x}) = \bar{a}(t) \left[ 1 - \epsilon(t, \mathbf{x}) \right]. \tag{3.23}$$

That is, $a$ is the scale factor of a homogeneous universe with parameters slightly different from those of the homogeneous universe characterized by the scale factor $\bar{a}$. Eq. (2.12a) implies that

$$\rho_M a^3 = \bar{\rho}_M \left( 1 + \delta_M \right) \bar{a}^3 \left( 1 - \epsilon \right)^3 = \bar{\rho}_M \bar{a}^3 \tag{3.24}$$

and then

$$\delta_{\mathrm{M}} = 3\epsilon, \tag{3.25}$$

up to first order in $\delta_{\mathrm{M}}$ and $\epsilon$. The perturbation to the matter density fluid is the fractional difference of the densities of the two slightly different universes and is three times the fractional difference of the expansion parameters.

Let us suppose we have a family of functions $a(t, \alpha)$, labelled by the parameter $\alpha$, that are solutions to the scale factor in the Friedmann equations of different homogeneous universes. Then

$$\epsilon = -\frac{\delta a}{a} = -\frac{\delta\alpha}{a}\frac{\partial a}{\partial\alpha} \qquad \text{and} \qquad \delta = -3\frac{\delta\alpha}{a}\frac{\partial a}{\partial\alpha}. \tag{3.26}$$

The second Friedmann equation

$$\ddot{a} = -\frac{4\pi G}{3}\bar{\rho}_{\mathrm{M}}a + \frac{\Lambda}{3}a \tag{3.27}$$

integrated in $a$ gives

$$\dot{a}^2 = X(a), \qquad \text{with} \qquad X(a) \equiv \frac{8\pi G}{3}(\bar{\rho}_{\mathrm{M}}a^3)\frac{1}{a} + \frac{\Lambda}{3}a^2 + \mathcal{K}. \tag{3.28}$$

This is the first Friedmann equation. Comparison with eq. (2.8) reveals the constant of integration $\mathcal{K}$ is related to the spatial curvature through $\mathcal{K} = -K/R^2$. Integrating (3.28) in time gives

$$t = \int \frac{\mathrm{d}a}{X^{1/2}} + t_c, \tag{3.29}$$

where $t_c$ is a second constant of integration. $t_c$ and $\mathcal{K}$ can be thought as parameters distinguishing the neighbouring universes. Differentiating eq. (3.29) with respect to $\mathcal{K}$ and $t_c$, keeping $t$ fixed, we get

$$\frac{\mathrm{d}t}{\mathrm{d}\mathcal{K}} = \frac{\partial a}{\partial\mathcal{K}}\frac{\partial}{\partial a}\int\frac{\mathrm{d}a}{X^{1/2}} + \frac{\partial X}{\partial\mathcal{K}}\frac{\partial}{\partial X}\int\frac{\mathrm{d}a}{X^{1/2}} + \frac{\mathrm{d}t_c}{\mathrm{d}\mathcal{K}}$$

$$0 = X^{-1/2}\frac{\partial a}{\partial\mathcal{K}} - \frac{1}{2}\frac{\partial X}{\partial\mathcal{K}}\int\frac{\mathrm{d}a}{X^{3/2}} + 0 \Rightarrow$$

$$\Rightarrow \frac{\partial a}{\partial\mathcal{K}} = \frac{X^{1/2}}{2}\int\frac{\mathrm{d}a}{X^{3/2}}; \tag{3.30}$$

and

$$\frac{\mathrm{d}t}{\mathrm{d}t_c} = \frac{\partial a}{\partial t_c}\frac{\partial}{\partial a}\int\frac{\mathrm{d}a}{X^{1/2}} + \frac{\partial X}{\partial t_c}\frac{\partial}{\partial X}\int\frac{\mathrm{d}a}{X^{1/2}} + \frac{\mathrm{d}t_c}{\mathrm{d}t_c}$$

$$0 = X^{-1/2}\frac{\partial a}{\partial t_c} + 0 + 1 \Rightarrow \frac{\partial a}{\partial t_c} = -X^{1/2}, \tag{3.31}$$

thus giving, from eq. (3.26) with $\alpha = \mathcal{K}$,

$$\delta^+(t, \mathbf{x}) = -\frac{3}{2}\delta\mathcal{K}\frac{X^{1/2}}{a}\int\frac{\mathrm{d}a}{X^{3/2}} \tag{3.32}$$

and, with $\alpha = t_c$,

$$\delta^-(t, \mathbf{x}) = 3\delta t_c\frac{X^{1/2}}{a}. \tag{3.33}$$

$\delta^+$ and $\delta^-$ are the growing and decaying mode of the matter density field, corresponding to the terms $\varepsilon^+_{\mathrm{M}}(\mathbf{x})D^+_{\mathrm{M}}(t)$ and $\varepsilon^-_{\mathrm{M}}(\mathbf{x})D^-_{\mathrm{M}}(t)$ in eq. (3.19), respectively. One can verify that they satisfy $\ddot{\delta}_{\mathrm{M}} + 2H\dot{\delta}_{\mathrm{M}} - \frac{3}{2}H^2\Omega_{\mathrm{M}}\delta_{\mathrm{M}} = 0$, which is equivalent to (3.18) but expressed in terms of the cosmic time, and are indeed the solutions to the matter density contrast equation.

One interesting case is the simple Einstein–de Sitter (EdS) cosmology—a matter-only universe with the flat FLRW metric. In this cosmology, $X = \frac{8\pi G}{3}\frac{\bar{\rho}_{\mathrm{M}}a^3}{a} \propto a^{-1}$ giving $D^+_{\mathrm{M}} \propto a \propto t^{2/3}$ from eq. (3.32) and $D^-_{\mathrm{M}} \propto a^{-3/2} \propto t^{-1}$ from eq. (3.33), the time dependence coming from eq. (3.28). The growth rate $f(a) = \frac{\mathrm{d}\ln D^+_{\mathrm{M}}}{\mathrm{d}\ln a}$ in the EdS universe is constant and equal to 1.

## 3.3 The matter correlation function and power spectrum

We now define a quantity of extreme importance for confronting theory and observations. In practice, in order to compare theory with observations, one cannot compare a map of galaxies generated by simulations to the actual observed distribution of galaxies. Instead, these tests are done by comparing their statistical properties. The key quantity is the two-point correlation function $\xi(\mathbf{r})$, or autocorrelation function of the density field,[1]

$$\xi_{\mathrm{M}}(\mathbf{r}) \equiv \langle\delta_{\mathrm{M}}(\mathbf{r}')\delta_{\mathrm{M}}(\mathbf{r}' + \mathbf{r})\rangle = \frac{1}{V}\int_V \delta_{\mathrm{M}}(\mathbf{r}')\delta_{\mathrm{M}}(\mathbf{r}' + \mathbf{r})\,\mathrm{d}\mathbf{r}', \tag{3.34}$$

which is an average of the product of the density contrast at two points separated by $\mathbf{r}$ over some volume $V$ (see Peebles [53] and references therein). Isotropy of the universe actually implies that $\xi_{\mathrm{M}}$ depends only on the modulus $r$ of the vector $\mathbf{r}$. We may then write $\xi_{\mathrm{M}}(r)$ instead. Of course the correlation function also depends on $\tau$, as the inhomogeneities evolve with time. However, we omit this dependence in this section for simplicity of notation.

---

[1]In this section $\mathbf{r}'$ is a point of space just as $\mathbf{r}$, not to be confused with $\mathrm{d}\mathbf{r}/\mathrm{d}\tau$.

In Fourier space, the density contrast is the Fourier transform of $\delta_A(\mathbf{r})$ (now denoting both the matter field $\delta_M$ and the galaxy field $\delta_g$),

$$\hat{\delta}_A(\mathbf{k}) \equiv \int d\mathbf{r}\, e^{-i\mathbf{k}\cdot\mathbf{r}}\delta_A(\mathbf{r}). \tag{3.35}$$

We leave the normalization factor in the inverse Fourier transform,

$$\delta_A(\mathbf{r}) = (2\pi)^{-3} \int d\mathbf{k}\, e^{i\mathbf{k}\cdot\mathbf{r}}\hat{\delta}_A(\mathbf{k}). \tag{3.36}$$

The covariance of two Fourier modes is

$$\langle \hat{\delta}_A(\mathbf{k}_1)\hat{\delta}_A(\mathbf{k}_2)\rangle = \int d\mathbf{r}_1 \int d\mathbf{r}_2\, e^{-i\mathbf{k}_1\cdot\mathbf{r}_1}e^{-i\mathbf{k}_2\cdot\mathbf{r}_2}\langle \delta_A(\mathbf{r}_1)\delta_A(\mathbf{r}_2)\rangle. \tag{3.37}$$

Changing the variable of integration $\mathbf{r}_1$ to $\mathbf{r} = \mathbf{r}_1 - \mathbf{r}_2$ makes the integrand $e^{-i\mathbf{k}_1\cdot\mathbf{r}_1} \times e^{-i\mathbf{k}_2\cdot\mathbf{r}_2}\xi_A(r)$ equal to $e^{-i\mathbf{k}_1\cdot\mathbf{r}}e^{-i(\mathbf{k}_1+\mathbf{k}_2)\cdot\mathbf{r}_2}\xi_A(r)$, which upon integration in $\mathbf{r}_2$ gives the three-dimensional Dirac delta function $\delta_{3D}(\mathbf{k}_1 + \mathbf{k}_2)$, expressing the hypothetical translational invariance or statistical homogeneity. Hence,

$$\langle \hat{\delta}_A(\mathbf{k}_1)\hat{\delta}_A(\mathbf{k}_2)\rangle = (2\pi)^3\, \delta_{3D}(\mathbf{k}_1 + \mathbf{k}_2) \int d\mathbf{r}\, e^{-i\mathbf{k}_1\cdot\mathbf{r}}\xi_A(r). \tag{3.38}$$

The remaining integral in eq. (3.38) is the Fourier transform (evaluated at $\mathbf{k}_1$) of the correlation function $\xi_A(r)$. We define it as the matter power spectrum

$$\mathcal{P}_A(k) \equiv \int d\mathbf{r}\, e^{-i\mathbf{k}\cdot\mathbf{r}}\xi_A(r) \tag{3.39}$$

and may alternatively express it, after integrating the angular part, as

$$\mathcal{P}_A(k) = 2\pi \int_0^\infty dr\, r^2 \frac{\sin(kr)}{kr}\xi_A(r). \tag{3.40}$$

The power spectrum $\mathcal{P}_A$ depends only on $k$, the modulus of $\mathbf{k}$, thus reflecting the statistical isotropy. Naturally, the correlation function is the inverse Fourier transform of the power spectrum:

$$\xi_A(r) = (2\pi)^{-3} \int d^3\mathbf{k}\, e^{-i\mathbf{k}\cdot\mathbf{r}}\mathcal{P}_A(k) = \int_0^\infty dk\, k^2 \frac{\sin(kr)}{kr}\mathcal{P}_A(k). \tag{3.41}$$

The correlation function and the power spectrum are equivalent descriptions of the statistical properties of the inhomogeneities. The statistical properties of the matter density field are completely characterized by the two-point correlation function or the power spectrum if the fluctuations are Gaussian (which means that

the phases of the Fourier modes $\hat{\delta}_{\mathrm{M}}(\mathbf{k})$ are uncorrelated and random as a consequence of the central limit theorem). The requirement is that the initial perturbations produced during inflation are Gaussian, since the linear evolution preserves the phases. Indeed, the primordial fluctuations have been shown highly Gaussian [54, 55]. However, in case non-Gaussianities are eventually detected, the three-point correlation function (or equivalently its Fourier space counterpart, the bispectrum) and higher order moments may be necessary to describe completely the statistical properties of the density field.

### 3.3.1 The galaxy correlation function, number density and bias

The matter density field cannot be directly observed since its composed mostly of dark matter. Instead, we can directly see the galaxies and study their discrete distribution, which is expected to trace the underlying matter field. This idea was introduced by Kaiser [56] in 1984 to explain the properties of Abell clusters, despite the already known fact that clustering properties of galaxies vary with their morphology [57, 58], so they cannot all be good tracers of the mass distribution [59]. This situation is eased, however, by the galaxy distribution, initially very biased when they were formed at high density regions of the matter fluctuation field, becoming less and less biased with time as its gravitational evolution takes place.

The galaxy overdensity is defined in terms of a mean galaxy number density $\bar{n}_{\mathrm{g}}$ rather than an energy density,

$$\delta_{\mathrm{g}}(\tau, \mathbf{r}) \equiv \frac{n_{\mathrm{g}}(\tau, \mathbf{r}) - \bar{n}_{\mathrm{g}}(\tau)}{\bar{n}_{\mathrm{g}}(\tau)}. \tag{3.42}$$

The relation between the galaxy and the total matter distribution is made by the galaxy bias $b(\tau, \mathbf{r})$,

$$\delta_{\mathrm{g}}(\tau, \mathbf{r}) = b(\tau, \mathbf{r})\delta_{\mathrm{M}}(\tau, \mathbf{r}). \tag{3.43}$$

The bias is a consequence of the non-linear nature of galaxy formation. Several different and complicated biasing schemes have been introduced in the literature. The simplest form of bias is a constant $b$, so the galaxy density contrast $\delta_{\mathrm{g}}$ is linearly biased, $\delta_{\mathrm{g}} = b\delta$. This assumption is justified by the indication that, on sufficiently large scales, galaxy bias is scale independent [60, 61]. The galaxy velocity field, on the other hand, follows exactly the matter velocity field, $\mathbf{v}_{\mathrm{g}} = \mathbf{v}_{\mathrm{M}}$. The correlation function and the power spectrum of galaxies will then be related to their matter counterparts by

$$\xi_{\mathrm{g}} = b^2 \xi_{\mathrm{M}} \quad \text{and} \quad \mathcal{P}_{\mathrm{g}} = b^2 \mathcal{P}_{\mathrm{M}}. \tag{3.44}$$

The probability of finding a galaxy centered in a random volume element $\mathrm{d}V$ is $\bar{n}_\mathrm{g}\,\mathrm{d}V$. The galaxy two-point correlation function $\xi_\mathrm{g}(r) = \langle \delta_\mathrm{g}(\mathbf{r}')\delta_\mathrm{g}(\mathbf{r}' + \mathbf{r}) \rangle$ can be interpreted as the excess probability, compared to that of a random distribution, that a pair of galaxies can be found at a distance $r$, as this probability can be written as $\mathrm{d}P = \bar{n}_\mathrm{g}^2 [1 + \xi_\mathrm{g}(r)]\,\mathrm{d}V_1\mathrm{d}V_2$.

# Chapter 4

# Redshift-space distortions

The distances of galaxies from us are usually inferred through the measured redshift, by the conversion of the redshift velocity to distance via Hubble's law. However, this is not exact. As we have seen in chapter 2, the formation of structures due to gravitational instabilities induce galaxies to have peculiar velocities that distort the uniform Hubble flow. What we actually measure with the redshift is the sum of the two contributions to the velocity of galaxies—the Hubble expansion velocity and the line-of-sight projection of the peculiar velocity,

$$cz = Hr + \mathbf{v} \cdot \hat{\mathbf{r}}. \tag{4.1}$$

Therefore, the direct interpretation of the distance as $cz/H$ is contaminated by the extra term $v/H \equiv \mathbf{v} \cdot \hat{\mathbf{r}}/H$ due to the peculiar velocity. The displacements of galaxies relative to their true positions in the redshift space when they possess peculiar velocity along the line of sight are what we call redshift-space distortions (RSDs).

Peculiar velocities constitute a powerful cosmic probe since they are related to the growth rate of structures [eq. (3.22)]. Redshift surveys have been used to constrain cosmological parameters. Peacock et al. [62] measure the amount of matter in the universe from clustering in the Two-degree-Field Galaxy Redshift Survey (2dFGRS). Verde et al. [59] also use the 2dFGRS data to complement their analysis of the CMB for parameter estimation from the WMAP observations with the matter power spectrum of the nearby universe. In this chapter, we will see how the RSDs look like in redshift space and how they affect the statistical properties that we studied in section 3.3, which is essential to learn how to compare theoretical predictions with observations of RSD.
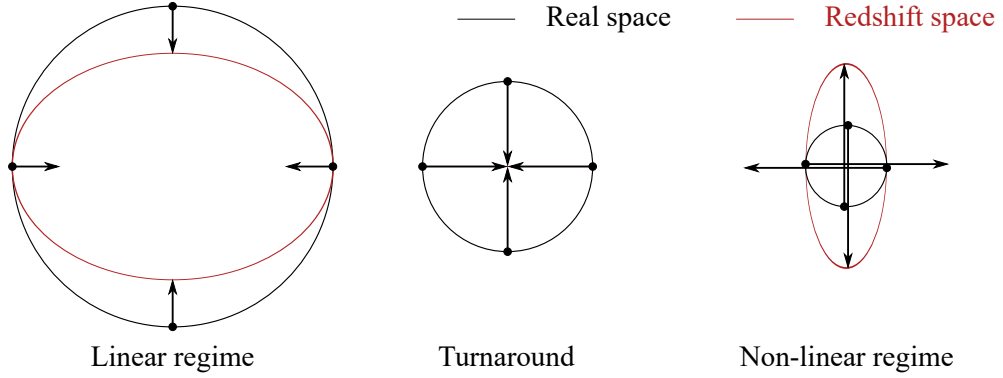
Figure 4.1: In the linear regime, a spherical density contrast appears squashed along the line of sight in redshift space. At smaller scales, velocities tend to be larger, originating the so-called fingers-of-god, appearing to be turned inside out. There is an intermediate point of turnaround, where the density contrast shell appears collapsed, when peculiar velocities in the line of sight exactly cancel the Hubble velocity.

## 4.1   Seeing the distortions in redshift space

We show schematically in figure 4.1 how the RSDs look like in redshift space for a radially symmetric distribution of galaxies. The galaxies, represented by dots, are falling towards the center with peculiar velocities represented by the arrows in the schematic image. All the galaxies on the same black circle (real space) have the same total peculiar velocity |**v**|. The observer is far away at some point below the undermost galaxy represented. Then, due to the effect produced by peculiar velocities, galaxies will appear, in redshift space, at the positions represented by the red ellipses. Coherent infall velocities of galaxies between the center of the distribution and the observer will add to the Hubble expansion, while the velocities of those galaxies behind the center of the density contrast will subtract from the Hubble flow.

  We can distinguish two regime scales. On large scales, for galaxies far from the center of the distribution, the distortion tends to be small because the gravitational pull is relatively weak. The distribution appears squashed along the line of sight. This is the so-called Kaiser effect. The situation changes at smaller scales, where virialized non-linear motions of galaxies closer to the center are composed of peculiar velocities that can even surpass the cosmic Hubble flow velocity, thus producing a smearing effect known as fingers-of-god. There is an intermediate point between the two regimes where the peculiar velocities exactly cancel out the Hubble flow velocity. In a real galaxy survey all these features are present, besides some other complicated characteristics about the coverage and the selec-

2dF Galaxy Redshift Survey

4° slice
63361 galaxies
141402 total
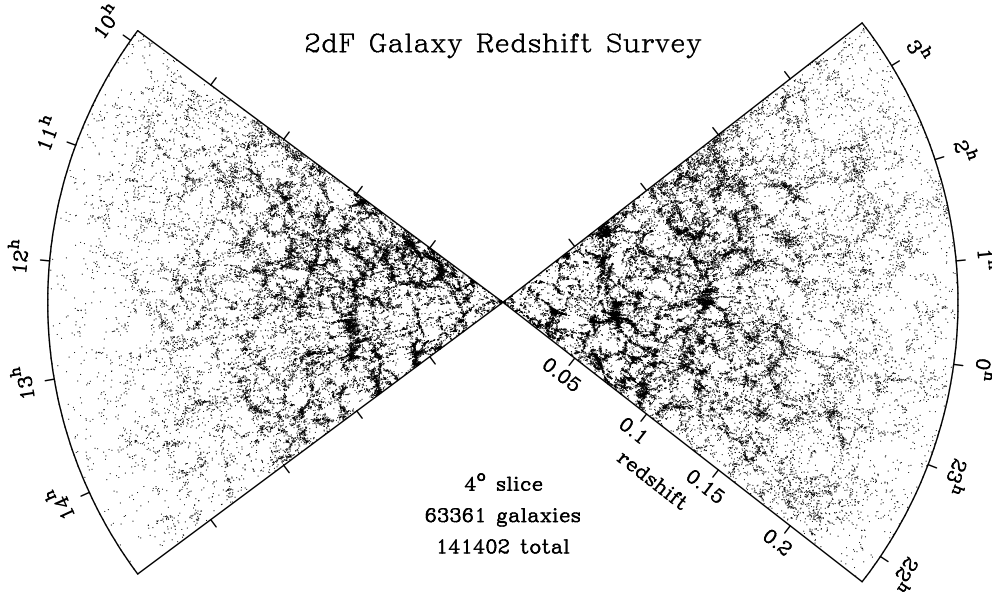
Figure 4.2: Distribution of galaxies in part of the 2dF galaxy survey, from Peacock et al. [62] (not all redshifts had been obtained at that time). The slices are 4° thick, centered at declination −2.5° in the northern galactic pole and −27.5° in the southern galactic pole.

tion of galaxies. For example, the 2dFGRS [62, 63] (figure 4.2) is a survey limited by magnitude; most nearby galaxies are included in the catalog but, as the distance increases, only the brighter galaxies are selected because of the flux-limited window function.

## 4.2   The linear theory

We have already deduced the continuity and Euler equations [eqs. (3.14)] for a (pressureless) fluid of matter in an expanding background in section 3.2. Before applying those results, a few important adjustments must be made. Those results give a good description of the clustering of the matter distribution field, which is composed mostly of dark matter. Of course we do not observe dark matter directly, but rather discrete galaxies, which can at least be assumed to trace the underlying distribution of matter, so the statistical properties of the structure of the universe can be studied by observing the galaxy distribution. Thus the study of the statistical properties of the galaxy distribution is of great importance for uncovering the features of the large-scale structure of the universe.

### 4.2.1 The redshift-space distortion parameter

With the linear bias assumption $\delta_g = b(z)\delta_M$, the continuity equation (3.22) for galaxies reads

$$\mathcal{H}af\frac{\delta_g}{b} + \theta_g = \mathcal{H}a\beta\,\delta_g + \theta_g = 0, \tag{4.2}$$

where have we introduced the so-called redshift-space distortion parameter

$$\beta(z) \equiv \frac{f(z)}{b(z)}. \tag{4.3}$$

This definition is more general than the simple constant bias. Nevertheless, it is usual to extract measurements of $b$, $f$ and $\beta$ assumed constant within redshift bins.

### 4.2.2 The correlation function and the power spectrum in redshift space

With the redshift-space galaxy density contrast $\delta_g^s(\mathbf{s})$ adequately defined in all redshift space, inside and outside the region of the survey [64], the redshift-space correlation function $\xi_g^s$ is defined by

$$\xi_g^s(s_{12}, s_1, s_2) \equiv \langle \delta_g^s(\mathbf{s}_1)\delta_g^s(\mathbf{s}_2) \rangle. \tag{4.4}$$

Unlike in the real-space case, the redshift-space correlation function depends not only on the separation $s_{12} \equiv |\mathbf{s}_1 - \mathbf{s}_2|$ of the galaxies in redshift space, but also in the redshift distances $s_1$ and $s_2$. Part of the symmetry present in $\xi_g(r_{12})$ is broken in redshift space due to the redshift distortions caused by the peculiar velocities of galaxies and possibly due to the heterogeneity of the selection function over different regions. However, the rotational symmetry about the observer at $s = 0$ is preserved, since the selection function does not depend on the direction of the vectors $\mathbf{s}_1$ and $\mathbf{s}_2$.

If the angle between $\mathbf{s}_1$ and $\mathbf{s}_2$ is small enough, then $\xi_g^s$ depends only on the parallel and perpendicular to the line of sight $\mathbf{z}$ components $s_\parallel$ and $s_\perp$ of the separation $s_{12}$. This is the plane-parallel (or distant-observer) approximation.

We also define the redshift Fourier modes $\hat{\delta}^s(\mathbf{k})$ in the same way of eqs. (3.35) and (3.36):

$$\hat{\delta}_g^s(\mathbf{k}) = \int d\mathbf{s}\, e^{-i\mathbf{k}\cdot\mathbf{s}}\delta_g^s(\mathbf{s}), \tag{4.5}$$

$$\delta_g^s(\mathbf{s}) = (2\pi)^{-3} \int d\mathbf{k}\, e^{i\mathbf{k}\cdot\mathbf{s}}\hat{\delta}_g^s(\mathbf{k}). \tag{4.6}$$

The redshift-space power spectrum, similarly to the real-space case, is the Fourier transform of the redshift-space correlation function. In the plane-parallel approximation,

$$\mathcal{P}_g^s(k_\parallel, k_\perp) \equiv \int d\mathbf{s} \, e^{-i\mathbf{k}\cdot\mathbf{s}} \xi_g^s(s_\parallel, s_\perp), \tag{4.7}$$

where $k_\parallel$ and $k_\perp$ are the parallel and perpendicular to the line-of-sight components of the wavevector $\mathbf{k}$.

As we saw in section 4.1, and now with the knowledge of the correlation function, we expect the contours of $\xi_g^s$ to be compressed along the line of sight by galaxies falling into overdense regions. This distortion of $\xi_g^s$ on large scales is known as the Kaiser effect. This effect offers a method for measuring the redshift-space distortion parameter $\beta$, which will then be detectable through the correlation function or the power spectrum. Figure 4.3 illustrates the distorted redshift-space correlation function computed for the 2dFGRS.

### 4.2.3   From real space to redshift space

Starting from the conservation of the number of galaxies in a survey, $n^s(\mathbf{s}) \, d\mathbf{s} = n(\mathbf{r}) \, d\mathbf{r}$, where $\mathbf{r}$ and $\mathbf{s} = \mathbf{r} + \frac{1}{H_0}\mathbf{v} \cdot \hat{\mathbf{r}}$ are the positions in real and redshift space, respectively, and $\mathbf{v}$ is the peculiar velocity field, it is possible to show [64, 65] that the observed Fourier modes of the galaxy density contrast in redshift space are related to the Fourier modes in real space by

$$\hat{\delta}_g^s(\mathbf{k}) = \left(1 + \beta\mu_{kz}^2\right)\hat{\delta}_g(\mathbf{k}) \tag{4.8}$$

in the plane-parallel (distant observer) approximation, where $\mu_{kz} \equiv \frac{1}{k}\mathbf{k} \cdot \hat{\mathbf{z}}$ is the cosine of the angle between the wavevector $\mathbf{k}$ and the line-of-sight direction $\hat{\mathbf{z}}$. It follows immediately that the power spectrum in redshift space is amplified by the square of that factor over the power spectrum in real space,

$$\mathcal{P}_g^s(\mathbf{k}) = \left(1 + \beta\mu_{kz}^2\right)^2 \mathcal{P}_g(k). \tag{4.9}$$

Galaxies moving perpendicularly to the observer have $\mu_{kz} = 0$ and are thus not affected. In the next section we show how the RSD parameter $\beta$ can be measured from the redshift-space power spectrum.
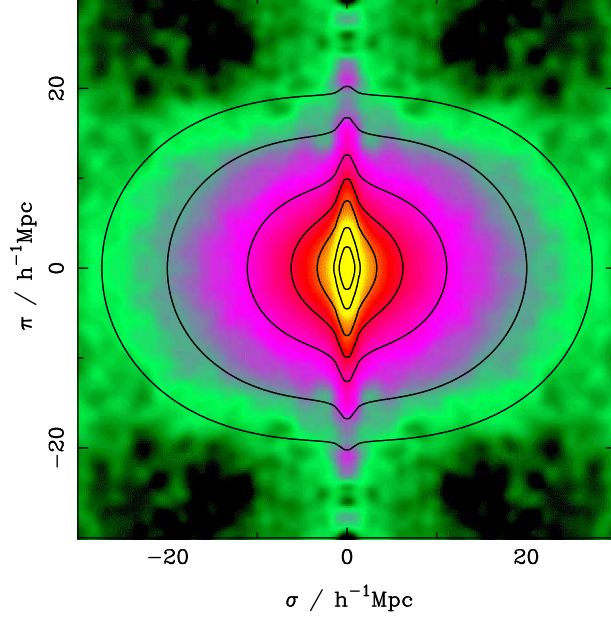
Figure 4.3: The redshift-space correlation function $\xi_g^s(\sigma, \pi)$ for the 2dFGRS as a function of the transverse ($\sigma$) and radial ($\pi$) pair separations, from Peacock et al. [62]. The data are measured only in the first quadrant and mirrored in both axes for the purpose of illustrating deviations from circular symmetry. Redshift distortions are clearly identified, both the fingers-of-god elongations at small scales and the Kaiser effect at large distances. Superimposed are the contours $\xi_g^s = 10, 5, 2, 1, 0.5, 0.2$ and $0.1$ showing model predictions with $\beta = 0.4$. A pairwise velocity dispersion of $400 \, \text{km s}^{-1}$ was used for modelling the small-scale effects.

## 4.3 Measuring the redshift-space distortion parameter

Here we will present some of the methods that have been used, for example, by Ratcliffe, Shanks, Parker & Fong [66], to obtain a measurement of the redshift-space distortion parameter.

### 4.3.1 The ratio of quadrupole-to-monopole moments of the redshift-space power spectrum

In the plane-parallel approximation, one can write the redshift-space power spectrum as a sum of even harmonics $\mathcal{P}_\ell^s(k)$:

$$\mathcal{P}_g^s(\mathbf{k}) = \sum_{\ell \text{ even}} \mathscr{P}_\ell(\mu_{kz}) \mathcal{P}_\ell^s(k), \tag{4.10}$$

where the harmonics are defined by

$$\mathcal{P}^s_\ell \equiv \frac{2\ell + 1}{4\pi} \int d\Omega_{\mathbf{k}} \, \mathscr{P}_\ell(\mu_{kz}) \mathcal{P}^s_g(\mathbf{k}), \tag{4.11}$$

$d\Omega_{\mathbf{k}}$ is the infinitesimal solid angle in Fourier space and $\mathscr{P}_\ell$ are the Legendre polynomials, given by

$$\mathscr{P}_\ell(\mu) = \frac{1}{2^\ell \ell!} \frac{d^\ell}{d\mu^\ell} \left[ (\mu^2 - 1)^\ell \right]. \tag{4.12}$$

The odd harmonics vanish by pair exchange symmetry and non-zero azimuthal harmonics ($Y_{\ell m}$ with $m \neq 0$) vanish by symmetry about the line of sight. In the linear regime, it can be shown that $\mathcal{P}^s_g(\mathbf{k})$ reduces to a sum of monopole, quadrupole and hexadecapole harmonics:

$$\mathcal{P}^s_g(\mathbf{k}) = \mathscr{P}_0(\mu_{kz})\mathcal{P}^s_0(k) + \mathscr{P}_2(\mu_{kz})\mathcal{P}^s_2(k) + \mathscr{P}_4(\mu_{kz})\mathcal{P}^s_4(k). \tag{4.13}$$

Substituting eq. (4.12) into eq. (4.11), it is easy to obtain each of these harmonics in terms of the true power spectrum. With $\mathscr{P}_0(\mu_{kz}) = 1$, $\mathscr{P}_2(\mu_{kz}) = \frac{1}{2}(3\mu^2_{kz} - 1)$ and $\mathscr{P}_4(\mu_{kz}) = \frac{1}{8}(3 - 30\mu^2_{kz} + 35\mu^4_{kz})$, the monopole term is

$$\begin{aligned}
\mathcal{P}^s_0(k) &= \frac{1}{4\pi} \int d\Omega_{\mathbf{k}} \left(1 + \beta\mu^2_{kz}\right)^2 \mathcal{P}_g(k) \\
&= \frac{1}{2} \int_{-1}^{1} d\mu_{kz} \left(1 + 2\beta\mu^2_{kz} + \beta^2\mu^4_{kz}\right) \mathcal{P}_g(k) \\
&= \left(1 + \frac{2}{3}\beta + \frac{1}{5}\beta^2\right) \mathcal{P}_g(k),
\end{aligned} \tag{4.14}$$

the quadrupole is

$$\begin{aligned}
\mathcal{P}^s_2(k) &= \frac{5}{4} \int_{-1}^{1} d\mu_{kz} \left(3\mu^2_{kz} - 1\right)\left(1 + 2\beta\mu^2_{kz} + \beta^2\mu^4_{kz}\right) \mathcal{P}_g(k) \\
&= \left(\frac{4}{3}\beta + \frac{4}{7}\beta^2\right) \mathcal{P}_g(k)
\end{aligned} \tag{4.15}$$

and the hexadecapole is given by

$$\begin{aligned}
\mathcal{P}^s_4(k) &= \frac{9}{16} \int_{-1}^{1} d\mu_{kz} \left(3 - 30\mu^2_{kz} + 35\mu^4_{kz}\right)\left(1 - \beta\mu^2_{kz}\right)^2 \mathcal{P}_g(k) \\
&= \frac{8}{35}\beta^2 \mathcal{P}_g(k).
\end{aligned} \tag{4.16}$$
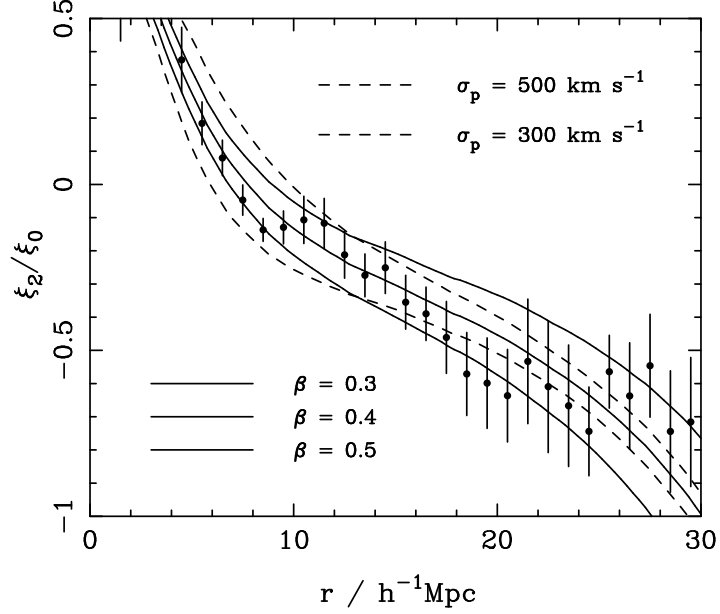
Figure 4.4: The quadrupole-to-monopole ratio $\xi_2^s/\xi_0^s$ as a function of the radii $r$, from Peacock et al. [62]. The quantity is positive at small scales, where the fingers-of-god effect dominates, and negative at large scales, dominated by coherent infall velocities. Solid lines show model predictions for $\beta = 0.3$, $0.4$ and $0.5$, with pairwise velocity dispersion $\sigma_p = 400\,\mathrm{km\,s^{-1}}$ for modelling the small-scale effects. The dashed lines are predictions for $\beta = 0.4$, with $\sigma_p = 300$ and $500\,\mathrm{km\,s^{-1}}$. The ratio becomes more negative as $\beta$ increases and as $\sigma_p$ decreases.

The hexadecapole harmonic is generally small and noisy, so it is of particular interest to compute the ratio of the quadrupole to the monopole harmonics of the redshift-space power spectrum:

$$\frac{\mathcal{P}_2^s(k)}{\mathcal{P}_0^s(k)} = \frac{\frac{4}{3}\beta + \frac{4}{7}\beta^2}{1 + \frac{2}{3}\beta + \frac{1}{5}\beta^2}. \tag{4.17}$$

This same result applies for the quadrupole-to-monopole ratio of the redshift-space correlation function $\xi_2^s/\xi_0^s$. Thus measuring the ratio of quadrupole-to-monopole moments of the redshift-space power spectrum (or correlation function) one can extract a measurement of the redshift-space distortion parameter $\beta$. The advantage of this method is that it uses quantities measured in redshift space only. Figure 4.4 shows the results for the quadrupole-to-monopole ratio of the redshift-space correlation function for the 2dFGRS at different radii.

### 4.3.2 The ratio of redshift-space to real-space angle-averaged power spectra

The redshift-space power spectrum $\mathcal{P}_g^s(\mathbf{k})$ depends on the wavevector $\mathbf{k}$ in Fourier space. This can be explicitly put as a dependence on the modulus $k$ and on the angle of $\mathbf{k}$ with the line-of-sight direction, that is, $\mathcal{P}_g^s(\mathbf{k}) = \mathcal{P}_g^s(k, \mu_{kz})$. If we integrate over all $\mu_{kz}$ we get the angle-averaged redshift-space power spectrum $\mathcal{P}_g^s(k)$ (the distinction with respect to the original redshift-space power spectrum $\mathcal{P}_g^s(\mathbf{k})$ is made clear by the explicit dependence on the modulus $k$ of the wavevector only):

$$\mathcal{P}_g^s(k) = \frac{\int_{-1}^{1} d\mu_{kz}\, \mathcal{P}_g^s(k, \mu_{kz})}{\int_{-1}^{1} d\mu_{kz}}. \tag{4.18}$$

With $\mathcal{P}_g^s(\mathbf{k})$ from eq. (4.9), this gives

$$\mathcal{P}_g^s(k) = \left[1 + \tfrac{2}{3}\beta + \tfrac{1}{5}\beta^2\right]\mathcal{P}_g(k). \tag{4.19}$$

A similar expression also applies for the angle-averaged correlation function, by inverse Fourier transforming the equation above:

$$\xi_g^s(s) = \left[1 + \tfrac{2}{3}\beta + \tfrac{1}{5}\beta^2\right]\xi_g(r). \tag{4.20}$$

Measurement of the real-space correlation function $\xi_g(r)$ is done by deprojecting the angular correlation function of a survey. Since this process is known to be noisy, the method just discussed is more appropriate for large surveys.

# Chapter 5

# The growth of structures in interacting dark energy models

We already obtained the evolution equations for fluid density and velocity perturbations in section 3.2 in a general fashion, allowing the presence of an interaction term in the energy-momentum tensor conservation equation. Specially for the matter fluid, we combined those equations with the Poisson equation in sub-horizon scales to get a second order differential equation (3.18) for $\delta_{\mathrm{M}}$ in the non-interacting case. Then, we have defined the growth rate of the matter perturbations as their logarithmic rate of change. We are now interested in seeing how the growth of structures is affected by the presence of interaction between dark energy and dark matter. The following study produced an interesting result from the theoretical point of view and has been submitted to the Journal of Cosmology and Astroparticle Physics for publication [6].

The fact that the evolution of the growth rate can be solved approximately in an analytic form,

$$f(z) \approx [\Omega_{\mathrm{M}}(z)]^{\gamma(z)}, \qquad (5.1)$$

is remarkable. The approximation was first proposed by Peebles [53] for the matter dominated universe as $f(z = 0) \approx (\Omega_{\mathrm{M},0})^{0.6}$, followed by the more accurate approximation $(\Omega_{\mathrm{M},0})^{4/7}$ by Lightman & Schechter [67]. More generally, the approximation was also derived in dynamical DE models with zero curvature and slowly varying EoS [68] and in curved spaces [69]; in modified gravity models, the approximate solution was given in refs. [70, 71]. This approximation has been shown very satisfactory until now for virtually any cosmological model without DE-DM coupling, with $\gamma$ varying accordingly (see, for example, Linder [72] and references therein). In the $\Lambda$CDM model, the growth index is approximately 6/11. Since growth of structures data spans a wide range of redshift and the growth index evolves with the redshift, it is worth exploring its parametrization as a function

of the redshift. This can help distinguish between DE models and modified gravity models [73, 74].

In order to investigate the influence of a DE-DM interaction on the growth of structures, we now consider a simplified model of the universe composed exclusively of dark energy and dark matter. Baryonic matter is not taken into account. The purpose of this chapter is to derive and present an analytical solution for the growth rate of (dark) matter perturbations as a function of the redshift in interacting DE models. A similar analysis is done by Simpson, Jackson & Peacock [75], although with slightly different model and parametrization. Our approach generalizes the method employed by Tsujikawa, Felice & Alcaniz [76] for the dynamical DE model without any interaction with DM. The derivation is based on the expansion of the growth index and of the DE EoS parameter in terms of the DE density parameter $\Omega_{DE}(z)$. We also derive an expression for the root mean square (RMS) amplitude of perturbations $\sigma_8(z)$ and show that when the DE equation of state, the coupling, the DE energy density and the amplitude of perturbations at present are given, the evolution history of the growth of structures is fully determined analytically. This analytic solution of the growth can help us see clearly the influence of the interaction between dark sectors in the growth. The analytic form of $f\sigma_8(z)$ thus obtained enables us to test the interacting DE model by using LSS observations.

We are going to analyze two different types of interacting DE models, one with an interacting term proportional to the DE density and other with a term proportional to the DM density. In a general way, we can combine equations (3.14) with the Poisson equation (3.17) to get a second order differential equation for $\delta_{DM}$ in the interacting case as well, without specifying the form of the interaction term $Q_0^{DM}$. The resulting equation is

$$\delta''_{DM} - (\mathscr{Q} - \mathscr{H}) \delta'_{DM} - \left( \frac{3}{2} \mathcal{H}^2 \Omega_{DM} + \mathscr{Q}' + \mathcal{H}\mathscr{Q} \right) \delta_{DM} = -\frac{ik^i \delta Q_i^{DM}}{\bar{\rho}_{DM}}, \qquad (5.2)$$

where we have defined

$$\mathscr{Q} \equiv \frac{\bar{Q}_0^{DM}}{\bar{\rho}_{DM}} - \frac{\delta Q_0^{DM}}{\bar{\rho}_{DM}\delta_{DM}} \qquad \text{and} \qquad \mathscr{H} \equiv \mathcal{H} - \frac{\bar{Q}_0^{DM}}{\bar{\rho}_{DM}}. \qquad (5.3)$$

In the following sections we specify the interaction according to the two cases we want to study.

# 5.1 The interacting model $Q_0^{\mathrm{DM}} \propto \rho_{\mathrm{DE}}$

We start with a model with an interaction term in the DM energy-momentum conservation equation that is proportional to the DE energy density,

$$\text{CDE:} \qquad Q_0^{\mathrm{DM}} = \bar{Q}_0^{\mathrm{DM}} = -3\mathcal{H}\zeta\bar{\rho}_{\mathrm{DE}}, \qquad (5.4)$$

where $\zeta$ is the coupling constant. The interaction in this coupled dark energy (CDE) model has only an unperturbed part, since we are neglecting DE clustering. With eq. (5.4), the background evolution eq. (3.12) reads

$$\bar{\rho}'_{\mathrm{DM}} + 3\mathcal{H}\bar{\rho}_{\mathrm{DM}} = 3\mathcal{H}\zeta\bar{\rho}_{\mathrm{DM}}\frac{1-\Omega_{\mathrm{DM}}}{\Omega_{\mathrm{DM}}}. \qquad (5.5)$$

Replacing $\bar{Q}_0^{\mathrm{DM}}/\bar{\rho}_{\mathrm{DM}} = -3\mathcal{H}\zeta\left(1-\Omega_{\mathrm{DM}}\right)/\Omega_{\mathrm{DM}}$ and $\delta Q_0^{\mathrm{DM}}/\bar{\rho}_{\mathrm{DM}}\delta_{\mathrm{DM}} = 0$, the evolution of the DM perturbations (5.2) reduces to

$$\delta''_{\mathrm{DM}} + \left(1 + 6\zeta\tfrac{1-\Omega_{\mathrm{DM}}}{\Omega_{\mathrm{DM}}}\right)\mathcal{H}\delta'_{\mathrm{DM}} -$$
$$- \tfrac{3}{2}\mathcal{H}^2\delta_{\mathrm{DM}}\left[\Omega_{\mathrm{DM}} - 2\zeta\tfrac{1-\Omega_{\mathrm{DM}}}{\Omega_{\mathrm{DM}}}\left(1 + \tfrac{\mathcal{H}'}{\mathcal{H}^2} + 3\zeta\tfrac{1-\Omega_{\mathrm{DM}}}{\Omega_{\mathrm{DM}}} - \tfrac{\Omega'_{\mathrm{DM}}}{\mathcal{H}\Omega_{\mathrm{DM}}}\tfrac{1}{1-\Omega_{\mathrm{DM}}}\right)\right] = 0. \quad (5.6)$$

The standard evolution $\delta''_{\mathrm{DM}} + \mathcal{H}\delta'_{\mathrm{DM}} - \tfrac{3}{2}\mathcal{H}^2\Omega_{\mathrm{DM}}\delta_{\mathrm{DM}} = 0$ is recovered when $\zeta = 0$. Due to the presence of the interaction, the coefficient of $\delta_{\mathrm{DM}}$ in eq. (5.6) can become positive as $\Omega_{\mathrm{DM}}$ decreases, leading to a decaying regime of the perturbation. It is evident that this negative growth rate cannot be described by the parametrization of $f$ with the growth index. This imposes a constraint on the values that the coupling can assume under this growth index parametrization, as we will se in section 5.1.3.

## 5.1.1 The growth of structure

To obtain the approximation $f \approx \Omega_{\mathrm{DM}}^{\gamma}$, we need to change the time derivatives $\partial/\partial\tau$ to $\partial/\partial a$ and write eq. (5.6) in terms of $f$. We can carry out a power series expansion for the functions in terms of $\Omega_{\mathrm{DE}}$ around zero, describing the time evolution in terms of the DE density parameter. In non-interacting models, a polynomial equation in $\Omega_{\mathrm{DE}}$ can be obtained by equating coefficients in both sides, with its zero-th order coefficients vanishing identically and its coefficients for higher orders in $\Omega_{\mathrm{DE}}$ giving the coefficients of $\gamma = \sum_{n=0}^{\infty} \gamma_n \left(\Omega_{\mathrm{DE}}\right)^n$ in terms of the coefficients of $w_{\mathrm{DE}} = \sum_{n=0}^{\infty} w_n \left(\Omega_{\mathrm{DE}}\right)^n$ (see, for example, Wang & Steinhardt [68]). This form of parametrization has been shown useful in obtaining the analytic expression of the growth index in dynamical DE models and convenient for distinguishing the model from the $\Lambda$CDM model [68, 76].

For the DE-DM interaction model, we adopt the same strategy as that of the non-interacting cases [76]. We do the expansion around $\Omega_{DE} = 0$ and assume that the ratio between the rate of change of the DE density parameter and the Hubble rate is negligible compared to the density parameter and to unity, at least in the regime of structure formation. Therefore, $\Omega'_{DE} \ll \mathcal{H}\Omega_{DE}$ in eq. (5.6) and we are led to

$$
\delta''_{DM} + \left(1 + 6\zeta\tfrac{1-\Omega_{DM}}{\Omega_{DM}}\right)\mathcal{H}\delta'_{DM} -
$$
$$
- \tfrac{3}{2}\mathcal{H}^2\delta_{DM}\left\{\Omega_{DM} + 2\zeta\tfrac{1-\Omega_{DM}}{\Omega_{DM}}\left[-\tfrac{1}{2} + 3w_{DE}(1-\Omega_{DM}) - 3\zeta\tfrac{1-\Omega_{DM}}{\Omega_{DM}}\right]\right\} = 0. \quad (5.7)
$$

After some manipulations, this is rewritten as

$$
\frac{d^2\ln\delta_{DM}}{d\ln a^2} + \left(\frac{d\ln\delta_{DM}}{d\ln a}\right)^2 + \left[\frac{1}{2} - \frac{3}{2}w_{DE}(1-\Omega_{DM}) + 6\zeta\frac{1-\Omega_{DE}}{\Omega_{DE}}\right]\frac{d\ln\delta_{DM}}{d\ln a} -
$$
$$
- \frac{3}{2}\Omega_{DM} + 3\zeta\frac{1-\Omega_{DM}}{\Omega_{DM}}\left[\frac{1-\Omega_{DM}}{\Omega_{DM}}(3\zeta - 3w_{DE}\Omega_{DM}) + \frac{1}{2}\right] = 0. \quad (5.8)
$$

Substituting $f$, we have

$$
\frac{df}{d\ln a} + f^2 + f\left[\frac{1}{2} - \frac{3}{2}w_{DE}(1-\Omega_{DM}) + 6\zeta\frac{1-\Omega_{DM}}{\Omega_{DM}}\right] - \frac{3}{2}\Omega_{DM} +
$$
$$
+ 3\zeta\frac{1-\Omega_{DM}}{\Omega_{DM}}\left[\frac{1-\Omega_{DM}}{\Omega_{DM}}(3\zeta - 3w_{DE}\Omega_{DM}) + \frac{1}{2}\right] = 0, \quad (5.9)
$$

which still has the first term parametrized by the scale factor. Next, we write

$$
\frac{df}{d\ln a} = \frac{d\Omega_{DM}}{d\ln a}\frac{df}{d\Omega_{DM}} \quad (5.10)
$$

and use the (background) energy conservation equations to substitute $\frac{d\Omega_{DM}}{d\ln a}$. The total conservation equation gives

$$
d\bar{\rho} + 3\tfrac{da}{a}(\bar{\rho} + \bar{p}) = 0,
$$
$$
d(a^3\bar{\rho}) = -d(a^3)w_{DE}\bar{\rho}_{DE},
$$
$$
d\left(\frac{a^3\bar{\rho}_{DM}}{\Omega_{DM}}\right) = -d(a^3)w_{DE}\bar{\rho}_{DM}\frac{1-\Omega_{DM}}{\Omega_{DM}}, \quad (5.11)
$$

where we have used $\bar{\rho} = \frac{\bar{\rho}_{DM}}{\Omega_{DM}}$ and $\bar{\rho}_{DE} = \bar{\rho}_{DM}\frac{1-\Omega_{DM}}{\Omega_{DM}}$, while the DM equation gives

$$
d\bar{\rho}_{DM} + 3\tfrac{da}{a}\bar{\rho}_{DM} = 3\tfrac{da}{a}\zeta\bar{\rho}_{DM}\frac{1-\Omega_{DM}}{\Omega_{DM}},
$$
$$
d(a^3\bar{\rho}_{DM}) = \zeta\bar{\rho}_{DM}\frac{1-\Omega_{DM}}{\Omega_{DM}}d(a^3), \quad (5.12)
$$

which can be inserted back in eq. (5.11) to give

$$\zeta\bar{\rho}_{\text{DM}}\frac{1-\Omega_{\text{DM}}}{\Omega_{\text{DM}}}\frac{\text{d}(a^3)}{\Omega_{\text{DM}}} - a^3\bar{\rho}_{\text{DM}}\frac{\text{d}\Omega_{\text{DM}}}{\Omega_{\text{DM}}^2} = -w_{\text{DE}}\bar{\rho}_{\text{DM}}\frac{1-\Omega_{\text{DM}}}{\Omega_{\text{DM}}}\text{d}(a^3),$$

$$3\zeta(1-\Omega_{\text{DM}})\,\text{d}\ln a - \text{d}\Omega_{\text{DM}} = -3w_{\text{DE}}\Omega_{\text{DM}}(1-\Omega_{\text{DM}})\,\text{d}\ln a,$$

$$\frac{\text{d}\Omega_{\text{DM}}}{\text{d}\ln a} = 3(1-\Omega_{\text{DM}})(\zeta + w_{\text{DE}}\Omega_{\text{DM}}). \tag{5.13}$$

Substituting eq. (5.13) into eq. (5.10) and dividing eq. (5.9) by $f$ we have

$$3(\zeta + w_{\text{DE}}\Omega_{\text{DM}})\frac{1-\Omega_{\text{DM}}}{f}\frac{\text{d}f}{\text{d}\Omega_{\text{DM}}} + f + \frac{1}{2} - \frac{3}{2}w_{\text{DE}}(1-\Omega_{\text{DM}}) + 6\zeta\frac{1-\Omega_{\text{DM}}}{\Omega_{\text{DM}}} -$$

$$-\frac{3}{2}\frac{\Omega_{\text{DM}}}{f} + 3\zeta\frac{1-\Omega_{\text{DM}}}{f\Omega_{\text{DM}}}\left[\frac{1-\Omega_{\text{DM}}}{\Omega_{\text{DM}}}(3\zeta - 3w_{\text{DE}}\Omega_{\text{DM}}) + \frac{1}{2}\right] = 0. \tag{5.14}$$

Finally, expanding eq. (5.14) around $\Omega_{\text{DE}} = 0$ with $f = (\Omega_{\text{DM}})^{\gamma_0 + \gamma_1\Omega_{\text{DE}} + \cdots}$, we arrive at the polynomial equation

$$[3(1-w_0+5\zeta) - \gamma_0(5-6w_0-6\zeta)]\Omega_{\text{DE}} + \frac{1}{2}\Big[-\gamma_0^2 + \gamma_0(1+12w_1+18\zeta) -$$

$$- 2\gamma_1(5-12w_0-12\zeta) - 6w_1 + 6\zeta(5-6w_0+6\zeta)\Big]\Omega_{\text{DE}}^2 + O(\Omega_{\text{DE}}^3) = 0. \tag{5.15}$$

The zero-th order part is still identically zero even with non-zero $\zeta$. The equations of the higher order terms can be solved to give the modified growth index coefficients

$$\gamma_0 = \frac{3(1-w_0+5\zeta)}{5-6w_0-6\zeta}, \tag{5.16a}$$

$$\gamma_1 = \frac{-\gamma_0^2 + \gamma_0(1+12w_1+18\zeta) - 6w_1 + 6\zeta(5-6w_0+6\zeta)}{2(5-12w_0-12\zeta)}, \tag{5.16b}$$

$$\vdots$$

We note that positive $\zeta$ increases $\gamma_0$, the dominant part of the growth index. The well-known result $\gamma_0 = \frac{3(1-w_0)}{5-6w_0}$ is recovered when $\zeta = 0$, giving $\gamma_0 = 6/11$ for $\Lambda$CDM. With the standard values $w_0 = -1$ and $\zeta = 0$, the first-order coefficient is $\gamma_1 = \frac{3(5+11w_1)}{2057}$, which may give a rather small contribution $\gamma_1\Omega_{\text{DE}}$ to $\gamma$ for a slowly varying EoS parameter.

Predictions made with $f = (\Omega_{\text{DM}})^{\gamma_0 + \gamma_1\Omega_{\text{DE}} + \cdots}$ can, in principle, be compared to growth rate measurements like those compiled in Dossett et al. [74]. Those data, however, are generally obtained from measurements of the RSD parameter

$\beta = f/b$, where $b$ is the bias measuring how galaxies trace the matter density field, and thus can be bias-dependent. Usually, it is preferable to compare predictions with the bias-independent data of $f\sigma_8$ [33], the growth rate multiplied by the variance of the density field filtered at a scale $R = 8\,h^{-1}$ Mpc, defined as

$$\sigma_R^2(z) \equiv \frac{1}{2\pi^2} \int_0^\infty \mathrm{d}k\, k^2 \mathcal{P}_{\mathrm{DM}}(k,z)\, |W(kR)|^2 \,, \tag{5.17}$$

where $P(k,z)$ is the matter power spectrum and $W(kR)$ is the window function of the experiment in Fourier space. We derive $\sigma_8$ from $\delta_{\mathrm{DM}}$ starting with the definition of $f$,

$$\frac{\mathrm{d}\Omega_{\mathrm{DM}}}{\mathrm{d}\ln a}\frac{\mathrm{d}\ln\delta_{\mathrm{DM}}}{\mathrm{d}\Omega_{\mathrm{DM}}} = (\Omega_{\mathrm{DM}})^\gamma \quad \Rightarrow$$

$$\Rightarrow \quad 3\,(1-\Omega_{\mathrm{DM}})\,(\zeta + w_{\mathrm{DE}}\Omega_{\mathrm{DM}})\frac{\mathrm{d}\ln\delta_{\mathrm{DM}}}{\mathrm{d}\Omega_{\mathrm{DM}}} = (\Omega_{\mathrm{DM}})^\gamma \quad \therefore$$

$$\therefore \quad \frac{\mathrm{d}\ln\delta_{\mathrm{DM}}}{\mathrm{d}\Omega_{\mathrm{DE}}} = -\frac{(1-\Omega_{\mathrm{DE}})^\gamma}{3\Omega_{\mathrm{DE}}\left[\zeta + w_{\mathrm{DE}}\,(1-\Omega_{\mathrm{DE}})\right]}. \tag{5.18}$$

We integrate backwards in $\Omega_{\mathrm{DE}}$ from $\Omega_{\mathrm{DE},0}$ to $\Omega_{\mathrm{DE}}(z)$ and expand it to obtain

$$\ln\frac{\delta_{\mathrm{DM}}}{\delta_{\mathrm{DM},0}} = \ln\left(\frac{\Omega_{\mathrm{DE}}}{\Omega_{\mathrm{DE},0}}\right)^{-1/3\tilde{w}_0} + \frac{\gamma_0 - \bar{\omega}_{01}}{3\tilde{w}_0}\,(\Omega_{\mathrm{DE}} - \Omega_{\mathrm{DE},0}) -$$

$$- \frac{1}{6\tilde{w}_0}\left[\frac{\gamma_0^2}{2} - \gamma_0\left(\frac{1}{2} + \bar{\omega}_{01}\right) - \gamma_1 + \frac{1}{\tilde{w}_0}\left(w_0\bar{\omega}_{01} - w_2 + \frac{w_1\tilde{w}_1}{\tilde{w}_0}\right)\right]\left(\Omega_{\mathrm{DE}}^2 - \Omega_{\mathrm{DE},0}^2\right) +$$

$$+ O(\Omega_{\mathrm{DE}}^3) + O(\Omega_{\mathrm{DE},0}^3) \tag{5.19}$$

where we have introduced the definitions

$$\tilde{w}_n \equiv w_n + \zeta \qquad \text{and} \qquad \bar{\omega}_{01} \equiv \frac{w_0 - w_1}{\tilde{w}_0}. \tag{5.20}$$

The time dependence of $\delta_{\mathrm{DM}}$ is parametrized by $\Omega_{\mathrm{DE}}$. $\delta_{\mathrm{DM},0}$ and $\Omega_{\mathrm{DE},0}$ represent their values today. Eq. (5.19) then gives, up to the second order in $\Omega_{\mathrm{DE}}$ and $\Omega_{\mathrm{DE},0}$,

$$\delta_{\mathrm{DM}}(z) = \delta_{\mathrm{DM},0}\mathcal{D}_{\mathrm{DM}}(z;0), \tag{5.21}$$

with

$$\mathcal{D}_{\mathrm{DM}}(z;0) \equiv \left[\frac{\Omega_{\mathrm{DE}(z)}}{\Omega_{\mathrm{DE},0}}\right]^{-1/3\tilde{w}_0} \exp\left[\frac{\varepsilon_1\Delta_{\mathrm{DE}}^{(1)} + \varepsilon_2\Delta_{\mathrm{DE}}^{(2)}}{3\tilde{w}_0}\right] \tag{5.22}$$

the backward propagation function for the evolution of the DM perturbation, as analogously defined in eq. (3.20) for the matter perturbation, and

$$\varepsilon_1 \equiv \gamma_0 - \bar{\omega}_{01}, \tag{5.23}$$

$$\varepsilon_2 \equiv -\frac{\gamma_0^2}{4} + \frac{\gamma_0}{2}\left(\frac{1}{2} + \bar{\omega}_{01}\right) + \frac{\gamma_1}{2} - \frac{1}{2\tilde{w}_0}\left(w_0\bar{\omega}_{01} - w_2 + w_1\frac{\tilde{w}_1}{\tilde{w}_0}\right), \tag{5.24}$$

$$\Delta_{\mathrm{DE}}^{(n)} \equiv \Omega_{\mathrm{DE}}^n(z) - \Omega_{\mathrm{DE},0}^n. \tag{5.25}$$

Noting that $\mathcal{P}_{\mathrm{DM}}(k,z) = [\mathcal{D}_{\mathrm{DM}}(z;0)]^2 \mathcal{P}_{\mathrm{DM},0}(k)$ and $\mathcal{D}_{\mathrm{DM}}$ is scale-independent, it follows directly from the definition (5.17) that $\sigma_R^2 = \mathcal{D}_{\mathrm{DM}}^2 \sigma_{R,0}^2$, i.e., $\sigma_R$ satisfies the same equation (5.21) for $\delta_{\mathrm{DM}}$. Thus, at the scale $R = 8\,h^{-1}$ Mpc, we have

$$\sigma_8(z) = \sigma_{8,0}\left[\frac{\Omega_{\mathrm{DE}}(z)}{\Omega_{\mathrm{DE},0}}\right]^{-1/3\tilde{w}_0} \exp\left[\frac{\varepsilon_1\Delta_{\mathrm{DE}}^{(1)} + \varepsilon_2\Delta_{\mathrm{DE}}^{(2)}}{3\tilde{w}_0}\right], \tag{5.26}$$

also up to the second order in $\Omega_{\mathrm{DE}}$ and $\Omega_{\mathrm{DE},0}$. Note that there can be some inaccuracy in the computation of $\sigma_8(z)$ from eq. (5.26), since we are integrating a function that has been expanded around $\Omega_{\mathrm{DE}} = 0$ from redshift zero, where $\Omega_{\mathrm{DE}}$ is not so small, until $z$. This has the consequence of the errors of the expansion at low redshifts being accumulated for $\sigma_8$ at any redshift and constitutes a limitation of the method. We also note that if $|w_1|$ or $|w_2|$ is too large, it is possible that they can make the exponential in eq. (5.26) grow enormously.

For the evaluation of $\Omega_{\mathrm{DE}}(z)$, we have to use a recursive relation. The DM and DE densities, in terms of the redshift, are

$$\bar{\rho}_{\mathrm{DM}}(z) = \bar{\rho}_{\mathrm{DM},0}\exp\left[\int_0^z \frac{3}{1+\tilde{z}}\left(1 - \zeta\frac{\Omega_{\mathrm{DE}}}{1 - \Omega_{\mathrm{DE}}}\right)\mathrm{d}\tilde{z}\right], \tag{5.27a}$$

$$\bar{\rho}_{\mathrm{DE}}(z) = \bar{\rho}_{\mathrm{DE},0}\exp\left[\int_0^z \frac{3}{1+\tilde{z}}\left[1 + w_{\mathrm{DE}}(\tilde{z}) + \zeta\right]\mathrm{d}\tilde{z}\right]. \tag{5.27b}$$

The term $w_{\mathrm{DE}}^{\mathrm{eff}} \equiv w_{\mathrm{DE}} + \zeta$ in eq. (5.27b) can be seen as an effective DE equation of state within the alternative framework where the interaction term is absorbed into the equation of state and there is no net transfer of energy-momentum between DE and DM.

The zero-th order DE density parameter is obtained by setting $w_{\mathrm{DE}} = w_0$ and neglecting the term $\zeta\frac{\Omega_{\mathrm{DE}}}{1-\Omega_{\mathrm{DE}}} \approx \zeta\Omega_{\mathrm{DE}} + \zeta\Omega_{\mathrm{DE}}^2$,

$$\Omega_{\mathrm{DE}}^{(0)} = \frac{\bar{\rho}_{\mathrm{DE}}^{(0)}}{\bar{\rho}_{\mathrm{DE}}^{(0)} + \bar{\rho}_{\mathrm{DM}}^{(0)}} = \frac{\Omega_{\mathrm{DE},0}\,(1+z)^{3\tilde{w}_0}}{1 - \Omega_{\mathrm{DE},0} + \Omega_{\mathrm{DE},0}\,(1+z)^{3\tilde{w}_0}}. \tag{5.28}$$

Table 5.1: Stability conditions of the CDE model.

| Constant EoS | Interaction sign | Condition |
|---|---|---|
| $w_{\mathrm{DE}} < -1$ | $\zeta < 0$ | early-time instability |
| $w_{\mathrm{DE}} < -1$ | $\zeta > 0$ | stable |
| $-1 < w_{\mathrm{DE}} < 0$ | $\zeta < 0$ | stable |
| $-1 < w_{\mathrm{DE}} < 0$ | $\zeta > 0$ | early-time instability |

Now the density parameter up to the first order is calculated by using $w_{\mathrm{DE}} = w_0 + w_1 \Omega_{\mathrm{DE}}^{(0)}$ and $\zeta \frac{\Omega_{\mathrm{DE}}}{1 - \Omega_{\mathrm{DE}}} = \zeta \Omega_{\mathrm{DE}}^{(0)}$,

$$\Omega_{\mathrm{DE}}^{(1)}(z) = \frac{\Omega_{\mathrm{DE},0} (1+z)^{3\tilde{w}_0} \left[1 - \Omega_{\mathrm{DE},0} + \Omega_{\mathrm{DE},0} (1+z)^{3\tilde{w}_0}\right]^{\tilde{w}_1/\tilde{w}_0}}{1 - \Omega_{\mathrm{DE},0} + \Omega_{\mathrm{DE},0} (1+z)^{3\tilde{w}_0} \left[1 - \Omega_{\mathrm{DE},0} + \Omega_{\mathrm{DE},0} (1+z)^{3\tilde{w}_0}\right]^{\tilde{w}_1/\tilde{w}_0}} \quad (5.29)$$

With equations (5.16), (5.26) and (5.29) we are now able to compute $f(z)$ and $\sigma_8(z)$ in this coupled model provided that we know the parameters $\zeta$, $w_n$, $\sigma_{8,0}$ and $\Omega_{\mathrm{DE},0}$. Once we know the coupling, DE EoS coefficients, DE density parameter and the mean perturbation amplitude at present we can determine analytically how structures have evolved and can compare these results with LSS observations.

## 5.1.2 Stability conditions

Interacting DE models with constant EoS have already been shown to suffer from instabilities with respect to curvature and dark energy perturbations [77, 78]. Depending on some combinations of the sign of the interaction and on the dark energy EoS being of the quintessence or phantom type, $\delta_{\mathrm{DE}}$ and the potential $\phi$ (in the perturbation of the metric) can blow up. Table 5.1 summarizes the allowed regions for the interaction and the DE equation of state parameters in the CDE model as shown by Gavela et al. [79], which extends the model stability analysis of He, Wang & Abdalla [78] to negative values of $\zeta$.

These results strongly restrict the parameter space for interacting DE. As those references point out, such instabilities can be avoided by allowing the EoS to vary with time, which we do when we expand $w_{\mathrm{DE}}$ in terms of $\Omega_{\mathrm{DE}}$. However, before considering a time variable EoS, first we simplify our models by fixing $w_1$ so we have one less parameter to be constrained with the Markov Chain Monte Carlo (MCMC) method. We proceed in the next section to compare our results for the growth rate with numerical calculations provided by a modified version of the Code for Anisotropies in the Microwave Background (CAMB) [80], in order to assess the reliability of our expressions and validate the method.

### 5.1.3 Comparison with full numerical computations in CAMB

To test how effective our analytical result of the growth in the CDE model is, we compare it with the numerical $f(z)$ obtained in a modified version of CAMB[1] for the interacting model.[2] We are going to show that our analytic solution can be trusted and we can further use it to estimate the cosmological parameters with a MCMC code, as a shortcut alternative to the full numerical computation to speed up the calculation.

We fix $w_1 = 0$ and $\Omega_{\mathrm{DE},0} = 0.7$ and calculate $f(z)$ with $z$ ranging from 0 to 10. According to the stability conditions given in the last section, the interaction constant in CDE can be negative, in which case the dark energy EoS must be of quintessence type, or the coupling be positive with phantom type DE EoS. We then fix $w_0 = -0.999$ and test the interaction constants $\zeta = -0.1, -0.01, -0.001$ and $w_0 = -1.001$ with $\zeta = 0.001, 0.01, 0.1$. To distinguish these two tests, we name the models, respectively, coupled phantom-like dark energy (CPDE) and coupled quintessence-like dark energy (CQDE). The comparisons are shown in figure 5.1 through the modulus of the difference $\Delta f \equiv f_{\mathrm{anl}} - f_{\mathrm{num}}$ divided by $f_{\mathrm{num}}$ (left panel), where "anl" and "num" stand for analytical and numerical computations. Over the range of the RSD data (low redshift until $z \sim 1$), for a given $\zeta$, the discrepancy grows as we approach $z = 0$, which is expected from the fact that $\Omega_{\mathrm{DE},0}$ is as big as 0.7. The discrepancy tends to decrease as $z$ increases, but only until a certain redshift, when it can start to grow, albeit slowly. In the $\zeta = 0.1$ case, $f_{\mathrm{num}}$ can become negative and the discrepancy is huge. This occurs because as $z$ decreases, $\frac{1-\Omega_{\mathrm{DM}}}{\Omega_{\mathrm{DM}}}$ increases and the second term inside the curly brackets in eq. (5.7) dominates the coefficient of $\delta_{\mathrm{DM}}$ and changes its sign, leading to a negative growth. The analytical parametrization $(\Omega_{\mathrm{DM}})^\gamma$, on the other hand, obviously can never become negative. The numerical result for $\zeta = -0.1$ shows that $f$ grows very rapidly at small redshifts as $z$ goes to zero, a behavior that is opposite to the other cases. This is due to a change of sign in the coefficient of $\delta'_{\mathrm{DM}}$ (Hubble drag) in eq. (5.7). We discard the cases $\zeta = -0.1$ and $\zeta = 0.1$ as they are not well described by eq. (5.1) and restrict $\zeta$ within the interval $[-0.01, 0]$ for the CQDE model and $[0, 0.01]$ for the CPDE model, which allow the difference between the numerical and the analytical results to be kept below about $10\%$ (with the other parameters fixed at reasonable values). The cusps observed in the curves of $|\Delta f / f_{\mathrm{num}}|$ in the two models mean a change of sign of $\Delta f$. The fact that the ana-

---

[1] CAMB is a cosmological Boltzmann code commonly used for calculating theoretical radiation and matter power spectra, among other things, given the cosmological parameters of the standard $\Lambda$CDM model or some of its derivatives.

[2] The model implemented in CAMB differed slightly from the analytical model by the presence of a baryonic component, accounting for $4\%$ of the total energy density, which did not have a perceptible influence on the comparisons.
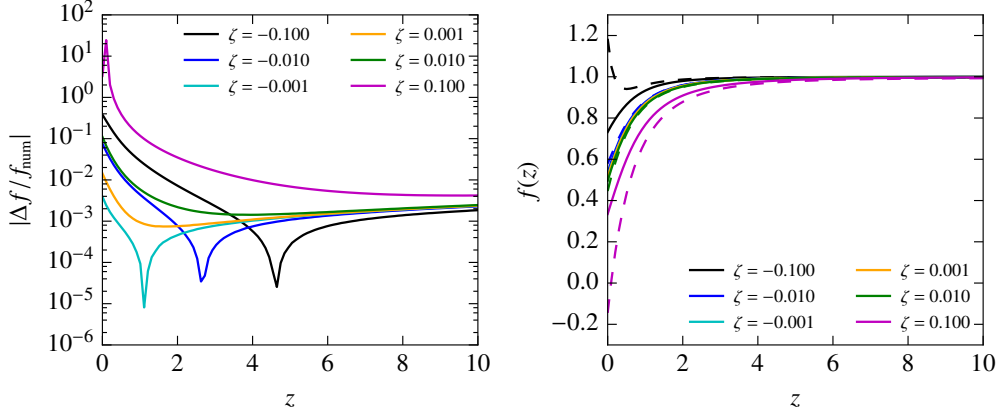
Figure 5.1: Comparison between analytical and numerical computations of $f(z)$ for the CDE model. In the left panel, the modulus of the relative differences, in logarithmic scale; in the right panel, the dashed lines represent the numerical results for $f(z)$, while the solid lines show our analytical results.

lytical and numerical curves cross themselves instead of converging to a common plateau, with $f_{num}$ becoming smaller than $f_{anl}$ as $z$ becomes larger, might indicate some contribution of a decaying mode of the perturbation, which is out of the scope of this work.

The conclusion is that the MCMC analysis can be made using the analytic approximations derived for $f$ in the interacting DE model, provided the parameters are restricted to the region where the discrepancy with respect to the numerical reference from CAMB is reasonably small. In section 5.3 we will present the RSD data that we use to estimate the parameters of our interacting models via MCMC.

## 5.2 The interacting model $Q_0^{DM} \propto \rho_{DM}$

We have also analyzed the case of an interaction proportional do the DM density,

$$Q_0^{DM} = -3\mathcal{H}\zeta\rho_{DM}. \tag{5.30}$$

The perturbed spatial part is $\delta Q_i^{DM}$ is set to zero. The background evolution is given by

$$\bar{\rho}'_{DM} + 3\mathcal{H}\bar{\rho}_{DM} = 3\mathcal{H}\zeta\bar{\rho}_{DM}. \tag{5.31}$$

The evolution of the DM perturbations comes from eq. (5.2) with $\frac{\bar{Q}_0^{DM}}{\bar{\rho}_{DM}} = \frac{\delta Q_0^{DM}}{\bar{\rho}_{DM}\delta_{DM}} = -3\mathcal{H}\zeta$, giving

$$\delta''_{DM} + (1 + 3\zeta)\mathcal{H}\delta'_{DM} - \frac{3}{2}\mathcal{H}^2\Omega_{DM}\delta_{DM} = 0. \tag{5.32}$$

This functional form of this equation is even simpler than the CDE case of section 5.1 with respect to the standard evolution, with only one extra term proportional to $\zeta$.

### 5.2.1 The growth of structure

In terms of $f$, with $\frac{d\Omega_{DM}}{d\ln a} = 3\Omega_{DM}\left[\zeta + w_{DE}\left(1 - \Omega_{DM}\right)\right]$, the growth rate evolution equation is

$$3\left[w_{DE}\left(1 - \Omega_{DM}\right) + \zeta\right]\frac{\Omega_{DM}}{f}\frac{df}{d\Omega_{DM}} + f + \frac{1}{2} - \frac{3}{2}w_{DE}\left(1 - \Omega_{DM}\right) + 3\zeta - \frac{3}{2}\frac{\Omega_{DM}}{f} = 0,$$
(5.33)

which expanded in $\Omega_{DE}$ for $f = (\Omega_{DM})^{\gamma_0 + \gamma_1\Omega_{DE} + \cdots}$ gives the polynomial equation

$$3\zeta\left(1 + \gamma_0\right) + \frac{1}{2}\left[3\left(1 - w_0\right) - \left(5 - 6w_0\right)\gamma_0 + 12\zeta\gamma_1\right]\Omega_{DE} +$$
$$+ \frac{1}{4}\left[-\gamma_0{}^2 + 36\zeta\gamma_2 + 2\gamma_1(12w_0 - 5 - 3\zeta) + (1 + 12w_1)\gamma_0 - 6w_1\right]\Omega_{DE}^2 +$$
$$+ O(\Omega_{DE}^3) = 0.$$
(5.34)

Unlike eq. (5.15), this now has a zero-th order part that does not vanish identically regardless of the interaction or other parameters. In order for eq. (5.34) to hold, $3\zeta\left(1 + \gamma_0\right) = 0$ must be satisfied. This implies $\zeta = 0$, recovering the non-interacting results for $\gamma$ from the higher order terms, or $\gamma_0 = -1$ and $\gamma_1 = \frac{9w_0 - 8}{12\zeta}$ (with $\zeta \neq 0$) from the first-order coefficient, which does not seem to fit the observed growth unless perhaps with a fine tuning of the parameters. Also, note that this solution implies a non-smooth transition to zero interaction. Although numerically the growth rate in this model can still be, to some degree, well approximated by the power law $\Omega_{DM}^\gamma$ form, as claimed by Linder [72], analytically we can see that this form is not appropriate for a non-zero coupling in the interaction term proportional to $\rho_{DM}$.

## 5.3 Observational constraints

In this section we present the dataset used to constrain the parameters of our CDE model. However, an adjustment to our growth rate $f$, calculated in a universe where DM and DE interact, is needed before comparing with $f\sigma_8$ data obtained assuming a standard cosmology. We explain in detail how the comparison must be made, then describe the statistical method employed in the analysis and discuss our results.

Table 5.2: Observed growth rate data and their respective references.

| $z$ | $f\sigma_8(z)$ | Ref. | $z$ | $f\sigma_8(z)$ | Ref. |
|---|---|---|---|---|---|
| 0.02 | $0.360 \pm 0.040$ | [82] | 0.40 | $0.419 \pm 0.041$ | [83] |
| 0.067 | $0.423 \pm 0.055$ | [84] | 0.41 | $0.450 \pm 0.040$ | [85] |
| 0.10 | $0.37 \ \pm 0.13$ | [86] | 0.50 | $0.427 \pm 0.043$ | [83] |
| 0.17 | $0.510 \pm 0.060$ | [33, 87] | 0.57 | $0.427 \pm 0.066$ | [88] |
| 0.22 | $0.420 \pm 0.070$ | [85] | 0.60 | $0.430 \pm 0.040$ | [85] |
| 0.25 | $0.351 \pm 0.058$ | [89] | 0.60 | $0.433 \pm 0.067$ | [83] |
| 0.30 | $0.407 \pm 0.055$ | [83] | 0.77 | $0.490 \pm 0.180$ | [33, 90] |
| 0.35 | $0.440 \pm 0.050$ | [33, 91] | 0.78 | $0.380 \pm 0.040$ | [85] |
| 0.37 | $0.460 \pm 0.038$ | [89] | 0.80 | $0.47 \ \pm 0.08$ | [92] |

## 5.3.1 The data

One way of measuring the growth of structures is through the effect of redshift-space distortions. We have seen in section 4.2 that the galaxy power spectrum $\mathcal{P}^s$ observed in redshift space is expected to be amplified with respect to the real power spectrum $\mathcal{P}(k)$ by a factor that depends on the growth rate and on the cosine of the angle between the movement of the galaxies and the observation, according to eq. (4.9). Multipole analysis of the anisotropy of the redshift-space power spectrum or correlation function in the redshift survey allows the observational determination of $\beta$, as we have also seen in section 4.3. Thus one gets the measurement $\beta\sigma_{8,g} = f\sigma_{8,M}$ of the growth of structure. The advantage of using $f\sigma_8$ rather than just $f$ to compare with model predictions is that the estimator $\beta\sigma_{8,g}$ is independent of the bias model. Also, the determination of $\beta$ is affected only weakly by changes in the cosmology (through the determination of distances) [33, 81].

In table 5.2 we list measurements of growth rate with their errors for various redshifts from different surveys like the 2dFGRS, the Six-degree-Field Galaxy Survey (6dFGS), the Sloan Digital Sky Survey (SDSS), the Baryon Oscillation Spectroscopic Survey (BOSS) and the WiggleZ dark energy survey. Most of those data are measured using RSD and others are based on direct measurements of peculiar velocities [82, 93, 94] or galaxy luminosities [86].

**Corrections to the growth rate due to the altered continuity equation**

In a standard cosmology, the coherent motion of galaxies is connected to the growth rate through the galaxy continuity equation $\theta_g = -\mathcal{H}\beta\delta_g$, built upon the matter continuity equation $\theta_M = -\mathcal{H}f_M\delta_M$ with the density bias assumption $\delta_g = b\delta_M$ and without any bias for the velocities ($\theta_g = \theta_M$). Whether the RSD parameter $\beta$ is measured from the power spectrum or from peculiar velocities, the $f\sigma_8$

data are based on the correspondence between $f/b$ and the velocity divergence as established by the continuity equation. When an interacting matter component is involved, these continuity equations do not hold anymore. We will now see what quantity corresponds to the velocity divergence $\theta_g$ in an interacting DE model.

We need to start over from the baryons and DM continuity equations in the interacting model to write a continuity equation for matter on which a continuity equation for galaxies can be based. The two matter fluids now behave differently, one coupled to the dark energy fluid and the other uncoupled. For baryons, we still have $\delta_b' + \theta_b = 0$. With $Q_0^{DM} = -3\mathcal{H}\zeta\bar{\rho}_{DE}$, the DM continuity equation was obtained in section 3.2,

$$\delta_{DM}' + 3\mathcal{H}\zeta\frac{\bar{\rho}_{DE}}{\bar{\rho}_{DM}}\delta_{DM} + \theta_{DM} = 0. \tag{5.35}$$

Since the matter density $\rho_M$ is the sum of the densities $\rho_b$ and $\rho_{DM}$, the matter perturbation is $\delta_M = (\bar{\rho}_b\delta_b + \bar{\rho}_{DM}\delta_{DM})/\bar{\rho}_M$ and its time derivative is

$$\delta_M' = -3\mathcal{H}\zeta\frac{\bar{\rho}_{DE}}{\bar{\rho}_M}\delta_M - \frac{\bar{\rho}_b\theta_b + \bar{\rho}_{DM}\theta_{DM}}{\bar{\rho}_M} \tag{5.36}$$

where we have also used the background evolution equations of each component from eq. (3.12). Substituting the time derivative,

$$\mathcal{H}\left(\frac{\mathrm{d}\ln\delta_M}{\mathrm{d}\ln a} + 3\zeta\frac{\bar{\rho}_{DE}}{\bar{\rho}_M}\right)\delta_M + \frac{\bar{\rho}_b\theta_b + \bar{\rho}_{DM}\theta_{DM}}{\bar{\rho}_M} = 0. \tag{5.37}$$

Recognizing $\theta_M$ by the term $(\bar{\rho}_b\theta_b + \bar{\rho}_{DM}\theta_{DM})/\bar{\rho}_M$, as usual, gives the continuity equation altered by the interaction

$$\mathcal{H}\tilde{f}_M\delta_M + \theta_M = 0, \tag{5.38}$$

where $\tilde{f}_M \equiv f_M + 3\zeta\frac{\bar{\rho}_{DE}}{\bar{\rho}_M}$ is the modified growth rate, with the usual $f_M \equiv \frac{\mathrm{d}\ln\delta_M}{\mathrm{d}\ln a}$.

We maintain the assumption that galaxies trace the matter field via $\delta_g = b\delta_M$ and $\theta_g = \theta_M = \theta$, so the galaxy continuity equation is now

$$\mathcal{H}\tilde{\beta}\delta_g + \theta = 0, \tag{5.39}$$

with $\tilde{\beta} \equiv \tilde{f}/b$. Therefore, this modified growth rate function is the quantity that effectively corresponds to the coherent motion of galaxies if there is an interaction between DM and DE according to the CDE model considered here. Also, the RSD parameter that is effectively measured from the power spectrum is $\tilde{\beta}$, since the modeling of the Kaiser effect, including its nonlinear features, relies on a continuity equation like eq. (5.39)[3] to substitute the velocity divergence in favor of the

---

[3]Higher-order terms are generally neglected in the continuity equation.

density multiplied by the (thus modified) growth rate. The same argument applies about the treatment of nonlinear effects like the Fingers-of-God (FoG) (see, for example, refs. [95, 96]). We then just need to add the term $3\zeta\frac{\bar{\rho}_{DE}}{\bar{\rho}_{M}}$ to the growth rate $f_{DM} = \Omega_{DM}^{\gamma}$ obtained in section 5.1.1 before comparing those predictions to the $f\sigma_8$ data. In our simplified model with the matter sector composed of dark matter only, without baryonic matter, the modified growth rate is $\tilde{f}_{DM} = f_{DM} + 3\zeta\frac{1-\Omega_{DM}}{\Omega_{DM}}$.

## 5.3.2    The statistical method

We perform a posterior likelihood analysis with flat priors for the parameters. In order to do that, we employ our analytic formula in computing the theoretical growth, implement it in a MCMC program in python and carry out the data fitting by using a simple Metropolis algorithm [97–99]. The proposal function in the algorithm is a multivariate normal distribution centered at the current state of the Markov chain. Its covariance matrix is a diagonal matrix where each diagonal element is equal to the square of a fraction of the prior interval of its corresponding parameter, adjusted by hand to give an acceptance ratio roughly between 0.2 and 0.5 in the Metropolis algorithm [98]. The likelihoods are computed as $\log \mathcal{L} = -\sum_{i=1}^{N} \log\left(\sigma_i \sqrt{2\pi}\right) - \chi^2/2$, with

$$\chi^2 = \sum_{i=1}^{N} \frac{\left[f\sigma_8^{(obs)}(z_i) - \tilde{f}\sigma_8^{(th)}(z_i)\right]^2}{\sigma_i^2}. \tag{5.40}$$

$N$ is the number of points in the dataset, $\sigma_i$ the errors in the measurements, "obs" stands for the observed data and "th" is our theoretical prediction by using the analytic formula on the growth. We then compute the unnormalized posterior $P(X|D) \propto P(D|X)\pi(X)$ for the parameter-space point $X$ given the dataset $D$, according to the Bayesian theorem, where $P(D|X)$ is the likelihood $\mathcal{L}$ and $\pi(X)$ is the prior. Our MCMC code evolves the chains checking for convergence after each $N_{steps}$ and keeps running until they match the convergence criteria. The starting points are chosen randomly with uniform probability within the prior ranges for each parameter.

### Convergence criterion

For monitoring the convergence of the chains, we implemented the multivariate extension by Brooks & Gelman [100] of the method proposed by Gelman & Rubin [101]. Having the starting points of eight chains chosen randomly, we run the chains through $2N$ iterations discarding the first $N$ to avoid the burn-in period. The choice of discarding half of chain sample is an attempt to maximize the efficiency

in the convergence diagnosis. Keeping more iterations would make the samples vary too little, causing the detection to be attained later than necessary.

Let us consider a $p$-dimensional vector parameter $\theta$, a random variable with mean vector $\mu$ and variance $\sigma^2$ which we want to estimate through the MCMC method with $m$ independent chains. We write $\theta_{jt}^{(i)}$ denoting its $i$-th element in chain $j$ at time (step) $t$. We take the estimate $\hat{\mu} = \bar{\theta}_{..}$, with the bar denoting an average over the set corresponding to the index that has been replaced with a dot. In this case, the average is over the sequence of $N$ elements of the sample chain and then over the $m$ chains. To estimate the variance, we calculate the $p$-dimensional between-chain covariance matrix $B/N$ defined by

$$\frac{B}{N} = \frac{1}{m-1} \sum_{j=1}^{m} (\bar{\theta}_{j\cdot} - \bar{\theta}_{..})(\bar{\theta}_{j\cdot} - \bar{\theta}_{..})^{\dagger} \tag{5.41}$$

and the within-chain covariance matrix

$$W = \frac{1}{m(N-1)} \sum_{j=1}^{m} \sum_{t=1}^{N} (\theta_{jt} - \bar{\theta}_{j\cdot})(\theta_{jt} - \bar{\theta}_{j\cdot})^{\dagger}. \tag{5.42}$$

The covariance matrix $\sigma^2$ could be estimated by a weighted average of $B$ and $W$,

$$\hat{\sigma}_{+}^2 = \frac{N-1}{N} W + \frac{B}{N}. \tag{5.43}$$

However, this would be an unbiased estimate of the true covariance $\sigma^2$ only if the starting points of the chains were drawn from the target distribution. Instead, this overestimates $\sigma^2$ if the distribution of the starting points is appropriately overdispersed, as it needs to be in order for the MCMC algorithm to sample a large volume of the parameter space thus enabling the algorithm to be more likely to detect the eventual existence of multiple modes in the distribution. We account for the sampling variability of $\hat{\mu}$ using the covariance estimate

$$\hat{V} = \hat{\sigma}_{+}^2 + \frac{B}{mN} = \frac{N-1}{N} W + \left(1 + \frac{1}{m}\right) \frac{B}{N}. \tag{5.44}$$

We can then monitor $\hat{V}$ and $W$, determining convergence when a certain distance measure between the two covariance matrices indicates that they are satisfactorily close. This distance must be a rotationally invariant measure. In the one-dimensional case, we would use the square root of the variance ratio $R = (\hat{V}/\sigma^2)^{1/2}$, which is called the scale reduction factor (SRF), or better yet its overestimate $\hat{R} = (\hat{V}/W)^{1/2}$, underestimating $\sigma^2$, unknown, by $W$. This is the potential scale reduction factor (PSRF). In the multidimensional case, the multivariate potential scale reduction factor (MPSRF) is a scalar measure that approaches 1 (from

above) as convergence is achieved. It is given by the maximum SRF of the linear projection of $\theta$ along any arbitrary vector $\alpha$,

$$\hat{R}^p = \left( \max_{\alpha} \frac{\alpha^\dagger \hat{V} \alpha}{\alpha^\dagger W \alpha} \right)^{1/2}. \tag{5.45}$$

It is possible to show [102], however, that $(\hat{R}^p)^2$ is equal to the largest eigenvalue of the positive definite matrix $W^{-1}\hat{V}$, as long as both $\hat{V}$ and $W$ are nonsingular, positive definite and symmetric.

Convergence is achieved when $\hat{R}^p - 1$ is smaller than some required precision $\epsilon$. In our runs, which we describe next, we sought for convergence within $\epsilon \sim 10^{-6}$, the $\Lambda$CDM case going even further at $\epsilon \sim 10^{-7}$, a higher precision achieved without extra computational cost due to the reduced number of parameters in the $\Lambda$CDM model.

### 5.3.3 The results

For comparison purposes, we first constrain a simple $\Lambda$CDM model with the two free parameters $\sigma_{8,0}$ and $\Omega_{DE,0}$. Their best-fit values are used in the subsequent analysis when we compare the fitting of our models to the $\Lambda$CDM's fitting with the same data in the end of this section. The $f\sigma_8$ data from table 5.2 provide the following $1\sigma$ confidence level (CL) for the parameters: $\sigma_{8,0} = 0.7195^{+0.0440}_{-0.0415}$, $\Omega_{DE,0} = 0.6889^{+0.0606}_{-0.0691}$, with the best-fit values $\sigma_{8,0} = 0.7266$ and $\Omega_{DE,0} = 0.6864$ (see figure 5.2). The priors used, always flat in this and in all subsequent analyses, were [0.4, 1.0] for both parameters and we summarize the results in table 5.3. The growth rate determined by the EoS parameters is

$$\Lambda\text{CDM:} \qquad f(\Omega_{DM}) = (\Omega_{DM})^{0.5455 + 0.0073(1 - \Omega_{DM})} \tag{5.46}$$

regardless of the resulting best-fit $\sigma_{8,0}$ and $\Omega_{DE,0}$. The growth index today is $\gamma = 0.5505$, up to first order in $\Omega_{DE}$. In the following, we present the results for the interacting DE models.

**The coupled DE models**

Besides $\Omega_{DE,0}$ and $\sigma_{8,0}$, CDE has other free parameters: $w_0$, $w_1$ and the coupling constant $\zeta$. However, before trying to constrain all these parameters together, we first fix $w_1 = 0$ and see if we can have a good indication of $w_0 \neq -1$. Not being able to constrain $w_0$ alone in the equation of state means that we will certainly not be able to constrain $w_0$ and $w_1$ together. We show in figure 5.3 the effect of the interaction on $\tilde{f}(z)$, $\sigma_8(z)$ and on the product $\tilde{f}\sigma_8(z)$ with $\Omega_{DE,0}$ and $\sigma_{8,0}$ fixed at their $\Lambda$CDM best-fit values and with $w_0 \to -1$. In 5.3a (top panel) we can clearly
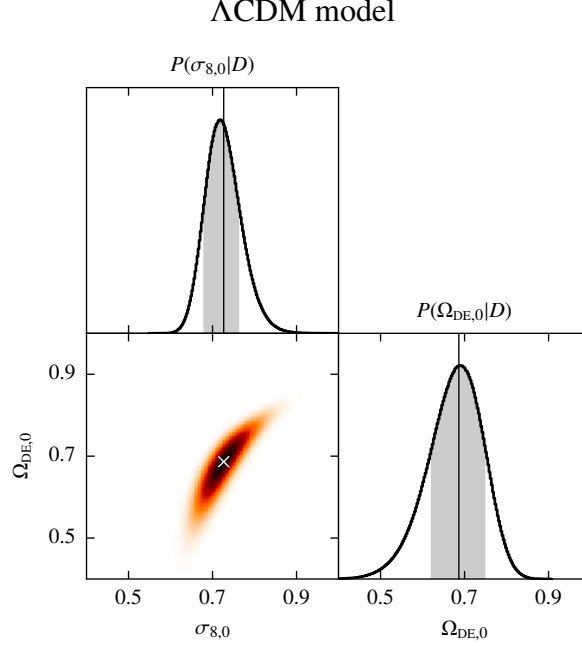
ΛCDM model



Figure 5.2: Histograms for the values of the DE density parameter and dark matter RMS fluctuation today at the scale of $8\,h^{-1}$ Mpc in the ΛCDM model. The vertical thin lines mark the best-fit values, and the grey area under the histograms show the $1\sigma$ CL. In the 2D histogram, the colors map the parameter space points to their unnormalized posterior values, from white (lowest values) to black (highest values), with shades of orange representing intermediate values. The white cross marks the best-fit point.

see influence of the interaction on the growth rate. The coupling $\zeta$ causes a shift of opposite sign to the growth rate $f$ (not shown), but a larger shift of equal sign to the modified rate $\tilde{f}$, the shift getting larger as $z$ gets closer to zero. The impact of the interaction on $\sigma_8$ (bottom panel is barely perceptible.

We choose the priors based on our comparison with the numerical result for $f(z)$, given in section 5.1.3. As discussed in section 5.1, in order to avoid changing the sign of the coefficient of $\delta_{DM}$ and to keep discrepancies with respect to the numerical solutions small, values of $\zeta$ should be small, of the order $10^{-2}$, so we use the prior $[0, 0.01]$ for $\zeta$ in the phantom case and $[-0.01, 0]$ in the quintessence case. $\Omega_{DE,0}$ can be assumed any value in the interval $(0.0, 1.0)$.

Table 5.3 summarizes the priors and the fitting results and we show in figures 5.4 and 5.5a the marginalized distributions for CPDE and CQDE, respectively. We prefer to express the $1\sigma$ CL intervals of the unconstrained parameters without reporting a central value. Because of the large uncertainties of the data, the method was not able to constrain $w_0$ and $\zeta$ with $f\sigma_8$ data alone, as can be seen
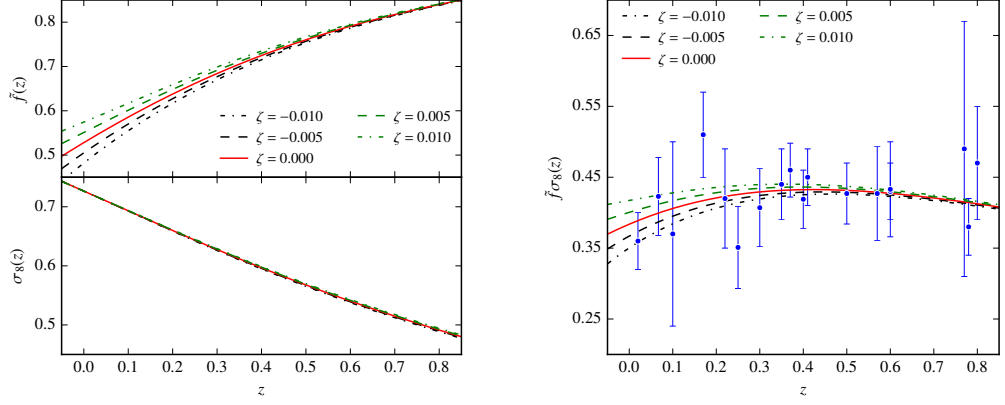
(a) Effect of $\zeta$ on $\tilde{f}(z)$ (top) and $\sigma_8(z)$ (bottom panel).

(b) Influence of different values of $\zeta$ on the product $\tilde{f}\sigma_8$.

Figure 5.3: Evolution of the growth of structures in the coupled DE model for varying values of the coupling $\zeta$. The negative values (black lines) correspond to the CQDE model and the positive values (green lines) to the CPDE model. In both cases we use $w_0 = -1$ for simplification, since we are interested in seeing the effect of the coupling only. The red line is the $\Lambda$CDM result. The data from table 5.2 are also plotted in (b).

from the histograms of the marginalized distributions. This hints the fact that such set of parameters can only be better constrained if we combine the $f\sigma_8$ data with other kinds of observations, e.g. the CMB. The best-fit values encountered lead to the growth rates

$$\text{CPDE:} \qquad f(\Omega_{\text{DM}}) = (\Omega_{\text{DM}})^{0.5371+0.0058(1-\Omega_{\text{DM}})} \,, \qquad (5.47)$$

$$\text{CQDE:} \qquad f(\Omega_{\text{DM}}) = (\Omega_{\text{DM}})^{0.5290-0.0147(1-\Omega_{\text{DM}})} \,, \qquad (5.48)$$

for the two models as functions of $\Omega_{\text{DM}}$. The best-fit $\Omega_{\text{DE},0}$ gives, for each model, the growth index today $\gamma = 0.5410$ and $\gamma = 0.5194$ respectively, up to first order in the density parameter.

**On the unconstrained parameters**

The models considered in our work cannot have all their parameters satisfactorily constrained due to the large uncertainties in the measurements of the large-scale structure. This difficulty motivated us to try to obtain a more conclusive determination of the interaction constant by fixing one more parameter, $w_0$ in the equation of state. We analyze the case of CQDE with the EoS fixed in its best-fit value $w_0 = -0.997728$. The choice of CQDE over CPDE is because this class of mod-

Table 5.3: Priors, best-fit values and $1\sigma$ CL ranges for the parameters of all models. Central values are shown only for reasonably well constrained parameters.

| Model | Parameter | Prior | Best-fit | $1\sigma$ CL |
|---|---|---|---|---|
| $\Lambda$CDM | $\sigma_{8,0}$ | $[0.4, 1.0]$ | $0.7266$ | $0.7195^{+0.0440}_{-0.0415}$ |
| | $\Omega_{\mathrm{DE},0}$ | $[0.4, 1.0]$ | $0.6864$ | $0.6889^{+0.0606}_{-0.0691}$ |
| CPDE | $\zeta$ | $[0.00, 0.01]$ | $7.8 \times 10^{-5}$ | $[0.0034, 0.0100]$ |
| | $\sigma_{8,0}$ | $[0.2, 1.4]$ | $0.6750$ | $0.6322^{+0.0473}_{-0.0293}$ |
| | $\Omega_{\mathrm{DE},0}$ | $(0.0, 1.0]$ | $0.6712$ | $0.6939^{+0.0652}_{-0.0731}$ |
| | $w_0$ | $[-3.0, -1.0)$ | $-1.4173$ | $[-2.1042, -1.0000]$ |
| CQDE | $\zeta$ | $[-0.01, 0.00]$ | $-0.0100$ | $[-0.0069, 0.0000]$ |
| | $\sigma_{8,0}$ | $[0.2, 1.4]$ | $0.7230$ | $0.7513^{+0.1262}_{-0.0598}$ |
| | $\Omega_{\mathrm{DE},0}$ | $(0.0, 1.0]$ | $0.6533$ | $0.7032^{+0.0667}_{-0.0705}$ |
| | $w_0$ | $(-1.0, -0.3]$ | $-0.9977$ | $[-1.0000, -0.5552]$ |
| $w$CQDE | $\zeta$ | $[-0.01, 0.00]$ | $-0.0100$ | $[-0.0100, -0.0031]$ |
| | $\sigma_{8,0}$ | $[0.2, 1.4]$ | $0.7240$ | $0.7166^{+0.0412}_{-0.0386}$ |
| | $\Omega_{\mathrm{DE},0}$ | $(0.0, 1.0]$ | $0.6546$ | $0.6737^{+0.0512}_{-0.0702}$ |

els gives, according to Gavela et al. [79], the best fit to LSS data.[4] We then run this CQDE model with the EoS parameters fixed at $w_0 = -0.997728$ and $w_1 = 0$, which we call fixed-$w$ coupled quintessence-like dark energy ($w$CQDE). The results are shown in figure 5.5b and in table 5.3. We have obtained the growth rate

$$w\text{CQDE:} \qquad f(\Omega_{\mathrm{DM}}) = (\Omega_{\mathrm{DM}})^{0.5290-0.0147(1-\Omega_{\mathrm{DM}})}, \qquad (5.49)$$

with today's value of the growth index $\gamma = 0.5194$. This pretty much coincides with the CQDE result, since the best-fit values of all parameters are practically identical.

We see that even when we keep the equation of state fixed, although the region of $1\sigma$ CL has been considerably reduced for $\sigma_{8,0}$ and $\Omega_{\mathrm{DE},0}$, the growth of structure data cannot constrain very well all the parameters either because the measurements are not very precise or the prior is too tight. Relaxing this prior for $\zeta$ would compromise the analysis, as the results for $f$ would not be so reliable, as discussed in section 5.1.3. This last result reinforces the need of additional observables in order to get fully satisfactory constraints and make assertive conclusions about a possible detection of a DE-DM interaction.

Indeed, Yang & Xu [103] used CMB, BAO and SNe Ia in addition to $f\sigma_8$ data to constrain an interacting $w$CDM model (IwCDM) which is equivalent to our

---

[4]Which model gives the best fit to the data that we used here could be evaluated by comparing their Bayesian evidences. However, this analysis is out of the scope of this work.
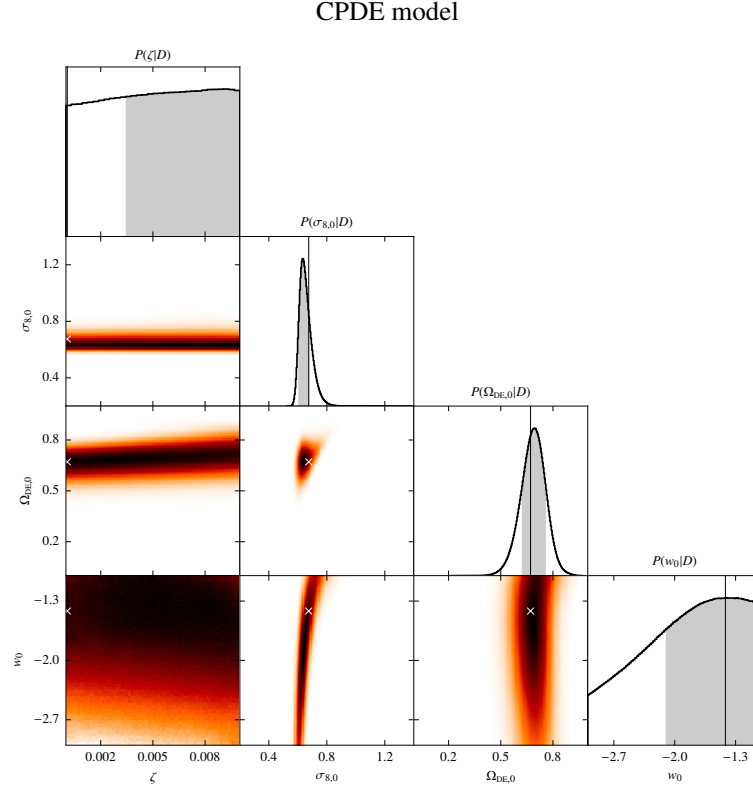
CPDE model



Figure 5.4: Histograms for the free parameters of CPDE. The vertical thin lines mark the best-fit values, and the grey area under the histograms show the $1\sigma$ CL. In the 2D histograms, the colors map the parameter space points to their unnormalized posterior values, from white (lowest values) to black (highest values), with shades of orange representing intermediate values. The white crosses mark the best-fit point. Due to the large uncertainties in the measurements of $f\sigma_8(z)$, the data could not constrain the interaction and the EoS parameter.

CQDE model. Murgia, Gariazzo & Fornengo [104] also combined CMB temperature and polarization, gravitational lensing and supernovae data with BAO/RSD data to constrain their models MOD1 and MOD2, identical to our models CQDE and CPDE, respectively. Costa, Xu, Wang & Abdalla [105] have combined the latest Planck CMB data, BAO, SNe Ia, $H_0$ and RSD data to constrain several parameters of their models, which also include our models CQDE and CPDE (models I and II in ref. [105]). In all these works, the authors obtained the growth by numerically computing the perturbation equations and compared with observational datasets. Their results are consistent with our treatment by employing the analytic formula on computing the growth. All these results converge that $f\sigma_8$ data alone
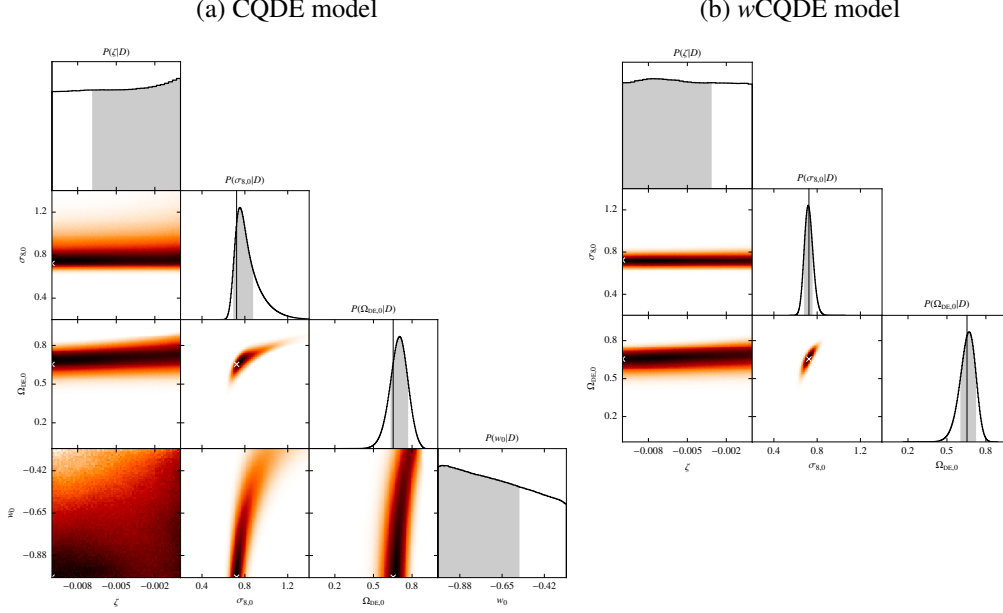
(a) CQDE model · (b) *w*CQDE model



Figure 5.5: Marginalized posterior distributions for (a) CQDE and (b) *w*CQDE models. The vertical thin lines mark the best-fit values, while the grey areas under the histograms in the diagonal show the $1\sigma$ CL. In the 2D histograms, the colors map the parameter space points to their unnormalized posterior values, from white (lowest values) to black (highest values), with shades of orange representing intermediate values. The white crosses mark the best-fit point. As we can see from the results of *w*CQDE, fixing the EoS parameter is not sufficient to constrain the interaction coupling in the already too tight prior.

cannot help to constrain well the model parameters due to the large uncertainty of the current data.

**Comparing the growth in different models**

In figure 5.6 we plot separately each of the interacting models' best-fit $\tilde{f}\sigma_8(z)$, together with the $\Lambda$CDM's best-fit over the redshift range of the data. We note that the best-fit $\tilde{f}\sigma_8(z)$ in the CDE models is generally lower than that in $\Lambda$CDM, but as the redshift decreases, it surpasses $\Lambda$CDM around redshift $z = 0.5$ and becomes smaller again around $z = 0.1$, the difference being slightly larger in the CPDE case (left panel) due to the best-fit point more distant from the $\Lambda$CDM best-fit.

The discrepancies between the models become more apparent when we look at the $1\sigma$ ranges and at the functions $\tilde{f}(z)$, $\sigma_8(z)$ and $\gamma(z)$ separately. In order to do that, we perform linear error propagation on the fitted parameters. We simplify
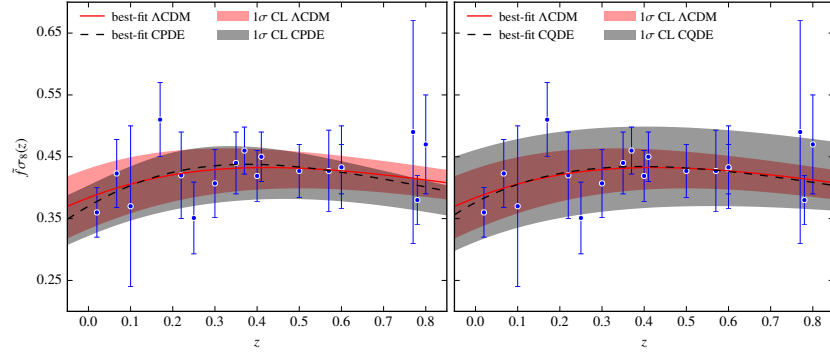
Figure 5.6: Comparisons of best-fit and $1\sigma$-range $\tilde{f}\sigma_8(z)$ between CPDE and $\Lambda$CDM (left panel) and between CQDE and $\Lambda$CDM (right panel). The blue data points are listed in table 5.2.



Figure 5.7: Comparisons of best-fit and $1\sigma$-range $f(z)$ (upper panels) and $\sigma_8(z)$ (lower panels) between CPDE and $\Lambda$CDM (left panels) and between CQDE and $\Lambda$CDM (right panels).
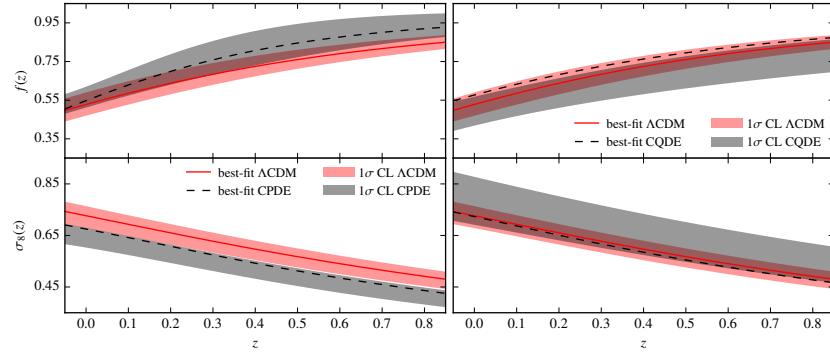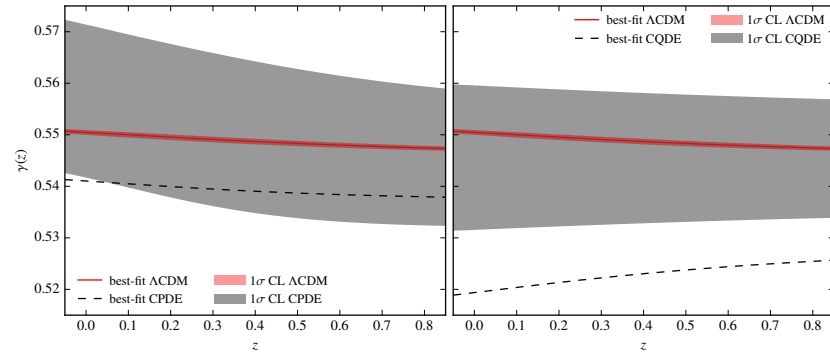


Figure 5.8: Comparisons of best-fit and $1\sigma$-range $\gamma(z)$ between CPDE and $\Lambda$CDM (left panel) and between CQDE and $\Lambda$CDM (right panel).

Table 5.4: Centralized $1\sigma$ CL intervals of the free parameters in $\Lambda$CDM and interacting models for the linear error propagation.

| Parameter | $\Lambda$CDM | CPDE | CQDE |
|---|---|---|---|
| $\zeta \pm \Delta\zeta$ | 0.0 | $0.0067 \pm 0.0033$ | $-0.0034 \pm 0.0034$ |
| $\sigma_{8,0} \pm \Delta\sigma_{8,0}$ | $0.7209 \pm 0.0426$ | $0.6412 \pm 0.0383$ | $0.7845 \pm 0.0930$ |
| $\Omega_{\mathrm{DE},0} \pm \Delta\Omega_{\mathrm{DE},0}$ | $0.6846 \pm 0.0649$ | $0.6900 \pm 0.0692$ | $0.7013 \pm 0.0686$ |
| $w_0 \pm \Delta w_0$ | $-1.0$ | $-1.5521 \pm 0.5521$ | $-0.7776 \pm 0.2224$ |

the task by centralizing the $1\sigma$ CL intervals, getting the values listed in table 5.4, then propagate the errors through eqs. (5.16), (5.1), (5.26) and (5.29).

Although the CQDE's best-fit is closer to $\Lambda$CDM than CPDE's best-fit, CQDE presents a wider $1\sigma$ range, encompassing the entire $\Lambda$CDM $1\sigma$ range (see figure 5.6). CPDE's $1\sigma$ range is about as wide as $\Lambda$CDM's. The three models are overall consistent within $1\sigma$ CL.

In figure 5.7 we analyze the unmodified $f(z)$ and $\sigma_8(z)$ separately. Faster growth rate means less dark matter in the past and explains the corresponding lower amplitudes $\sigma_8$ for CPDE, which presents higher $f(z)$ compared to $\Lambda$CDM. The opposite happens in CQDE. The differences between the interacting models and $\Lambda$CDM appear to enhance as $z$ increases. The interacting models' $1\sigma$ ranges are consistent with $\Lambda$CDM except for CPDE's $1\sigma$-range $\sigma_8$, which is only marginally consistent with $\Lambda$CDM at low redshifts.

The $1\sigma$ range interval of $\gamma(z)$ in $\Lambda$CDM (see figure 5.8) is very tight because the only uncertainty involved is in the $\Omega_{\mathrm{DE},0}$ parameter, which is well constrained. The best-fit growth index is lower than $\Lambda$CDM's best-fit in the two CDE models, falling closer to $\Lambda$CDM in the CPDE case and outside its own $1\sigma$ range in the CQDE case. However, their $1\sigma$ ranges are still consistent with $\Lambda$CDM in the redshift interval we are considering.

# Chapter 6

# A tentative detection with non-virialized galaxy clusters

Cosmological simulations in a $\Lambda$CDM universe and observations of galaxy and gas distributions suggest that clusters of galaxies are still accreting mass and thus are not expected to have achieved equilibrium. In this chapter we investigate the possibility to evaluate the departure from virial equilibrium in order to detect effects from a DE-DM interaction in that balance. The Layzer–Irvine model, a simple model for the interacting sector, has been considered previously [106–111]. We now employ optical observations in order to get mass profiles and intracluster gas temperatures of a set of galaxy clusters through weak lensing and X-ray data. We then perform evaluations of observed virial ratios, interaction strength, rest virial ratio and departure from equilibrium factors with a Monte Carlo method for error estimation. This work resulted in a paper published in the Monthly Notices of the Royal Astronomical Society [7].

## 6.1   The Layzer–Irvine model with interaction

Also known as the cosmic energy equation, the Layzer–Irvine equation [52, 112] generalizes the energy conservation equation of a system of non-relativistic particles interacting gravitationally in an expanding cosmological background. Here we include the dark energy–dark matter interaction in this balance. The interaction is described by a phenomenological model similar to that of section 5.2, with interaction proportional to the DM density. In an FLRW background,

$$\dot{\rho}_{\mathrm{DM}} + 3H\rho_{\mathrm{DM}} = 3H\zeta\rho_{\mathrm{DM}}, \tag{6.1a}$$

$$\dot{\rho}_{\mathrm{DE}} + 3H\rho_{\mathrm{DE}}(1 + w_{\mathrm{DE}}) = -3H\zeta\rho_{\mathrm{DM}}. \tag{6.1b}$$

Eq. (6.1a) is the same as eq. (5.31) but in terms of the cosmic time. We abandon the notation that used bars to indicate unperturbed quantities since we are not using perturbation theory in this chapter. Denoting the kinetic and the potential energy densities of the dark matter component by $\rho_{kin}$ and $\rho_{pot}$, with $\rho_{kin} + \rho_{pot} = \rho_{DM}$, the resulting Layzer–Irvine equation for dark matter [111] reads

$$\dot{\rho}_{DM} + H[(2 + 3\zeta)\rho_{kin} + (1 + 3\zeta)\rho_{pot}] = 0. \tag{6.2}$$

The time derivative vanishes when in equilibrium, yielding the interacting virial balance as

$$\frac{\rho_{kin}}{\rho_{pot}} = -\frac{1 + 3\zeta}{2 + 3\zeta}. \tag{6.3}$$

However, we want to take into account departures from equilibrium. Note that certainty of convergence of the energy density towards equilibrium, together with other magnitude restriction considerations [e.g. 48], prescribes from eq. (6.2) to exclude values of $\zeta$ lower than $-1/3$.

### 6.1.1 The non-virialized model

In order to simplify the calculation, we approximate the departure of $\rho_{kin}$ from the equilibrium as proportional to the departure of $\rho_{pot}$. That is, from eq. (6.3),

$$\dot{\rho}_{kin} \approx -\frac{1 + 3\zeta}{2 + 3\zeta}\dot{\rho}_{pot}, \tag{6.4}$$

so that eq. (6.2) becomes

$$\left[1 - \frac{1+3\zeta}{2+3\zeta}\right]\dot{\rho}_{pot} = -H[(2 + 3\zeta)\rho_{kin} + (1 + 3\zeta)\rho_{pot}], \tag{6.5}$$

then the virial ratio is given by

$$\frac{\rho_{kin}}{\rho_{pot}} = -\frac{1 + 3\zeta}{2 + 3\zeta} - \frac{1}{(2 + 3\zeta)^2}\frac{\dot{\rho}_{pot}}{H\rho_{pot}}. \tag{6.6}$$

The virial balance eq. (6.3) is corrected by a term we call departure from equilibrium (DfE). For the approximation eq. (6.4) to remain valid, the DM halo has to be close to the virial equilibrium. We thus need to check that

$$\left|\frac{\dot{\rho}_{pot}}{H\rho_{pot}}\right| \ll (2 + 3\zeta)(1 + 3\zeta). \tag{6.7}$$

A simple solution for $\zeta$ can be obtained in that case as long as $\rho_{\text{kin}}$, $\rho_{\text{pot}}$, $\dot{\rho}_{\text{pot}}$ and $H$ can be observed. Dividing eq. (6.5) by $H\rho_{\text{pot}}$, we get

$$\left[1 - \frac{1 + 3\zeta}{2 + 3\zeta}\right]\frac{\dot{\rho}_{\text{pot}}}{H\rho_{\text{pot}}} = -(2 + 3\zeta)\frac{\rho_{\text{kin}}}{\rho_{\text{pot}}} - (1 + 3\zeta);\qquad(6.8)$$

then, in terms of the theoretical virial ratio $\rho_{\text{kin}}/\rho_{\text{pot}}$ and the term $\dot{\rho}_{\text{pot}}/H\rho_{\text{pot}}$, we have the quadratic equation

$$9\zeta^2\left(1 + \tfrac{\rho_{\text{kin}}}{\rho_{\text{pot}}}\right) + 3\zeta\left(4\tfrac{\rho_{\text{kin}}}{\rho_{\text{pot}}} + 3\right) + \left(4\tfrac{\rho_{\text{kin}}}{\rho_{\text{pot}}} + 2 + \tfrac{\dot{\rho}_{\text{pot}}}{H\rho_{\text{pot}}}\right) = 0\qquad(6.9)$$

with the solution

$$\zeta = \frac{-\left(3 + 4\tfrac{\rho_{\text{kin}}}{\rho_{\text{pot}}}\right) + \sqrt{1 - 4\tfrac{\dot{\rho}_{\text{pot}}}{H\rho_{\text{pot}}}\left(1 + \tfrac{\rho_{\text{kin}}}{\rho_{\text{pot}}}\right)}}{6\left(1 + \tfrac{\rho_{\text{kin}}}{\rho_{\text{pot}}}\right)}\qquad(6.10)$$

verifying the classical, non-interacting and virialized result $\zeta = 0$ for $\dot{\rho}_{\text{pot}} = 0$ and $\rho_{\text{kin}}/\rho_{\text{pot}} = -1/2$. Note that eq. (6.10) is singular at $\rho_{\text{kin}}/\rho_{\text{pot}} = -1$. This singularity has its origin in the approximation eq. (6.4) and corresponds to $\zeta \to -\infty$.

We now need to evaluate $\rho_K$, $\rho_W$, $\dot{\rho}_W$ and $H$ from cluster observations. However, as we will see in section 6.2.3, the factor $\dot{\rho}_{\text{pot}}/H\rho_{\text{pot}}$ in the DfE is not a pure observable and depends on $\zeta$.

## 6.2    The evaluation from clusters

For each cluster, we have access to the total mass distribution through weak-lensing observations and to the cluster's kinetic state. The former is given through Navarro–Frenk–White (NFW) profile parameter fits, from which we can derive the potential energy, and the latter is evaluated through the cluster's X-ray temperature. In the following we provide the framework to make contact between such observables and the theoretical scheme we have presented above.

### 6.2.1    The NFW density profile and weak-lensing mass

The NFW density profile [113] found in *N*-body simulations is widely used to fit observed clusters in order to parametrize their mass distribution. The profile has two parameters and can be expressed in different ways, being the classical form in terms of a scale radius $r_{\text{s}}$ and the corresponding density $\rho_{\text{s}}$:

$$\rho_{\text{NFW}}(r) = \frac{\rho_{\text{s}}}{\frac{r}{r_{\text{s}}}\left(1 + \frac{r}{r_{\text{s}}}\right)^2}.\qquad(6.11)$$

From spherical collapse considerations, an "edge" can be defined at the virial radius of a cluster, assumed to extend to a distance $r_{200}$ within which the mean density is about 200 times the background density. This suggests defining the NFW concentration parameter $c \equiv r_{200}/r_{\rm s}$. Integrating the profile yields the mass profile

$$M_{\rm NFW}(r) = \frac{M_{200}}{\ln(1+c) - \frac{c}{1+c}} \left[ \ln\left(1 + c\frac{r}{r_{200}}\right) - \frac{c\frac{r}{r_{200}}}{1 + c\frac{r}{r_{200}}} \right], \qquad (6.12)$$

where $M_{200}$ is the mass inside $r_{200}$. The density profile in terms of $c$, $r_{200}$ and $M_{200}$ reads

$$\rho_{\rm NFW}(r) = \frac{M_{200}}{4\pi(r_{200})^3 \left[\ln(1+c) - \frac{c}{1+c}\right] \frac{r}{r_{200}}\left(1 + c\frac{r}{r_{200}}\right)^2}. \qquad (6.13)$$

## 6.2.2   The potential and kinetic energy density evaluations

With the profile (6.13), the potential energy density is simply

$$\rho_{\rm pot} \equiv -\frac{4\pi}{\frac{4}{3}\pi(r_{200})^3} \int_0^{r_{200}} \frac{\rho(r)GM(r)}{r} r^2 \, {\rm d}r = -\frac{3G(M_{200})^2}{4\pi(r_{200})^4 f_c}, \qquad (6.14)$$

with

$$f_c \equiv \frac{(1+c)\left[\ln(1+c) - c(1+c)^{-1}\right]^2}{c\left\{\frac{1}{2}\left[(1+c) - (1+c)^{-1}\right] - \ln(1+c)\right\}}. \qquad (6.15)$$

On the other hand, in order to evaluate the kinetic state of the cluster we use published X-ray observations, where we just need to obtain the X-ray temperature to get the equipartition formula

$$\rho_{\rm kin} = \frac{3}{2}N\frac{k_{\rm B}T_{\rm X}}{V} = \frac{9}{8\pi}\frac{M_{200}}{r_{200}^3}\frac{k_{\rm B}T_{\rm X}}{\mu m_{\rm H}}, \qquad (6.16)$$

where the equivalent number of particles $N$ is computed from the total mass given by weak-lensing as $M_{200}/\mu m_{\rm H}$, $\mu$ is the mean molecular mass in the intracluster gas, $m_{\rm H}$ is the proton mass, $V$ is the volume and $T_{\rm X}$ is the observable X-ray temperature. An advantage of this method over using a scale relation $\sigma_{\rm X}$-$T_{\rm X}$ between the galaxy velocity dispersion and the X-ray temperature, as in previous works [106–108]. is that the error from the scatter is avoided. We use a single compounded temperature $T_{\rm X}$ extracted from the X-ray flux of the central region of radius $r_{500}$, i.e., the radius within which the density is 500 times the background

density, which implies $r_{500} < r_{200}$. This is justified since this temperature already largely encompasses the turnaround of the temperature profile [114–116], therefore representing well the total density averaged temperature (the so-called virial temperature).

At this point the virial ratio can be evaluated, combining eqs. (6.14) and (6.16), as

$$\frac{\rho_{\text{kin}}}{\rho_{\text{pot}}} = -\frac{3}{2} \frac{r_{200}}{GM_{200}} \frac{k_B T_X}{\mu m_H} f_c. \tag{6.17}$$

## 6.2.3   The departure from equilibrium evaluation

The DfE factor can be rewritten as

$$-\frac{1}{(2 + 3\zeta)^2} \frac{\dot{\rho}_{\text{pot}}}{H\rho_{\text{pot}}} = -\frac{1}{(2 + 3\zeta)^2} \frac{\rho'_{\text{pot}}}{H\rho_{\text{pot}}} \dot{r}_{200}, \tag{6.18}$$

with the prime indicating differentiation with respect to $r_{200}$. From eq. (6.14) we get

$$\frac{\rho'_{\text{pot}}}{\rho_{\text{pot}}} = \frac{cg_c - 3}{r_{200}}, \quad \text{with} \quad g_c \equiv \frac{\ln(1 + c) - c\,(1 + c)^{-1}}{\frac{1}{2}\,(c + 2) - (1 + c)\ln(1 + c)}. \tag{6.19}$$

$\dot{r}_{200}$ still remains to be evaluated. We write the kinetic density as

$$\rho_{\text{kin}} = \frac{3}{2} \frac{M_{200}}{V} \sigma_X^2, \tag{6.20}$$

in terms of a one-dimensional velocity dispersion $\sigma_X$, thus defined as $\sigma_X^2 = \frac{k_B T_X}{\mu m_H}$. Now we define a theoretical average velocity dispersion $v_{\text{th}}$ the cluster would have if it were at virial equilibrium, adiabatically evolving from the current state. The theoretical virial ratio is given by eq. (6.3), with a theoretical kinetic density

$$\rho_{\text{kin,th}} = \frac{3}{2} \frac{M_{200}}{V} (v_{\text{th}})^2. \tag{6.21}$$

This definition combined with eqs. (6.3) and (6.14) leads to

$$(v_{\text{th}})^2 = \frac{2}{3} \frac{1 + 3\zeta}{2 + 3\zeta} \frac{GM_{200}}{r_{200} f_c}. \tag{6.22}$$

Finally, we evaluate the time evolution of $r_{200}$ by taking its difference with the velocity dispersion

$$\dot{r}_{200} = \sigma_X - v_{\text{th}}. \tag{6.23}$$

65

We obtain the DfE factor

$$-\frac{\dot{\rho}_{\text{pot}}/H\rho_{\text{pot}}}{(2+3\zeta)^2} = -\frac{1}{(2+3\zeta)^2}\frac{cg_c-3}{Hr_{200}}\left[\left(\frac{k_{\text{B}}T_{\text{X}}}{\mu m_{\text{H}}}\right)^{1/2} - \left(\frac{2}{3}\frac{1+3\zeta}{2+3\zeta}\frac{GM_{200}}{r_{200}f_c}\right)^{1/2}\right]. \quad (6.24)$$

With this equation we estimate the DfE due to "standard" dynamical sources (e.g. cluster collisions, AGN and supernova feedback, dynamical friction) combining observations and the dark energy model, leaving no room for degeneracy in the determination of $\zeta$. The DfE presented here appears model dependent in its explicit reference to the interaction strength; however, the method can use any model we want that gives a definite shift to the virial balance.

## 6.3 Computations for a set of non-virialized clusters

Cosmologically interesting observations of clusters are produced in many surveys and studies such as Okabe et al. [117] and Planck Collaboration [118]. In order to maximize our sample, while being able to separately evaluate from observations the kinetic and potential energy states of each cluster, we have restricted inputs to weak-lensing NFW fit parameters, X-ray derived $c_{500}$ NFW fits, and X-ray temperatures.

### 6.3.1 The sample

In order to try to minimize any systematics due to observational uncertainties, the clusters in our sample should present well determined X-ray gas temperature, as well as NFW profile fitted to the mass distribution obtained with weak lensing observations.

Most of the 22 clusters in our sample come from Okabe et al. [117]. Their NFW profiles are described by best-fit virial masses $M_{\text{vir}}$, concentration parameters $c_{\text{vir}}$ and masses $M_{200}$ estimated from this three-dimensional model fitting. Those are the Abell clusters A68, A115, A209, A267, A383, A521, A586, A611, A697, A1835, A2219, A2261, A2390, A2631 and also RX J1720.1+2638, RX J2129.6+0005, ZwCl 1454.8+2233 and ZwCl 1459.4+4240. Their weak lensing data are shown in table 6.1. We also include four more clusters from Planck Collaboration [118]: A520, A963, A1914 and A2034 (data in table 6.2). Weak lensing masses $M_{500}$ and best fitting NFW concentration parameter $c_{500}$ are given instead of $M_{\text{vir}}$, $c_{\text{vir}}$ and $M_{200}$ for these clusters. However, the error bars for $c_{500}$ were estimated from the X-ray data, since they are not given by ref. [118]. The spectroscopically determined temperatures $T_{\text{X}}$ are measured within $r_{500}$ and are all given in ref. [118], with the exceptions of A115 and A697 from Landry et al.

Table 6.1: Weak lensing masses $M_{200}$, $M_{\mathrm{vir}}$ and concentration $c_{\mathrm{vir}}$ for the Okabe's clusters. Masses are in units of $h^{-1}10^{14}M_{\odot}$.

| Cluster | $M_{200}$ | $M_{\mathrm{vir}}$ | $c_{\mathrm{vir}}$ |
|---|---|---|---|
| A68 | $4.45^{+1.75}_{-1.35}$ | $5.49^{+2.56}_{-1.81}$ | $4.02^{+3.36}_{-1.82}$ |
| A115 | $4.24^{+2.60}_{-1.79}$ | $5.36^{+4.08}_{-2.45}$ | $3.69^{+5.03}_{-2.04}$ |
| A209 | $10.62^{+2.17}_{-1.81}$ | $14.00^{+3.31}_{-2.60}$ | $2.71^{+0.69}_{-0.60}$ |
| A267 | $3.23^{+0.82}_{-0.69}$ | $3.85^{+1.08}_{-0.88}$ | $6.00^{+2.11}_{-1.58}$ |
| A383 | $3.11^{+0.88}_{-0.69}$ | $3.62^{+1.15}_{-0.86}$ | $8.87^{+5.22}_{-3.05}$ |
| A521 | $4.58^{+1.00}_{-0.88}$ | $5.85^{+1.45}_{-1.22}$ | $3.06^{+1.01}_{-0.79}$ |
| A586 | $6.29^{+2.26}_{-1.69}$ | $7.37^{+2.89}_{-2.08}$ | $8.38^{+3.52}_{-2.52}$ |
| A611 | $5.47^{+1.31}_{-1.11}$ | $6.65^{+1.75}_{-1.42}$ | $4.23^{+1.77}_{-1.23}$ |
| A697 | $9.73^{+1.86}_{-1.61}$ | $12.36^{+2.68}_{-2.21}$ | $2.97^{+0.85}_{-0.69}$ |
| A1835 | $10.86^{+2.53}_{-2.08}$ | $13.69^{+3.65}_{-2.86}$ | $3.35^{+0.99}_{-0.79}$ |
| A2219 | $7.75^{+1.89}_{-1.60}$ | $9.11^{+2.54}_{-2.06}$ | $6.88^{+3.42}_{-2.16}$ |
| A2261 | $7.97^{+1.51}_{-1.31}$ | $9.49^{+2.01}_{-1.69}$ | $6.04^{+1.71}_{-1.31}$ |
| A2390 | $6.92^{+1.50}_{-1.29}$ | $8.20^{+1.93}_{-1.63}$ | $6.20^{+1.53}_{-1.28}$ |
| A2631 | $4.54^{+0.89}_{-0.78}$ | $5.24^{+1.15}_{-0.98}$ | $7.84^{+3.54}_{-2.28}$ |
| RX J1720 | $3.48^{+1.28}_{-0.99}$ | $4.07^{+1.65}_{-1.22}$ | $8.73^{+5.60}_{-3.08}$ |
| RX J2129 | $5.29^{+1.76}_{-1.38}$ | $6.71^{+2.73}_{-1.96}$ | $3.32^{+2.16}_{-1.34}$ |
| ZwCl 1454 | $2.80^{+1.39}_{-1.03}$ | $3.45^{+2.02}_{-1.36}$ | $4.01^{+3.44}_{-1.96}$ |
| ZwCl 1459 | $3.77^{+1.17}_{-0.98}$ | $4.40^{+1.50}_{-1.20}$ | $6.55^{+3.34}_{-2.18}$ |

Table 6.2: Weak lensing masses $M_{500}$ and concentration $c_{500}$ for the Planck Collaboration's clusters. Masses are in units of $10^{14}M_{\odot}$. Data from Planck Collaboration [118].

| Cluster | $M_{500}$ | $c_{500}$ |
|---|---|---|
| A520 | $4.1^{+1.1}_{-1.2}$ | $1.4 \pm 0.6$ |
| A963 | $4.2^{+0.9}_{-0.7}$ | $1.2 \pm 0.2$ |
| A1914 | $4.7^{+1.6}_{-1.9}$ | $2.0 \pm 0.2$ |
| A2034 | $5.1^{+2.1}_{-2.4}$ | $1.8 \pm 0.3$ |

[119] and A611 from Cavagnolo, Donahue, Voit & Sun [120]. Uncertainties correspond to $1\sigma$ CL. Errors in redshifts (see table 6.3) are not specified but can be safely neglected compared to the errors in other quantities (the typical spectroscopic redshift error is around 1 %).

**The uniformization of the NFW profiles**

It would be interesting if we had all clusters described by the same parameters, in a uniform way, so we can apply the same method for all of them, in a single code. In what follows we describe how we proceed to convert the NFW profile parameters for those clusters with given $M_{500}$ and $c_{500}$ to $M_{200}$ and $c$.

In general, within a radius $r_\Delta$ we have

$$\Delta = \frac{M_\Delta}{\frac{4}{3}\pi(r_\Delta)^3\bar{\rho}(z)}, \tag{6.25}$$

which results in the radius

$$r_\Delta = \frac{1}{H(z)}\sqrt[3]{\frac{2GM_\Delta H(z)}{\Delta}} \tag{6.26}$$

given the mass $M_\Delta$. For the latter set of clusters, with NFW profiles specified by $M_{500}$ and $c_{500} = r_{500}/r_s$ (rather than $c_{200}$, which we called just $c$), the parameter $r_s = r_{200}/c = r_{500}/c_{500}$ comes immediately by using eq. (6.26) for $\Delta = 500$. Using SymPy [121] in python, we get $M_{200}$ and $r_{200}$ by solving simultaneously an equation similar to eq. (6.12)—but parametrized by $M_{500}$ and $c_{500}$ and evaluated at $r_{200}$ to give $M_{200}$—and eq. (6.26) with $\Delta = 200$:

$$M_{200} = \frac{M_{500}}{\ln(1 + c_{500}) - \frac{c_{500}}{1+c_{500}}}\left[\ln\left(1 + c_{500}\frac{r_{200}}{r_{500}}\right) - \frac{c_{500}\frac{r_{200}}{r_{500}}}{1 + c_{500}\frac{r_{200}}{r_{500}}}\right], \tag{6.27a}$$

$$r_{200} = \frac{1}{H(z)}\sqrt[3]{\frac{GM_{200}H(z)}{100}}. \tag{6.27b}$$

Then we can finally compute $c = r_{200}/r_s$.

For the former set, with NFW profiles specified by $M_{200}$, $M_{\text{vir}}$ and $c_{\text{vir}}$, "vir" would correspond to some $\Delta_{\text{vir}}$ around 200 but this value can vary with the redshift. Then we proceed as follows. We compute $r_{200}$ with eq. (6.26) and solve

$$M_{200} = \frac{M_{\text{vir}}}{\ln(1 + c_{\text{vir}}) - \frac{c_{\text{vir}}}{1+c_{\text{vir}}}}\left[\ln\left(1 + c_{\text{vir}}\frac{r_{200}}{r_{\text{vir}}}\right) - \frac{c_{\text{vir}}\frac{r_{200}}{r_{\text{vir}}}}{1 + c_{\text{vir}}\frac{r_{200}}{r_{\text{vir}}}}\right] \tag{6.28}$$

for $r_{\text{vir}}$. $\Delta_{\text{vir}}$ can also be determined now with $r_{\text{vir}}$ and $M_{\text{vir}}$, inverting eq. (6.26). Finally, we have $r_s = r_{\text{vir}}/c_{\text{vir}}$ and $c = r_{200}/r_s$. The errors are estimated using a Monte Carlo method that we describe in the next section. With $c$ and $M_{200}$, we can now proceed to the computation of the virial ratios.

## 6.3.2 The Monte Carlo estimation of errors

We apply a Monte Carlo method to propagate uncertainties through the numerical solutions. Multiple random realizations of each cluster are performed, with the observables assuming values drawn from a distribution that reflects the $1\sigma$ confidence intervals from the original asymmetrical uncertainties. Then, we carry the computations for all realizations of each cluster and analyze the final distribution of the quantities of interest in order to get their error intervals.

**Uncertainties in $M_{200}$ and $c_{200}$**

These two NFW parameters are always positive. In order to guarantee that their uncertainties will not lead to negative values in any of the random realizations, we choose the log-logistic distribution, for it being a non-negative probability distribution whose probability density function (PDF) and cumulative distribution function (CDF) have simple analytical forms. If $X$ is a random variable following a log-logistic distribution, its PDF with parameters $(\alpha, \beta)$ is

$$f_X(x; \alpha, \beta) = \frac{(\beta/\alpha)\,(x/\alpha)^{\beta-1}}{\left[1 + (x/\alpha)^\beta\right]^2} \tag{6.29}$$

and the CDF is given by

$$F_X(x; \alpha, \beta) = \frac{1}{1 + (x/\alpha)^{-\beta}}. \tag{6.30}$$

For a given observable $X$ with measured value $x^{+\Delta x_1}_{-\Delta x_2}$, we would like the Monte Carlo generating distribution to match the following criteria:

(i) The maximum probability coincides with the nominal measure;

(ii) The probability of $X$ lying between $x - \Delta x_2$ and $x + \Delta x_1$ is 68 %;

(iii) The PDF has the same value at the two points $x - \Delta x_2$ and $x + \Delta x_1$, so the interval in condition (ii) corresponds to the 68 % most probable values, i.e., $1\sigma$ CL

For the log-logistic distribution, these conditions are translated as

(i) $\alpha \left(\frac{\beta-1}{\beta+1}\right)^{1/\beta} = x$ (for $\beta > 1$);

(ii) $F_X(x + \Delta x_1; \alpha, \beta) - F_X(x - \Delta x_2; \alpha, \beta) = 0.68$;

(iii) $f_X(x - \Delta x_2; \alpha, \beta) = f_X(x + \Delta x_1; \alpha, \beta)$.

69

However, these are too many conditions for a distribution which has only two parameters. We choose to relax condition (i) and solve (ii) and (iii) for $\alpha$ and $\beta$. In practice, our resulting maximum probabilities usually happen to lie very close to $x$.

When extracting the $1\sigma$ CL, we take the opposite direction and get a best-fit log-logistic PDF for the distributions of $M_{200}$ and $c$, now solving (ii) and (iii) for $x - \Delta x_2$ and $x + \Delta x_1$. The maximum probability of the distribution is assigned to the nominal value $x$.

We have also used the log-normal distribution to check whether our choice of distribution could be biasing our results. The log-normal PDF and CDF are given by

$$
f_X(x; \mu, \sigma) = \frac{\exp\left\{-\frac{(\ln x - \mu)^2}{2\sigma^2}\right\}}{x\sigma\sqrt{2\pi}}, \quad F_X(x; \mu, \sigma) = \frac{1}{2}\operatorname{erfc}\left[-\frac{\ln x - \mu}{\sigma\sqrt{2}}\right], \quad (6.31)
$$

where $\operatorname{erfc}(x)$ is the complementary error function and $\mu$ and $\sigma$ are the Gaussian parameters of the distribution of $\ln X$.

We applied this Monte Carlo procedure for the clusters in our sample. However, the log-normal distribution could not satisfy our requirements (ii) and (iii) for all clusters in the first group. Nevertheless, we were able to verify in the other cases, where the log-normal distribution works, that the confidence intervals obtained with the two distributions are very similar, within a few percent of displacement between their extremities. The maximum probability can vary a little more between the two distributions because (i) is not being satisfied, but we are more concerned with the confidence intervals, since we use uniform distributions for $c$, $M_{200}$ and $T_X$ in the evaluation of the virial ratios, interaction strength and departure from equilibrium. We believe, then, that the use of the log-logistic distribution with the requirements that we propose for the estimation of errors for $M_{200}$ and $c$ is a reasonable choice, as it works for all clusters and the results seem not to be biased.

**Virial ratios and interaction strength fittings**

Table 6.3 summarizes the data used for computation of the virial ratios and interaction strengths according to the steps described in section 6.2. We assume flat distributions within the range $[x - \Delta x_2, x + \Delta x_1]$ for the inputs in the form $x_{-\Delta x_2}^{+\Delta x_1}$ in the generation of random realizations for our Monte Carlo method.

Inspection of the final distributions of virial ratios and interaction strengths suggests the use of log-normal distributions to fit (the negative of) the data. However, due to the nature of these quantities and their domains, we include a location

Table 6.3: Redshift, temperature and compiled NFW parameters of the 22 galaxy clusters. Temperatures are given in keV and masses in units of $h^{-1}10^{14}M_\odot$. X-ray data from Planck Collaboration [118], Landry et al. [119], and Cavagnolo, Donahue, Voit & Sun [120].

| Cluster | $z$ | $k_\mathrm{B}T_\mathrm{X}$ | $M_{200}$ | $c$ |
|---|---|---|---|---|
| A68 | 0.255 | $8.3 \pm 0.3$ | $4.45^{+1.75}_{-1.35}$ | $2.49^{+3.12}_{-1.65}$ |
| A115 | 0.197 | $8.9^{+0.6}_{-0.7}$ | $4.24^{+2.60}_{-1.79}$ | $1.86^{+3.52}_{-1.48}$ |
| A209 | 0.206 | $6.6 \pm 0.2$ | $10.62^{+2.17}_{-1.81}$ | $1.90^{+0.81}_{-0.63}$ |
| A267 | 0.230 | $5.6 \pm 0.1$ | $3.23^{+0.82}_{-0.69}$ | $3.95^{+3.00}_{-1.96}$ |
| A383 | 0.188 | $4.1 \pm 0.1$ | $3.11^{+0.88}_{-0.69}$ | $5.59^{+6.31}_{-3.51}$ |
| A520 | 0.203 | $7.9 \pm 0.2$ | $4.20^{+2.30}_{-1.70}$ | $2.20^{+1.10}_{-0.80}$ |
| A521 | 0.248 | $6.1 \pm 0.1$ | $4.58^{+1.00}_{-0.88}$ | $2.18^{+1.13}_{-0.83}$ |
| A586 | 0.171 | $7.8^{+1.0}_{-0.8}$ | $6.29^{+2.26}_{-1.69}$ | $4.90^{+5.82}_{-3.16}$ |
| A611 | 0.288 | $7.1^{+0.6}_{-0.5}$ | $5.47^{+1.31}_{-1.11}$ | $3.01^{+1.99}_{-1.37}$ |
| A697 | 0.282 | $8.8^{+0.7}_{-0.6}$ | $9.73^{+1.86}_{-1.61}$ | $2.17^{+0.94}_{-0.73}$ |
| A963 | 0.206 | $5.6 \pm 0.1$ | $5.10^{+1.70}_{-1.40}$ | $2.10 \pm 0.40$ |
| A1835 | 0.253 | $8.4 \pm 0.1$ | $10.86^{+2.53}_{-2.08}$ | $2.35^{+1.27}_{-0.93}$ |
| A1914 | 0.171 | $8.5 \pm 0.2$ | $4.20^{+2.90}_{-2.00}$ | $3.20^{+0.70}_{-0.60}$ |
| A2034 | 0.113 | $6.4 \pm 0.2$ | $4.30^{+4.00}_{-2.40}$ | $2.90^{+0.90}_{-0.70}$ |
| A2219 | 0.228 | $9.6^{+0.3}_{-0.2}$ | $7.75^{+1.89}_{-1.60}$ | $4.59^{+4.11}_{-2.53}$ |
| A2261 | 0.224 | $6.1^{+0.6}_{-0.5}$ | $7.97^{+1.51}_{-1.31}$ | $4.31^{+2.37}_{-1.72}$ |
| A2390 | 0.231 | $9.1 \pm 0.2$ | $6.92^{+1.50}_{-1.29}$ | $4.40^{+2.63}_{-1.86}$ |
| A2631 | 0.278 | $7.5^{+0.4}_{-0.2}$ | $4.54^{+0.89}_{-0.78}$ | $5.57^{+4.24}_{-2.78}$ |
| RX J1720 | 0.164 | $5.9 \pm 0.1$ | $3.48^{+1.28}_{-0.99}$ | $4.87^{+6.98}_{-3.45}$ |
| RX J2129 | 0.235 | $5.6 \pm 0.1$ | $5.29^{+1.76}_{-1.38}$ | $4.67^{+6.21}_{-3.19}$ |
| ZwCl 1454 | 0.258 | $4.6 \pm 0.1$ | $2.80^{+1.39}_{-1.03}$ | $2.18^{+3.25}_{-1.57}$ |
| ZwCl 1459 | 0.290 | $6.4 \pm 0.2$ | $3.77^{+1.17}_{-0.98}$ | $4.10^{+4.56}_{-2.56}$ |

parameter to allow the distribution to be shifted from the origin. The log-normal PDF is then

$$f_X(x;\mu,\sigma,x_\mathrm{loc}) = \frac{\exp\left\{-\left[\ln(x - x_\mathrm{loc}) - \mu\right]^2/2\sigma^2\right\}}{(x - x_\mathrm{loc})\,\sigma\,\sqrt{2\pi}} \qquad (6.32)$$

with $x_{\text{loc}}$ being the location parameter. We take the 68% most probable values and the maximum probability of this log-normal PDF to yield the resulting value $x^{+\Delta x_1}_{-\Delta x_2}$ of the quantity $X$. The fits obtained are especially good for the interaction strengths, as we show in section 6.4.2.

In addition, we introduce two selection criteria which we apply to the values of the interaction strength obtained with this method to conserve realizations: one physical, discussed in section 6.1, selects $\zeta \geq -1/3$, while the other avoids numerical problems, discussed in section 6.1.1, by keeping only $9\zeta \leq 200$ (see discussion in section 6.4.2).

**Reliability of the results**

Our analysis considers samples of 8600 random realizations of each cluster. However, some of them happen to have no solution for $\zeta$, or to have a solution outside the domain established by eq. (6.2). We remove these cases from the analysis, which makes the samples considerably smaller for some clusters. That is the case for A68, A115, A520 and A1914, for which we are left with only about 650 (on average) realizations. A possible explanation for such a large fraction of these samples not having a physical solution for $\zeta$ could be linked with the dynamical activity of those clusters [e.g. 122, 123], so their virial states are not as close to equilibrium for our method to be applicable.

The gas distribution in clusters can be used as a probe of the recent past dynamical activity of a cluster, since the gas responds quickly to perturbations in the gravitational potential, for instance, due to cluster merger and/or collision [124]. Visual inspections of Chandra X-ray images show that all clusters except A115, A520 and A1914 have rather undisturbed and symmetric gas distribution, suggesting that they are not dynamically active.

For comparison purposes, we define a "success rate" (SR) as the fraction of realizations satisfying our selection criteria in the total generated for each cluster. Clusters like A1835, A209 and A2261 present this fraction very close or equal to 1. The success rates for all clusters are presented in table 6.4. In the histograms, we use a number of bins proportional to the size of the samples.

In order to evaluate the consistency of our method, we consider a cluster from $N$-body simulation, similar to those of Machado & Lima Neto [125], in a cosmology with $\Omega_{\text{M}} = 0.3$, $\Omega_{\text{DE}} = 0.7$, $h = 0.72$ and no interaction in the dark sector, so the virial ratio should be very close[1] to $-0.5$ and interaction compatible with zero. The data for this simulated cluster are $M_{200} = 18.0\,h^{-1}10^{14}M_{\odot}$, $z = 0.0$, $c = 3.0$ and $T_{\text{X}} = 7.3 \pm 0.8\,\text{keV}$. The uncertainty in the temperature comes from

---

[1]Some variations can be introduced by the effects of projection translating from simulation to observables.

Table 6.4: Fraction of Monte Carlo-produced realisations for each cluster. The SR here presented were computed for our Monte Carlo samples of size 8600. Tests have shown that there is no significant variation of the SR with the size of the sample.

| Cluster | A115 | A1835 | A1914 | A2034 | A209 | A2219 |
|---------|------|-------|-------|-------|------|-------|
| SR | 0.06 | 1.00 | 0.09 | 0.58 | 1.00 | 0.79 |

| Cluster | A2261 | A2390 | A2631 | A267 | A383 | A520 |
|---------|-------|-------|-------|------|------|------|
| SR | 1.00 | 0.75 | 0.68 | 0.61 | 1.00 | 0.05 |

| Cluster | A521 | A586 | A611 | A68 | A697 |
|---------|------|------|------|-----|------|
| SR | 0.67 | 0.86 | 0.80 | 0.11 | 0.99 |

| Cluster | A963 | RX J1720 | RX J2129 | ZwCl 1454 | ZwCl 1459 |
|---------|------|----------|----------|-----------|-----------|
| SR | 0.91 | 0.71 | 1.00 | 0.64 | 0.63 |

the $\sigma_X$–$T_X$ scatter relation [126]

$$\sigma_X = 10^{2.49\pm0.02} T_X^{0.65\pm0.03}, \qquad (6.33)$$

from which $T_X$ was computed for a one-dimensional velocity dispersion of $\sigma_X = 1125\,\mathrm{km\,s^{-1}}$. Because the observed virial ratio is linear with the temperature, the only source of errors in this case, its histogram for all random realizations produced in our code reflects clearly the uniform distribution assigned to the input temperature. Fitting that uniform distribution we find a virial ratio of $-0.47 \pm 0.04$ from the central 68 % most probable values.

With the analysis of section 6.3.2, for the interaction strength we get $9\zeta = 0.05^{+0.69}_{-0.54}$, therefore compatible with the simulation. The theoretical virial ratio is also in accordance with the classic value, $(\rho_{\mathrm{kin}}/\rho_{\mathrm{pot}})_{\mathrm{th}} = -0.51 \pm 0.05$, while the DfE being $-0.08 \pm 0.06$ satisfies our condition (6.7).

## 6.4 Analysis of the results

In this section we present and discuss the outcome of our analysis starting with the observed virial ratios (OVRs), the theoretical virial ratios (TVRs) estimates from combining their DfE factors and interaction strengths $\zeta$. Throughout this section, we present the constraints on the virial ratios, interaction and DfE in figures 6.1b, 6.2, 6.3 and 6.4, all obtained for each cluster according to the method described in the previous section. These results are summarized in table 6.5.

Table 6.5: Virial ratios, interactions, theoretical virial ratios and departure from equilibrium from the log-normal fits.

| Cluster | OVR | $\zeta$ | TVR | DfE |
|---|---|---|---|---|
| A520 | $-0.96 \pm 0.02$ | $-53.28^{+19.87}_{-44.20}$ | $-0.96 \pm 0.02$ | $-0.003 \pm 0.003$ |
| A1914 | $-0.95 \pm 0.02$ | $-48.60^{+18.59}_{-43.09}$ | $-0.96 \pm 0.02$ | $-0.004 \pm 0.003$ |
| A115 | $-0.94 \pm 0.03$ | $-35.72^{+17.85}_{-43.34}$ | $-0.95 \pm 0.03$ | $-0.01 \pm 0.01$ |
| A68 | $-0.93 \pm 0.03$ | $-31.62^{+13.90}_{-37.11}$ | $-0.94 \pm 0.03$ | $-0.01 \pm 0.01$ |
| A521 | $-0.89 \pm 0.05$ | $-13.14^{+5.67}_{-24.80}$ | $-0.90 \pm 0.05$ | $-0.01 \pm 0.03$ |
| A267 | $-0.88 \pm 0.06$ | $-10.50^{+5.45}_{-24.20}$ | $-0.89 \pm 0.06$ | $-0.01 \pm 0.04$ |
| A2390 | $-0.87 \pm 0.06$ | $-13.08^{+5.90}_{-22.60}$ | $-0.89 \pm 0.05$ | $-0.05 \pm 0.04$ |
| A2631 | $-0.87 \pm 0.07$ | $-11.56^{+5.75}_{-22.91}$ | $-0.89 \pm 0.06$ | $-0.04 \pm 0.05$ |
| A611 | $-0.85^{+0.07}_{-0.08}$ | $-8.76^{+4.58}_{-20.08}$ | $-0.87 \pm 0.07$ | $-0.03 \pm 0.05$ |
| ZwCl 1459 | $-0.85 \pm 0.08$ | $-7.41^{+4.43}_{-21.56}$ | $-0.86^{+0.07}_{-0.08}$ | $-0.02 \pm 0.06$ |
| A2219 | $-0.84 \pm 0.08$ | $-9.28^{+4.48}_{-18.55}$ | $-0.87 \pm 0.06$ | $-0.07 \pm 0.05$ |
| ZwCl 1454 | $-0.82 \pm 0.09$ | $-3.95^{+2.42}_{-15.49}$ | $-0.82^{+0.09}_{-0.10}$ | $0.02 \pm 0.06$ |
| RX J1720 | $-0.81 \pm 0.10$ | $-4.47^{+2.94}_{-16.34}$ | $-0.83 \pm 0.09$ | $-0.02 \pm 0.07$ |
| A697 | $-0.81 \pm 0.07$ | $-8.17^{+3.62}_{-10.75}$ | $-0.84 \pm 0.06$ | $-0.04 \pm 0.06$ |
| A963 | $-0.78^{+0.07}_{-0.10}$ | $-4.59^{+1.98}_{-13.39}$ | $-0.80^{+0.08}_{-0.09}$ | $-0.01 \pm 0.05$ |
| A2034 | $-0.77^{+0.08}_{-0.10}$ | $-4.37^{+2.23}_{-13.35}$ | $-0.80^{+0.08}_{-0.09}$ | $-0.02 \pm 0.06$ |
| A586 | $-0.77 \pm 0.11$ | $-3.83^{+2.74}_{-12.51}$ | $-0.80^{+0.09}_{-0.10}$ | $-0.07 \pm 0.08$ |
| A1835 | $-0.70^{+0.06}_{-0.07}$ | $-4.84^{+2.10}_{-3.78}$ | $-0.75 \pm 0.06$ | $-0.07 \pm 0.06$ |
| A383 | $-0.61^{+0.08}_{-0.11}$ | $-0.41^{+1.04}_{-3.44}$ | $-0.60^{+0.09}_{-0.12}$ | $0.05 \pm 0.10$ |
| A209 | $-0.60 \pm 0.05$ | $-1.92^{+1.01}_{-1.41}$ | $-0.64 \pm 0.05$ | $-0.05 \pm 0.08$ |
| RX J2129 | $-0.60^{+0.09}_{-0.12}$ | $-0.68^{+1.23}_{-4.04}$ | $-0.63^{+0.10}_{-0.12}$ | $-0.02 \pm 0.10$ |
| A2261 | $-0.56^{+0.06}_{-0.07}$ | $-0.99^{+1.00}_{-1.55}$ | $-0.60 \pm 0.07$ | $-0.03 \pm 0.09$ |
| TOTAL | — | $-1.99^{+2.56}_{-16.00}$ | $-0.79 \pm 0.13$ | — |
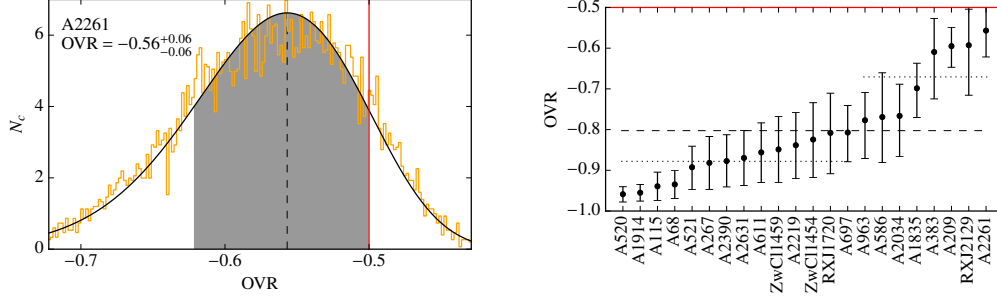
(a) OVR for the cluster A2261 from a sample of 8600 random realizations. $\rho_{kin}/\rho_{pot} = -0.56 \pm 0.06$.

(b) OVRs with error bars indicating 95 % and 68 % CLs for all clusters.

Figure 6.1: Panel (a) shows in detail the distribution of the OVR for the cluster A2261 when we apply the Monte Carlo method (section 6.3.2). $N_c$ is the normalized count of Monte Carlo clusters per bin of OVR. The shade area correspond to the 68 % CL. The dashed vertical line indicates the most probable value while the red solid line denotes the classic value. Panel (b) presents the most probable values and confidence levels for each cluster. The error bars give the 68 % CL. The mean of the most probable values is signaled by the dashed black line. The two dotted lines show the means for the two groups of clusters defined in the text and the solid red line marks the classic value.

## 6.4.1 The observed virial ratios

The OVR is obtained from applying the method described in section 6.3.2 to eq. (6.17). The histograms of OVR produced for each cluster are very similar to the ones obtained for their theoretical counterparts (section 6.4.3). As an example, we present in figure 6.1a the distribution obtained for the cluster A2261. It represents the histogram distribution of the OVR obtained from our Monte Carlo sampling of mass, temperature and concentration ranges. Superimposed is the log-normal fit, with shaded area corresponding to the 68 % CL. The red vertical line marks the theoretical non-interacting value, while the dashed line gives the most likely value.

We summarize the results of the OVR with their corresponding asymmetrical errors in figure 6.1b, where we have shown the theoretical non-interacting virial ratio as a horizontal red line. We have ordered the clusters by increasing OVR and keep this order for the rest of the work.

We have represented the mean value for the whole sample with a dashed line. We identify two groups of similar virial ratios separated by the global mean and for each group we represent their means by the dotted lines. The dispersion of the

ratios may reflect the diversity of the equilibrium conditions. However, the first group seems to have less scatter than the second one.

With this robust non-linear treatment of error propagation, all clusters exclude $-0.5$ at $1\sigma$, with the only exception of A2261, which includes that value marginally.

### 6.4.2 The interaction strength

As previously mentioned, we solve eq. (6.6) for $\zeta$ with the DfE term (6.24) using the Monte Carlo method of section 6.3.2. Eq. (6.10) is singular at $\rho_{\mathrm{kin}}/\rho_{\mathrm{pot}} = -1$, which corresponds to $\zeta$ infinite. This is a limitation of our method that we deal with by restricting the interaction strength to $|9\zeta| \leq 200$ such that the histograms would be legible. Note that this introduces a cut in the histograms of the TVRs (section 6.4.3), which reflects the limitation of our method.

Figure 6.2 represents the histograms of interaction strengths for all clusters, with the two lowest rightmost panels displaying the compounded distribution for all the studied clusters and the most probable values of $\zeta$ for all clusters together with their error bars for the 68 % CL. As previously done, the vertical dashed line gives the most probable value, and the shaded areas correspond to the 68 % CL. The red solid lines indicate the $\zeta = 0$ absence of interaction. The whole sample mean of the most probable values is given by the horizontal dashed line. Each group previously singled out also present their group mean as horizontal dotted lines. Finally, we add the most probable value and error bars of the compounded distribution in blue.

Of the 22 clusters, all of them except A586, A383, RX J2129 and A2261 (marginally) display a $1\sigma$ detection favoring positive $\zeta$.

In this model, the interaction strength should be the same for all clusters. The global mean $\bar{\zeta} = 1.44$ is compatible with 13 of the 22 clusters: A521, A267, A2390, A2631, A611, ZwCl 1459, A2219, ZwCl 1454, RX J1720, A697, A963, A586 and A2034. However, three of the clusters, as well as the compounded distribution that yields $\zeta = 0.288^{+2.252}_{-0.397}$, display compatibility with no interaction. This points to problems in our method, namely when it assumed small deviation from equilibrium while the results have important variations. Actually, the highest boundary is limited by the results of Salvatelli, Marchini, Lopez-Honorez & Mena [127] to[2] 0.30. Nevertheless, we concentrate on the present scheme and leave the solutions to a forthcoming work.

---

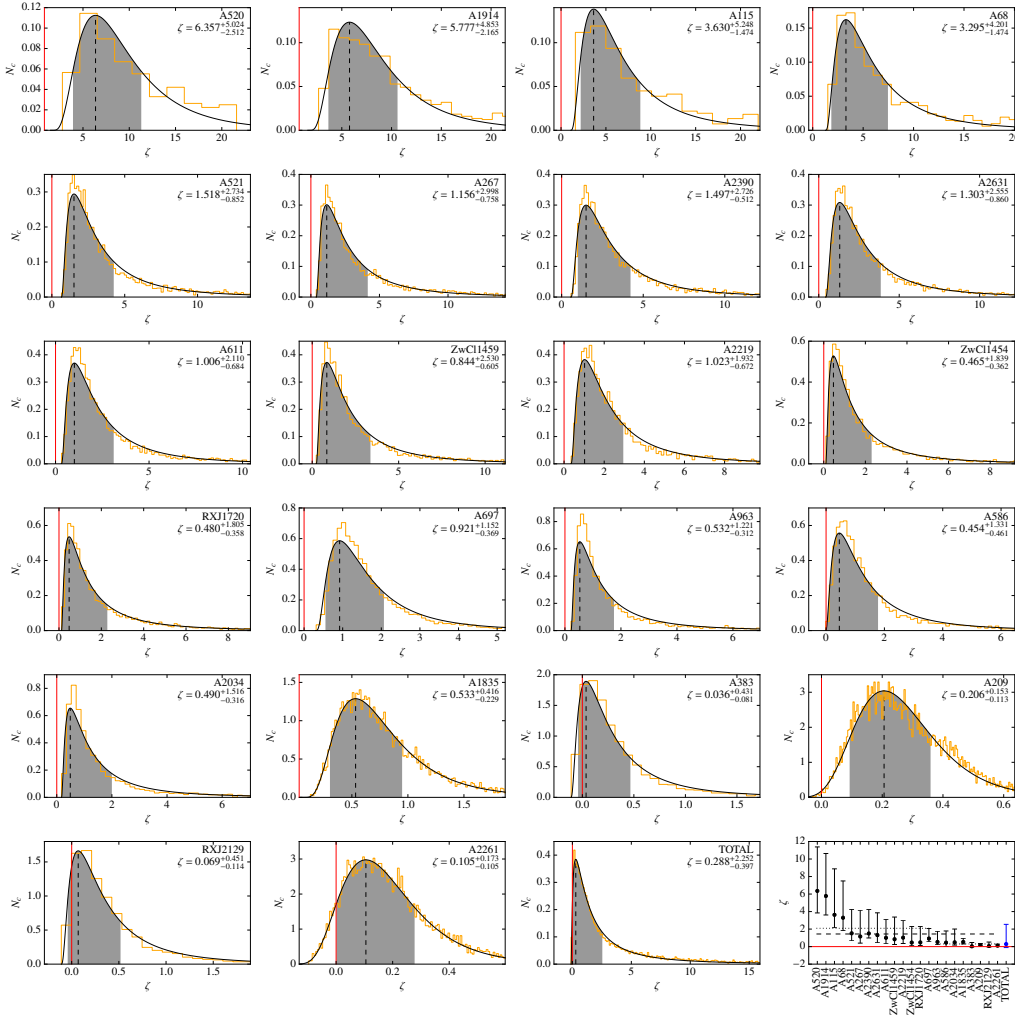[2]Salvatelli, Marchini, Lopez-Honorez & Mena have found $0.07 \leq \zeta \leq 0.30$ at 95 % CL.

Figure 6.2: Histograms for the distributions of interaction strength $\zeta$ with their log-normal fits for each cluster. The two lowest rightmost panels present the cumulated histogram of all the clusters and the most probable values and error bars for each cluster and compounded distribution in blue. The shaded areas under the histograms fits mark the 68 % CL. The vertical dashed lines point the most probable values, while the solid red line, when shown, marks the $\zeta = 0$ position. The horizontal dotted lines represent the means for each group of clusters, while the horizontal dashed line marks the overall mean.

## 6.4.3 The theoretical virial ratios

Armed with the results from the previous section, we compute with eq. (6.3) the TVR each cluster would have at perfect equilibrium in the presence of interaction. Figure 6.3 shows us their corresponding distributions. We keep conventions of
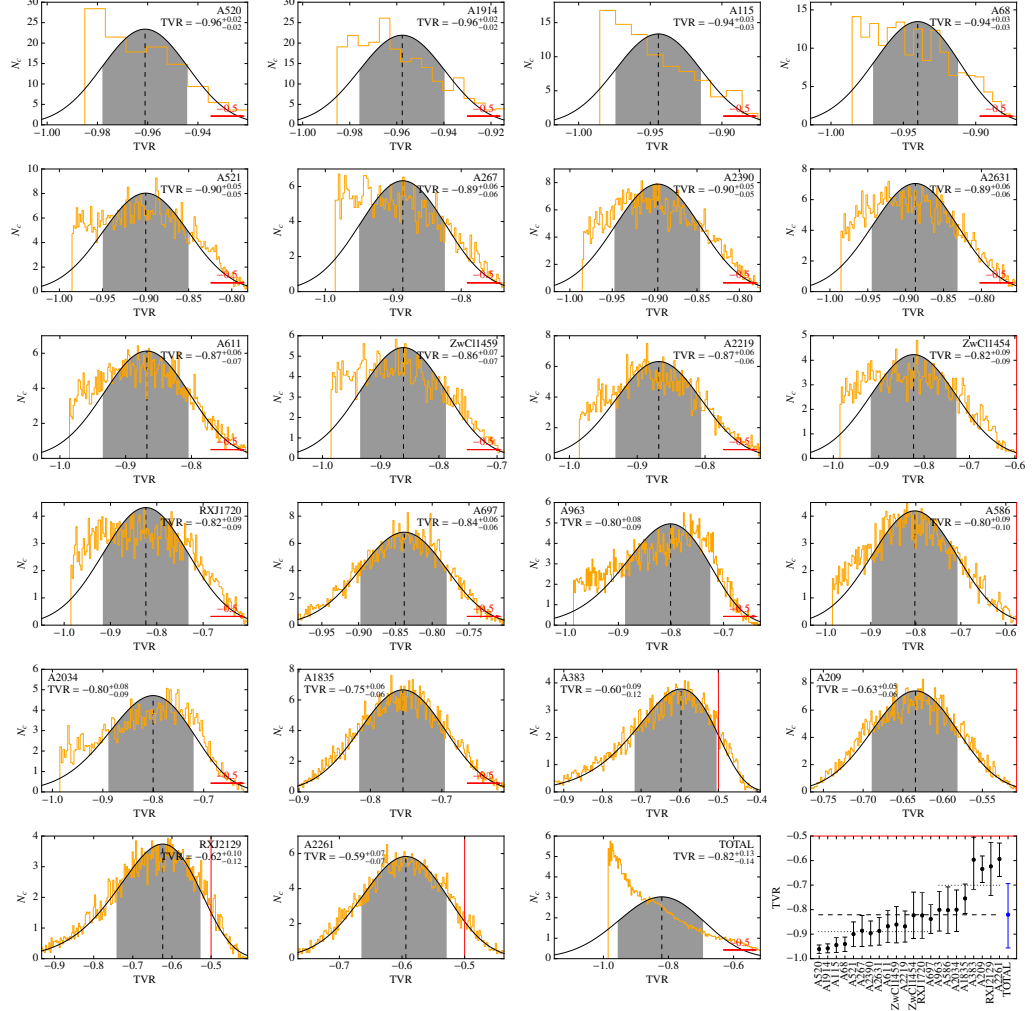
77

Figure 6.3: Histograms for the distributions of theoretical virial ratios with their log-normal fits for each cluster. The two lowest rightmost panel presents the cumulated histogram of all the clusters and the most probable TVR values with error bars. The shaded areas marks the 68 % CL. The vertical dashed lines point the most probable values, while the solid red line, when shown, marks the position of the no interaction classic virial ratio. The mean value of all most probable values is also shown, represented by the horizontal dashed black line in the last panel. The two horizontal dotted lines indicate the means of the two groups.

shaded areas and error bars representing 68 % CL, the vertical dashed lines for the most probable values and the red solid line to indicate absence of interaction, the compounded distribution represented in the last panel by the blue error bar. As these histograms are very similar to the observed ones (section 6.4.1), the following comments can be applied to both. The reasons for these similarities are discussed in section 6.4.4.

At this level, all the clusters exclude −0.5 at $1\sigma$, which confirms the result from section 6.4.1 (one cluster did not exclude that value but only marginally). However, 16 out of the 22 clusters present log-normal fits that reflects poorly the underlying distributions: A520, A1914, A115, A68, A521, A267, A2390, A2631, A611, ZwCl 1459, A2219, ZwCl 1454, RX J1720, A963, A586 and A2034. For all of those problematic distributions the log-normal fits break down for virial ratios in the proximity of −1. This is related to the singularity in eq. (6.10). In addition, the compounded TVR points towards a single value of $-0.82^{+0.13}_{-0.14}$, which represents a detection at $2\sigma$, in contradiction with the results of the previous section. All this suggests a problem with our method that assumed small deviation from equilibrium, as previously pointed out.

### 6.4.4 The departure from equilibrium factors

Eq. (6.24) with the results of section 6.4.2 allows us to compute the DfE factor for each cluster. The values of this factor relative to their TVR,

$$\frac{\text{DfE}}{\text{TVR}} = -\frac{(2 + 3\zeta)^{-2}\, \dot{\rho}_{\text{pot}}/H\rho_{\text{pot}}}{(\rho_{\text{kin}}/\rho_{\text{pot}})_{\text{th}}} = \frac{\dot{\rho}_{\text{pot}}/H\rho_{\text{pot}}}{(1 + 3\zeta)(2 + 3\zeta)}, \qquad (6.34)$$

are presented in figure 6.4. Except for A1914, A115, A68, A2390, A2219, A697 and A1835, all those relative departures are compatible with zero. We should note as well that ZwCl 1454 and A383 are the only clusters with positive DfE. For this figure and for numerical reasons, we fit the distributions for each cluster with uniform distributions so as to evaluate the order of magnitude of those departures and produce the values displayed on figure 6.4. Although not good fits, these uniform distributions enable us to show how small those values are, validating our hypothesis eq. (6.7). This explains the similarities between OVR and TVR, as seen in comparing figure 6.1b and the last panel of figure 6.3.

## 6.5 Discussion of the results

We analyzed the virial ratios of a set of clusters using a simple model based on the Layzer–Irvine equation [106–111], using weak-lensing mass profiles and intracluster gas temperatures from optical and X-ray observations [117, 118]. Our
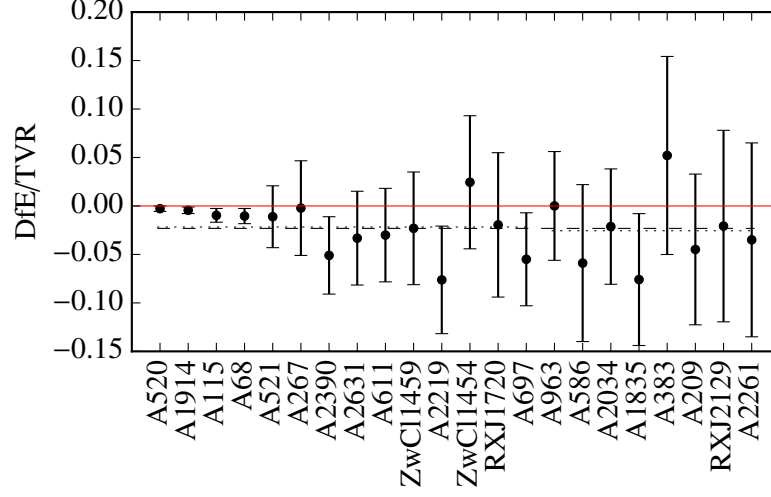
Figure 6.4: DfE factors relative to the TVR with confidence intervals for each cluster in our sample. Error bars give the 68 % CL. Dotted lines represent means for each group, while dashed line marks overall mean. The solid red line marks the absence of deviation.

treatment involved assessing the virial balance of each cluster as well as their equilibrium state, using a Monte Carlo statistical analysis on the data.

Our method, a first proof of concept for out of equilibrium virial evaluation, enabled us to find mild evidence for an interacting dark sector in the virial balance of those clusters, however yielding only small amplitudes of departure from equilibrium: although the compounded distribution of all clusters would accommodate $\zeta = 0$, a majority of the individual clusters, of their virial ratios and of the compounded evaluation of the virial ratio all point towards a positive interaction. The compounded estimates give us $\zeta = 0.29^{+2.25}_{-0.40}$, which is not a detection, but $(\rho_{kin}/\rho_{pot})_{th} = -0.82^{+0.13}_{-0.14}$, which is a detection at $2\sigma$. This tension between the compounded results for the interaction strength and the TVR, while the latter is constructed out of the former, points to the main problem in our results: despite the scatter in the values of virial ratios, the DfE factors remain small, as imposed in our hypotheses. In addition, our method contains an unphysical singularity at $\rho_{kin}/\rho_{pot} = -1$ in eq. (6.10). These problems, in spite of encouraging results, call for follow-up work which should remove the small departure from equilibrium hypothesis, as well as the singularity we introduced in this work for $\rho_{kin} = -\rho_{pot}$.

# Chapter 7

# Final considerations

We have studied dark energy interacting models and tested them against different types of large-scale structure observations. These works culminated in the production of two papers [6, 7], one of them already published, besides the development of a code for MCMC parameter estimation and another one for obtaining equations of motion and other quantities in GR from a given metric. Both codes are entirely written in python, with potential for a wide variety of uses, and will be made publicly available in the near future. In the first work here presented, we have derived the analytical expression for the growth rate of structures in terms of the growth index $\gamma$ in the presence of a DE-DM interaction. The derivation was based on the expansion of the growth index and the DE equation of state in power series of the dark energy density parameter $\Omega_{\mathrm{DE}}(z)$, which parametrizes the time evolution. We have proved the method to be successful in yielding an expression for $\gamma$ in terms of the EoS coefficients $w_0, w_1, \ldots$ and the coupling constant $\zeta$ when the interaction term in the energy conservation equation is written as $Q_0^{\mathrm{DM}} \propto \mathcal{H}\zeta\rho_{\mathrm{DE}}$, i.e., proportional do the DE density. The growth rate is then written as

$$f(\Omega_{\mathrm{DM}}) \approx [\Omega_{\mathrm{DM}}]^{\gamma_0 + \gamma_1 \Omega_{\mathrm{DE}}}$$

with the growth index coefficients given by

$$\gamma_0 = \frac{3\,(1 - w_0 + 5\zeta)}{5 - 6w_0 - 6\zeta},$$

$$\gamma_1 = \frac{-\gamma_0^2 + \gamma_0\,(1 + 12w_1 + 18\zeta) - 6w_1 + 6\zeta\,(5 - 6w_0 + 6\zeta)}{2\,(5 - 12w_0 - 12\zeta)},$$

up to first order in the DE density parameter. Since we consider only the two components, the DM density parameter is $\Omega_{\text{DM}} = 1 - \Omega_{\text{DE}}$ and

$$\Omega_{\text{DE}}(z) \approx \frac{\Omega_{\text{DE},0} \, (1+z)^{3(w_0+\zeta)} \left[ 1 - \Omega_{\text{DE},0} + \Omega_{\text{DE},0} \, (1+z)^{3(w_0+\zeta)} \right]^{\frac{w_1+\zeta}{w_0+\zeta}}}{1 - \Omega_{\text{DE},0} + \Omega_{\text{DE},0} \, (1+z)^{3(w_0+\zeta)} \left[ 1 - \Omega_{\text{DE},0} + \Omega_{\text{DE},0} \, (1+z)^{3(w_0+\zeta)} \right]^{\frac{w_1+\zeta}{w_0+\zeta}}},$$

This is one of the main results of this thesis. We showed that the growth rate should be altered by a term proportional to the interaction coupling to make the continuity equation compatible with the non-interacting model assumed for the measurements, namely $\tilde{f} \equiv f + 3\zeta \frac{1 - \Omega_{\text{DE}}}{\Omega_{\text{DE}}}$. The analytical expressions obtained then enabled us to compare the modified growth $\tilde{f}\sigma_8$ predicted by the interacting DE model with $f\sigma_8$ measurements from redshift-space distortions, with $\sigma_8$ given by

$$\sigma_8(z) \approx \sigma_{8,0} \left[ \frac{\Omega_{\text{DE}}(z)}{\Omega_{\text{DE},0}} \right]^{-\frac{1}{3(w_0+\zeta)}} \exp \left\{ \frac{\varepsilon_1 \left[ \Omega_{\text{DE}}(z) - \Omega_{\text{DE},0} \right] + \varepsilon_2 \left[ \Omega_{\text{DE}}^2(z) - \Omega_{\text{DE},0}^2 \right]}{3 \, (w_0 + \zeta)} \right\},$$

with

$$\varepsilon_1 \equiv \gamma_0 - \frac{w_0 - w_1}{w_0 + \zeta},$$

$$\varepsilon_2 \equiv -\frac{\gamma_0^2}{4} + \frac{\gamma_0}{2} \left( \frac{1}{2} + \frac{w_0 - w_1}{w_0 + \zeta} \right) + \frac{\gamma_1}{2} - \frac{w_0^2 + w_1^2 - w_1 \, (w_0 - \zeta) - w_2 \, (w_0 + \zeta)}{2 \, (w_0 + \zeta)^2}.$$

However, it was not possible to obtain tight constraints on the interaction strength due to the small number of measurements and their large uncertainties. The constraining power of these RSD measurements is remarkable when combined with CMB and other data, drastically reducing the region of the parameter space favored by observations.

When considering the analytical evaluation of the growth rate, Hubble rate measurements and supernovae data are particularly interesting for combining with RSD, since their predictions are made at the background level and can also be expressed analytically in terms of the model parameters. Their integration with the code developed for this work may be straightforward and is being considered for a follow-up work. We also plan to analyze the possibility of inclusion of the decaying mode of the matter perturbations, which could contribute more significantly in some cases, depending on the interaction.

When the interaction is proportional do the DM density, we find that the zeroth order terms of the expansion around $\Omega_{\text{DE}} = 0$ require $\zeta$ to be zero, thus forbidding the interacting cosmology. This is another important result, since the approximation $f \approx \Omega_{\text{M}}^\gamma$ is known to describe very well the growth rate in a wide variety of DE models and is widely adopted.

We have thus shown that the growth index parametrization cannot account for this specific type of interacting model. Still, we have studied this interaction $Q_0^{\mathrm{DM}} \propto \mathcal{H}\zeta\rho_{\mathrm{DM}}$ but in a different scenario and with other type of observations. Galaxy clusters have been considered as dynamical systems whose equilibrium state—altered by the coupling between dark sectors as dictated by the Layzer–Irvine equation—may reveal the existence of interaction. We find a hint of a positive interaction, although still compatible with zero at $1\sigma$ CL:

$$\zeta = 0.29^{+2.25}_{-0.40}, \qquad (1\sigma \ \mathrm{CL})$$

but also a $2\sigma$ detection in the compounded theoretical virial ratio

$$\left(\frac{\rho_{\mathrm{kin}}}{\rho_{\mathrm{pot}}}\right)_{\mathrm{th}} = -0.82^{+0.13}_{-0.14}. \qquad (1\sigma \ \mathrm{CL})$$

Most observed clusters appear to be somewhat perturbed systems and are maybe still forming (accreting mass), which is expected in the current standard cosmological scenario. Our approach treating clusters as out of equilibrium systems is therefore natural, despite the measurement of such departure not following the observed wide variations in virial states. The tension between the results of our measured departure from the classic virial ratio and our measured interaction strength indicates that our method shows potential but also has room for improvement. We expect that accommodation for large departures will enable the use of much larger samples, statistically enhancing the significance of these results.

# Bibliography

[1] A. G. Riess et al. "Observational Evidence from Supernovae for an Accelerating Universe and a Cosmological Constant". *The Astronomical Journal* 116.3 (Sept. 1998), pp. 1009–1038.

[2] S. Perlmutter et al. "Measurements of $\Omega$ and $\Lambda$ from 42 High-Redshift Supernovae". *The Astrophysical Journal* 517.2 (1999), p. 565.

[3] A. Friedmann. "On the Curvature of Space". *General Relativity and Gravitation* 31.12 (1999), pp. 1991–2000.

[4] F. Zwicky. "Republication of: The redshift of extragalactic nebulae". *General Relativity and Gravitation* 41.1 (2009), pp. 207–224.

[5] F. Zwicky. "On the Masses of Nebulae and of Clusters of Nebulae". *The Astrophysical Journal* 86 (Oct. 1937), p. 217.

[6] R. J. F. Marcondes et al. "Analytic study on the effect of dark energy–dark matter interaction on the growth of structures". arXiv: `1605.05264` `[astro-ph.CO]`.

[7] M. Le Delliou, R. J. F. Marcondes, G. B. Lima Neto & E. Abdalla. "Non-virialized clusters for detection of dark energy–dark matter interaction". *Monthly Notices of the Royal Astronomical Society* 453.1 (2015), pp. 2–13.

[8] E. Hubble. "A relation between distance and radial velocity among extra-galactic nebulae". *Proceedings of the National Academy of Sciences* 15.3 (1929), pp. 168–173.

[9] Planck Collaboration. "Planck 2015 results. XIII. Cosmological parameters". arXiv: `1502.01589` `[astro-ph.CO]`.

[10] A. G. Riess et al. "A 2.4 % Determination of the Local Value of the Hubble Constant". *The Astrophysical Journal* 826.1 (2016), p. 56.

[11] J. L. Bernal, L. Verde & A. G. Riess. "The trouble with $H_0$". arXiv: `1607.05617` `[astro-ph.CO]`.

[12]  A. G. Lemaître. "A Homogeneous Universe of Constant Mass and Increasing Radius accounting for the Radial Velocity of Extra-galactic Nebulæ". *Monthly Notices of the Royal Astronomical Society* 91.5 (1931), pp. 483–490.

[13]  H. P. Robertson. "Kinematics and World-Structure". *The Astrophysical Journal* 82 (Nov. 1935), p. 284.

[14]  A. G. Walker. "On Milne's Theory of World-Structure". *Proceedings of the London Mathematical Society* s2-42.1 (1937), pp. 90–127.

[15]  K. A. Olive et al. "Review of Particle Physics". *Chinese Physics C* 38.9 (2014), p. 090001.

[16]  C. Wetterich. "Cosmology and the fate of dilatation symmetry". *Nuclear Physics B* 302.4 (1988), pp. 668–696.

[17]  P. J. E. Peebles & B. Ratra. "Cosmology with a time-variable cosmological 'constant'". *The Astrophysical Journal Letters* 325 (Feb. 1988), pp. L17–L20.

[18]  R. R. Caldwell, R. Dave & P. J. Steinhardt. "Quintessential Cosmology – Novel Models of Cosmological Structure Formation". *Astrophysics and Space Science* 261.1 (1998), pp. 303–310.

[19]  C. L. Bennett et al. "Nine-year Wilkinson Microwave Anisotropy Probe (WMAP) Observations: Final Maps and Results". *The Astrophysical Journal Supplement Series* 208.2 (2013), p. 20.

[20]  G. Hinshaw et al. "Nine-year Wilkinson Microwave Anisotropy Probe (WMAP) Observations: Cosmological Parameter Results". *The Astrophysical Journal Supplement Series* 208.2 (2013), p. 19.

[21]  S. Dodelson. *Modern Cosmology*. Academic Press, 2003.

[22]  W. Hillebrandt & J. C. Niemeyer. "TYPE IA SUPERNOVA EXPLOSION MODELS". *Annual Review of Astronomy and Astrophysics* 38.1 (2000), pp. 191–230.

[23]  P. Schneider. *Extragalactic Astronomy and Cosmology: An Introduction.* Springer, 2006.

[24]  A. Coc, J.-P. Uzan & E. Vangioni. "Standard big bang nucleosynthesis and primordial CNO abundances after Planck". *Journal of Cosmology and Astroparticle Physics* 10 (2014), p. 050.

[25]  A. A. Penzias & R. W. Wilson. "A Measurement of excess antenna temperature at 4080 Mc/s". *The Astrophysical Journal* 142 (1965), pp. 419–421.

[26] R. H. Dicke, P. J. E. Peebles, P. G. Roll & D. T. Wilkinson. "Cosmic Black-Body Radiation". *The Astrophysical Journal* 142 (1965), pp. 414–419.

[27] S. Weinberg. *Cosmology*. Oxford University Press, 2008.

[28] J. C. Mather et al. "Measurement of the Cosmic Microwave Background spectrum by the COBE FIRAS instrument". *The Astrophysical Journal* 420 (1994), pp. 439–444.

[29] D. J. Fixsen et al. "The Cosmic Microwave Background Spectrum from the Full COBE FIRAS Data Set". *The Astrophysical Journal* 473.2 (1996), p. 576.

[30] D. J. Fixsen. "The Temperature of the Cosmic Microwave Background". *The Astrophysical Journal* 707.2 (2009), p. 916.

[31] D. J. Eisenstein et al. "Detection of the Baryon Acoustic Peak in the Large-Scale Correlation Function of SDSS Luminous Red Galaxies". *The Astrophysical Journal* 633.2 (2005), p. 560.

[32] L. Miao, L. Xiao-Dong, W. Shuang & W. Yi. "Dark Energy". *Communications in Theoretical Physics* 56.3 (2011), p. 525.

[33] Y.-S. Song & W. J. Percival. "Reconstructing the history of structure formation using redshift distortions". *Journal of Cosmology and Astroparticle Physics* 10 (2009), p. 004.

[34] A. Guth. "Inflationary universe: A possible solution to the horizon and flatness problems". *Physical Review D* 23.2 (Jan. 1981), pp. 347–356.

[35] S. Hawking, I. Moss & J. Stewart. "Bubble collisions in the very early universe". *Physical Review D* 26.10 (Nov. 1982), pp. 2681–2693.

[36] A. H. Guth & E. J. Weinberg. "Could the universe have recovered from a slow first-order phase transition?" *Nuclear Physics B* 212.2 (1983), pp. 321–364.

[37] A. D. Linde. "A new inflationary universe scenario: A possible solution of the horizon, flatness, homogeneity, isotropy and primordial monopole problems". *Physics Letters B* 108.6 (1982), pp. 389–393.

[38] A. Albrecht & P. Steinhardt. "Cosmology for Grand Unified Theories with Radiatively Induced Symmetry Breaking". *Physical Review Letters* 48.17 (Apr. 1982), pp. 1220–1223.

[39] D. Baumann. "TASI Lectures on Inflation". arXiv: `0907.5424` [`hep-th`].

[40] A. Einstein. "Kosmologische Betrachtungen zur allgemeinen Relativitätstheorie". German.

[41] S. Weinberg. "The cosmological constant problem". *Reviews of Modern Physics* 61.1 (Jan. 1989), pp. 1–23.

[42] L. Amendola & S. Tsujikawa. *Dark Energy: Theory and Observations*. Cambridge University Press, 2010.

[43] G. Montani, M. V. Battisti, R. Benini & G. Imponente. *Primordial Cosmology*. World Scientific Publishing Company, 2011.

[44] T. Padmanabhan. "Cosmological constant—the weight of the vacuum". *Physics Reports* 380.5-6 (2003), pp. 235–320.

[45] V. L. Fitch, D. R. Marlow, M. A. E. Dementi & F. J. Dyson. "Critical Problems in Physics". *American Journal of Physics* 66.9 (1998), pp. 837–838.

[46] I. Zlatev, L. Wang & P. Steinhardt. "Quintessence, Cosmic Coincidence, and the Cosmological Constant". *Physical Review Letters* 82.5 (Feb. 1999), pp. 896–899.

[47] S. del Campo, R. Herrera, G. Olivares & D. Pavón. "Interacting models of soft coincidence". *Physical Review D* 74.2 (July 2006), p. 023501.

[48] J.-H. He, B. Wang & E. Abdalla. "Testing the interaction between dark energy and dark matter via the latest observations". *Physical Review D* 83.6 (Mar. 2011), p. 063515.

[49] V. Poitras. "Can the coincidence problem be solved by a cosmological model of coupled dark energy and dark matter?" *General Relativity and Gravitation* 46.6 (2014), p. 1732.

[50] P. Ferreira, D. Pavón & J. Carvalho. "On detecting interactions in the dark sector with $H(z)$ data". *Physical Review D* 88.8 (Oct. 2013), p. 083503.

[51] D. G. A. Duniya, D. Bertacca & R. Maartens. "Clustering of quintessence on horizon scales and its imprint on HI intensity mapping". *Journal of Cosmology and Astroparticle Physics* 10 (2013), p. 015.

[52] P. J. E. Peebles. *Principles of physical cosmology*. Princeton University Press, 1993.

[53] P. J. E. Peebles. *The Large-Scale Structure of the Universe*. Princeton University Press, 1980.

[54] B. Leistedt, H. V. Peiris & N. Roth. "Constraints on Primordial Non-Gaussianity from 800 000 Photometric Quasars". *Physical Review Letters* 113.22 (Nov. 2014), p. 221301.

[55] Planck Collaboration. "Planck 2013 results. XXIV. Constraints on primordial non-Gaussianity". *Astronomy & Astrophysics* 571 (2014), A24.

[56]  N. Kaiser. "On the spatial correlations of Abell clusters". *The Astrophysical Journal Letters* 284 (Sept. 1984), pp. L9–L12.

[57]  A. Dressler. "Galaxy morphology in rich clusters: Implications for the formation and evolution of galaxies". *The Astrophysical Journal* 236 (Mar. 1980), pp. 351–365.

[58]  M. Postman & M. J. Geller. "The morphology-density relation: The group connection". *The Astrophysical Journal* 281 (June 1984), pp. 95–99.

[59]  L. Verde et al. "First-Year Wilkinson Microwave Anisotropy Probe (WMAP) Observations: Parameter Estimation Methodology". *The Astrophysical Journal Supplement Series* 148.1 (2003), p. 195.

[60]  H. Hoekstra et al. "Weak Lensing Study of Galaxy Biasing". *The Astrophysical Journal* 577.2 (2002), p. 604.

[61]  L. Verde et al. "The 2dF Galaxy Redshift Survey: the bias of galaxies and the density of the Universe". 335.2 (2002), pp. 432–440.

[62]  J. A. Peacock et al. "A measurement of the cosmological mass density from clustering in the 2dF Galaxy Redshift Survey". *Nature* (2001), pp. 169–173.

[63]  M. Colless et al. "The 2dF Galaxy Redshift Survey: spectra and redshifts". *Monthly Notices of the Royal Astronomical Society* 328 (2001), pp. 1039–1063.

[64]  A. J. S. Hamilton. "Linear Redshift Distortions: A Review". Astrophysics and Space Science Library 231 (1998), pp. 185–275.

[65]  N. Kaiser. "Clustering in real space and in redshift space". *Monthly Notices of the Royal Astronomical Society* 227 (July 1987), pp. 1–21.

[66]  A. Ratcliffe, T. Shanks, Q. A. Parker & R. Fong. "The Durham/UKST Galaxy Redshift Survey – IV. Redshift-space distortions in the two-point correlation function". *Monthly Notices of the Royal Astronomical Society* 296.1 (May 1998), pp. 191–205.

[67]  A. P. Lightman & P. L. Schechter. "The Omega dependence of peculiar velocities induced by spherical density perturbations". *The Astrophysical Journal Supplement Series* 74 (Dec. 1990), p. 831.

[68]  L. Wang & P. J. Steinhardt. "Cluster Abundance Constraints for Cosmological Models with a Time-varying, Spatially Inhomogeneous Energy Component with Negative Pressure". *The Astrophysical Journal* 508 (1998), p. 483.

[69]  Y. Gong, M. Ishak & A. Wang. "Growth factor parametrization in curved space". *Physical Review D* 80.2 (2009), p. 023002.

[70] E. V. Linder & R. N. Cahn. "Parameterized beyond-Einstein growth". *Astroparticle Physics* 28 (2007), p. 481.

[71] Y. Gong. "Growth factor parametrization and modified gravity". *Physical Review D* 78.12 (2008), p. 123010.

[72] E. V. Linder. "Cosmic growth history and expansion history". *Physical Review D* 72 (2005), p. 043529.

[73] R. Gannouji & D. Polarski. "The growth of matter perturbations in some scalar–tensor DE models". *Journal of Cosmology and Astroparticle Physics* 05 (2008), p. 018.

[74] J. Dossett et al. "Constraints on growth index parameters from current and future observations". *Journal of Cosmology and Astroparticle Physics* 04 (2010), p. 022.

[75] F. Simpson, B. Jackson & J. A. Peacock. "Unmodified gravity". *Monthly Notices of the Royal Astronomical Society* 411 (2011), pp. 1053–1058.

[76] S. Tsujikawa, A. D. Felice & J. Alcaniz. "Testing for dynamical dark energy models with redshift-space distortions". *Journal of Cosmology and Astroparticle Physics* 01 (2013), p. 030.

[77] J. Väliviita, E. Majerotto & R. Maartens. "Large-scale instability in interacting dark energy and dark matter fluids". *Journal of Cosmology and Astroparticle Physics* 07 (2008), p. 020.

[78] J.-H. He, B. Wang & E. Abdalla. "Stability of the curvature perturbation in dark sectors' mutual interacting models". *Physics Letters B* 671.1 (2009), pp. 139–145.

[79] M. Gavela et al. "Dark coupling". *Journal of Cosmology and Astroparticle Physics* 07 (2009), p. 034.

[80] A. Lewis, A. Challinor & A. Lasenby. "Efficient Computation of Cosmic Microwave Background Anisotropies in Closed Friedmann-Robertson-Walker Models". *The Astrophysical Journal* 538.2 (2000), p. 473.

[81] S. Basilakos, S. Nesseris & L. Perivolaropoulos. "Observational constraints on viable $f(R)$ parametrizations with geometrical and dynamical probes". *Physical Review D* 87 (2013), p. 123529.

[82] M. J. Hudson & S. J. Turnbull. "The Growth Rate of Cosmic Structure from Peculiar Velocities at Low and High Redshifts". *The Astrophysical Journal Letters* 751 (2012), p. L30.

[83] R. Tojeiro et al. "The clustering of galaxies in the SDSS-III Baryon Oscillation Spectroscopic Survey: measuring structure growth using passive galaxies". *Monthly Notices of the Royal Astronomical Society* 424 (2012), p. 2339.

[84] F. Beutler et al. "The 6dF Galaxy Survey: $z \approx 0$ measurements of the growth rate and $\sigma_8$". *Monthly Notices of the Royal Astronomical Society* 423 (2012), p. 3430.

[85] C. Blake et al. "The WiggleZ Dark Energy Survey: the growth rate of cosmic structure since redshift $z = 0.9$". *Monthly Notices of the Royal Astronomical Society* 415 (2011), p. 2876.

[86] M. Feix, A. Nusser & E. Branchini. "Growth Rate of Cosmological Perturbations at $z \sim 0.1$ from a New Observational Test". *Physical Review Letters* 115.1 (2015), p. 011301.

[87] W. J. Percival et al. "The 2dF Galaxy Redshift Survey: spherical harmonics analysis of fluctuations in the final catalogue". *Monthly Notices of the Royal Astronomical Society* 353 (2004), p. 1201.

[88] B. A. Reid et al. "The clustering of galaxies in the SDSS-III Baryon Oscillation Spectroscopic Survey: measurements of the growth of structure and expansion rate at $z = 0.57$ from anisotropic clustering". *Monthly Notices of the Royal Astronomical Society* 426 (2012), p. 2719.

[89] L. Samushia, W. Percival & A. Raccanelli. "Interpreting large-scale redshift-space distortion measurements". *Monthly Notices of the Royal Astronomical Society* 420 (2012), p. 2102.

[90] L. Guzzo et al. "A test of the nature of cosmic acceleration using galaxy redshift distortions". *Nature* 451 (2008), p. 541.

[91] M. Tegmark et al. "Cosmological constraints from the SDSS luminous red galaxies". *Physical Review D* 74 (2006), p. 123507.

[92] S. de la Torre et al. "The VIMOS Public Extragalactic Redshift Survey (VIPERS) – Galaxy clustering and redshift-space distortions at $z = 0.8$ in the first data release". *Astronomy & Astrophysics* 557 (2013), A54.

[93] S. J. Turnbull et al. "Cosmic flows in the nearby universe from Type Ia supernovae". *Monthly Notices of the Royal Astronomical Society* 420 (2012), p. 447.

[94] M. Davis et al. "Local gravity versus local velocity: solutions for $\beta$ and non-linear bias". *Monthly Notices of the Royal Astronomical Society* 413 (2011), p. 2906.

[95] M. Oh & Y.-S. Song. "Measuring neutrino mass imprinted on the anisotropic galaxy clustering". arXiv: `1607.01074 [astro-ph.CO]`.

[96] A. Taruya, T. Nishimichi & S. Saito. "Baryon acoustic oscillations in 2D: Modeling redshift-space power spectrum from perturbation theory". *Physical Review D* 82 (2010), p. 063522.

[97] C. Geyer. "Introduction to Markov Chain Monte Carlo". In: *Chapman & Hall/CRC Handbooks of Modern Statistical Methods*. Informa UK Limited, 2011. doi: `10.1201/b10905-2`.

[98] D. Foreman-Mackey, D. Hogg, D. Lang & J. Goodman. "`emcee`: The MCMC Hammer".

[99] A. Heavens. "Statistical techniques in cosmology". arXiv: `0906.0664 [astro-ph.CO]`.

[100] S. P. Brooks & A. Gelman. "General Methods for Monitoring Convergence of Iterative Simulations". *Journal of Computational and Graphical Statistics* 7 (1998), p. 434.

[101] A. Gelman & D. B. Rubin. "Inference from Iterative Simulation Using Multiple Sequences". *Statistical Science* 7 (1992), p. 457.

[102] K. V. Mardia, J. T. Kent & J. M. Bibby. *Multivariate Analysis*. Academic Press, 1980.

[103] W. Yang & L. Xu. "Cosmological constraints on interacting dark energy with redshift-space distortion after Planck data". *Physical Review D* 89.8 (Apr. 2014), p. 083517.

[104] R. Murgia, S. Gariazzo & N. Fornengo. "Constraints on the coupling between dark energy and dark matter from CMB data". *Journal of Cosmology and Astroparticle Physics* 04 (2016), p. 014.

[105] A. A. Costa, X.-D. Xu, B. Wang & E. Abdalla. "Constraints on interacting dark energy models from Planck 2015 and redshift-space distortion data". arXiv: `1605.04138 [astro-ph.CO]`.

[106] O. Bertolami, F. Gil Pedro & M. Le Delliou. "Dark energy–dark matter interaction and putative violation of the equivalence principle from the Abell cluster A586". *Physics Letters B* 654.5-6 (2007), pp. 165–169.

[107] O. Bertolami, F. Gil Pedro & M. Le Delliou. "The Abell cluster A586 and the detection of violation of the equivalence principle". *General Relativity and Gravitation* 41.12 (2009), pp. 2839–2846.

[108] O. Bertolami, F. Gil Pedro & M. Le Delliou. "Testing the interaction of dark energy to dark matter through the analysis of virial relaxation of clusters Abell clusters A586 and A1689 using realistic density profiles". *General Relativity and Gravitation* 44.4 (2012), pp. 1073–1088.

[109] E. Abdalla, L. R. Abramo, L. S. Jr. & B. Wang. "Signature of the interaction between dark energy and dark matter in galaxy clusters". *Physics Letters B* 673.2 (2009), pp. 107–110.

[110] E. Abdalla, L. R. Abramo & J. C. C. de Souza. "Signature of the interaction between dark energy and dark matter in observations". *Physical Review D* 82.2 (July 2010), p. 023508.

[111] J.-H. He, B. Wang, E. Abdalla & D. Pavón. "The imprint of the interaction between dark sectors in galaxy clusters". *Journal of Cosmology and Astroparticle Physics* 12 (2010), p. 022.

[112] P. P. Avelino & C. F. V. Gomes. "Generalized Layzer-Irvine equation: The role of dark energy perturbations in cosmic structure formation". *Physical Review D* 88 (Aug. 2013), p. 043514.

[113] J. F. Navarro, C. S. Frenk & S. D. M. White. "The Structure of Cold Dark Matter Halos". *The Astrophysical Journal* 462 (May 1996), p. 563.

[114] A. Vikhlinin et al. "*Chandra* Temperature Profiles for a Sample of Nearby Relaxed Galaxy Clusters". *The Astrophysical Journal* 628.2 (2005), p. 655.

[115] G. W. Pratt et al. "Temperature profiles of a representative sample of nearby X-ray galaxy clusters". *Astronomy & Astrophysics* 461.1 (2007), pp. 71–80.

[116] A. Moretti, F. Gastaldello, S. Ettori & S. Molendi. "Gas temperature profiles in galaxy clusters with Swift XRT: observations and capabilities to map near $R_{200}$". *Astronomy & Astrophysics* 528 (2011), A102.

[117] N. Okabe et al. "LoCuSS: Subaru Weak Lensing Study of 30 Galaxy Clusters". *Publications of the Astronomical Society of Japan* 62.3 (2010), pp. 811–870.

[118] Planck Collaboration. "Planck intermediate results – III. The relation between galaxy cluster mass and Sunyaev-Zeldovich signal". *Astronomy & Astrophysics* 550 (Feb. 2013), A129.

[119] D. Landry et al. "Chandra measurements of a complete sample of X-ray luminous galaxy clusters: the gas mass fraction". *Monthly Notices of the Royal Astronomical Society* 433.4 (2013), pp. 2790–2811.

[120]   K. W. Cavagnolo, M. Donahue, G. M. Voit & M. Sun. "Bandpass Dependence of X-Ray Temperatures in Galaxy Clusters". *The Astrophysical Journal* 682.2 (2008), p. 821.

[121]   SymPy Development Team. *SymPy: Python library for symbolic mathematics*. 2014. url: `http://www.sympy.org`.

[122]   M. Markevitch, F. Govoni, G. Brunetti & D. Jerius. "Bow Shock and Radio Halo in the Merging Cluster A520". *The Astrophysical Journal* 627.2 (2005), p. 733.

[123]   R. Barrena, M. Girardi & W. Boschin. "The puzzling merging cluster Abell 1914: new insights from the kinematics of member galaxies". *Monthly Notices of the Royal Astronomical Society* 430.4 (2013), pp. 3453–3464.

[124]   F. Andrade-Santos, G. B. L. Neto & T. F. Laganá. "A New Method to Quantify X-Ray Substructures in Clusters of Galaxies". *The Astrophysical Journal* 746.2 (2012), p. 139.

[125]   R. E. G. Machado & G. B. Lima Neto. "Simulations of the merging galaxy cluster Abell 3376". *Monthly Notices of the Royal Astronomical Society* 430.4 (2013), pp. 3249–3260.

[126]   Y.-J. Xue & X.-P. Wu. "The $L_X$-$T$, $L_X$-$\sigma$, and $\sigma$-$T$ Relations for Groups and Clusters of Galaxies". *The Astrophysical Journal* 538.1 (2000), p. 65.

[127]   V. Salvatelli, A. Marchini, L. Lopez-Honorez & O. Mena. "New constraints on coupled dark energy from the Planck satellite experiment". *Physical Review D* 88.2 (July 2013), p. 023531.